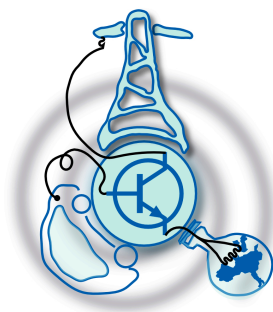# Control of Axial Active Magnetic Bearings for Flywheel-based Energy Storage System

by

Juan Morís Gómez

Submitted to the Department of Electrical Engineering, Electronics, Computers and Systems
in partial fulfillment of the requirements for the degree of

Master of Science in Electrical Energy Conversion and Power Systems

at the

UNIVERSIDAD DE OVIEDO

July 2014

Author . . . .

Certified by . . . .
Pablo García Fernández
Associate Professor
Thesis Supervisor

Control of Axial Active Magnetic Bearings for Flywheel-based Energy Storage System

by

Juan Morís Gómez

Submitted to the Department of Electrical Engineering, Electronics, Computers and Systems
on July 22, 2014, in partial fulfillment of the
requirements for the degree of
Master of Science in Electrical Energy Conversion and Power Systems

Abstract

This thesis deals with the design and implementation of the control system for a Flywheel-based Energy Storage System (FESS) with active magnetic bearings. The thesis focuses on the construction of realistic model of the system according to experimental tests. The simulation model will be used to control the thrust magnetic bearings in order to withstand the flywheel in levitation.

Finally, the project also deals with the practical issues associated to the digital implementation of such control system in Digital Signal Processor (DSP) as well as the description of the hardware developed for the future control of the radial magnetic bearings of the prototype.

Thesis Supervisor: Pablo García Fernández
Title: Associate Professor

Acknowledgments

I would like to thank all the people who have been supporting me throughout these two years of Master, specially my supervisor Pablo García and my colleagues from the Electric Drives and Power Converters research group, where the project has been developed.

Contents

List of Figures

List of Tables

Nomenclature

Position Control Variables

z^*	Flywheel position command with respect to levitation set point	$[\mu m]$
z	Flywheel position with respect to levitation set point	$[\mu m]$
g	Air gap between flywheel and top thrust magnetic bearing	$[\mu m]$
e_p	Position error	$[\mu m]$
v^*	Flywheel vertical velocity command	$[mm/s]$
v_s	Flywheel vertical velocity	$[mm/s]$
v_k	Flywheel vertical velocity feedback	$[mm/s]$
F_{cont}	Force command from velocity controller	$[N]$
F_i	Permanent magnet ring force	$[N]$
F_{ref}	Force command with decoupled weight effect	$[N]$
F_{in}	Force command for magnetic bearing	$[N]$
B_{in}	Magnetic field intensity command for magnetic bearing	$[T]$
F_{out}	Simulated magnetic force of the bearing	$[N]$
B_{out}	Simulated magnetic field intensity of the bearing	$[T]$
F_s	Total applied force to mechanical system	$[N]$
a_s	Simulated vertical acceleration of the flywheel	$[m/s^2]$
m	Flywheel body mass	$[kg]$
g_a	Gravitational acceleration	$[m/s^2]$

Current Control Variables

i^*	Current command for axial magnetic bearing coil	$[A]$
i	Actual current through axial magnetic bearing coil	$[A]$
e_i	Current error	$[A]$
u	Voltage across axial magnetic bearing coil	$[V]$

Transfer Functions

$G0$	Magnetic bearing coil	$[A/V]$
$C0$	Current controller	$[V/A]$
$G2$	Flywheel velocity response	$[(mm/s)/N]$
$C2$	Velocity controller	$[N/(mm/s)]$
$G3$	Flywheel position response	$[\mu m/(mm/s)]$
$C3$	Position controller	$[(mm/s)/\mu m]$

Chapter 1

Introduction

1.1   Background

This project is contextualized within a research line dealing with a flywheel-based energy storage system prototype developed within the Electrical Engineering Department at the Polytechnical School of Engineering of Gijón (University of Oviedo).

This project comes as a continuation of the final degree's project, which was aimed to develop the power converter and the basic implementation of the control system for the axial magnetic bearings [12].

1.2   Research objectives and opportunities

Taking the work done as an starting point, this master thesis is aimed to correctly identify the axial levitation system based on laboratory experiments and tests with the flywheel prototype, as well as to carry out the control of the vertical magnetic levitation of the flywheel through simulation and preliminary experimental validation.

Additionally, the hardware development for the radial magnetic bearings will be also provided for future use, in order to help the implementation of previously conducted works on the radial magnetic bearings control [19].

1.3   Document Structure

Nomenclature gathers a list of the control variables involved in the control system, including a brief description and their physical units.

Chapter 2 will briefly describe the state of the art of both flywheel energy storage systems and active magnetic bearings in general. In both sections the operational principle of the described systems is explained, including physical principles involved.

Chapter 3 describes the flywheel prototype in which the project is based on, as well as the characterization process carried out to build a simulation model.

Chapter 4 describe the hardware that is going to be used for the implementation of the levitation control. Even though this project focuses in the control of axial magnetic bearings, the hardware for the radial magnetic bearings has been developed for future use.

Chapter 5 deals with the design of the vertical levitation control system. The chapter starts with the design specifications, then both current and position control systems are explained, and finally the simulation results are presented.

Chapter 6 contains the experimental results resulting from the implementation of the control system in the laboratory setup.

Chapter 7 summarizes all results obtained in this project, pointing out the rooms for further research within this project.

Finally, *Appendix A* contains the details of the digital implementation of the control system in DSP platform, as well as the description of the main operating modes included in the real-time software developed.

References are included at the end of the document.

Chapter 2

State of the Art

2.1 Flywheel Energy Storage Systems

2.1.1 Operational principle

The final goal of the FESS is to serve as a bidirectional energy buffer, which realizes the energy conversion from electrical to kinetic and vice versa, therefore being able to store or release energy, respectively, depending upon demand.

By making use of the electrical machine, the flywheel is able to store energy when the electrical machine is acting as a motor. Therefore, the absorbed electrical energy will be converted into kinetic energy and the flywheel will be accelerated.

When the energy needs to be released, the machine operates as a generator, extracting the kinetic energy and converting it back into electricity, by reducing the flywheel rotational speed.

Equation (2.1) shows how can the kinetic energy stored can be calculated based on the flywheel moment of intertia and the rotational speed.

$$\Delta E_c = \frac{1}{2} I_z (\omega_{max}^2 - \omega_{min}^2) \tag{2.1}$$

where:

E_c: increment of kinetic energy $[J]$

J: Rotor moment of inertia with respect rotation axis $[kg \cdot m^2]$

ω: rotational speed of the rotor $[rad/s]$

The rotational speed of the flywheel is limited to a maximum speed ω_{max}, due to maximum flux weakening capability of the PM machine, control constraints or eventually mechanical integrity of the flywheel, while the minimum limit has to do with the rating of the power delivery converter.

The energy conversion process is shown in figure 2-1:
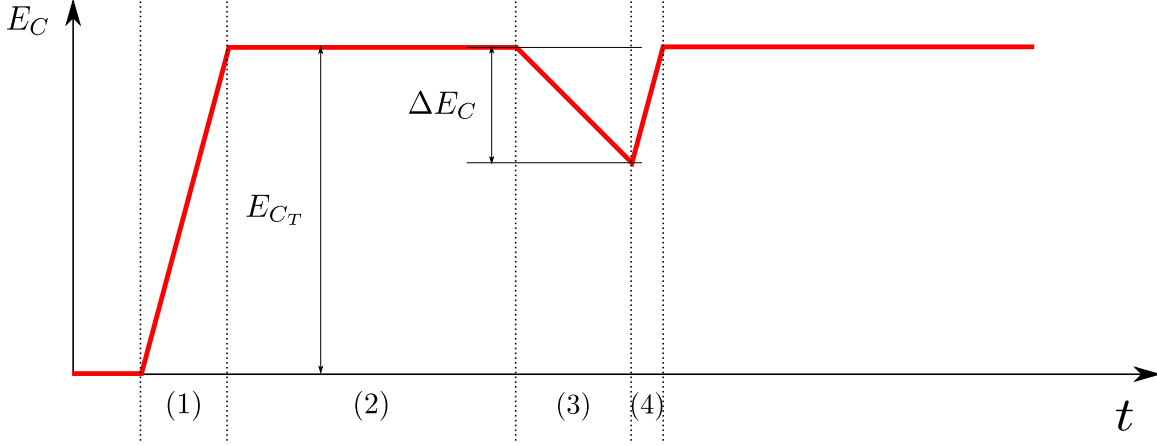
Figure 2-1: Kinetic energy versus time along the energy conversion process.

The process shown in the above figure can be described as follows:

1. Being initially stopped, the flywheel is accelerated until the nominal speed by absorbing electrical energy from the external source.

2. Once the nominal speed is reached, the total energy stored ΔE_{C_T} remains nearly constant due to the negligible losses of the system and the absence of friction.

3. Whenever the energy is demanded, the electric machine starts operating as a generator, extracting the stored energy in the flywheel while decreasing its speed. The extracted energy ΔE is the increment of kinetic energy extracted ΔE_C converted back into electrical energy through the efficiency of the machine, thus:

$$\Delta E = \eta_{mach} \cdot \Delta E_C \tag{2.2}$$

24

The efficiency of the permanent magnet synchronous machine is high, around 95%.

4. Once the demanded energy is delivered, the flywheel recovers its nominal storage level by accelerating its speed up to the nominal.

Therefore, this operational principle allows the flywheel to control a bidirectional energy flow, providing a flexible solution for many energy storage applications.

2.1.2 Applications

Flywheel-based Energy Storage Systems (FESS) have a wide range of potential applications:

- **Renewable Energies:** one of the main issues associated with renewable energies, specially wind power, is the intermittent nature of source. Energy storage systems have a room of application in this field since they can help to match generation with demand. The system will store energy during the low demand hours, and release it during the peak hours, performing the so-called effect valley-filling or peak-shaving [29][24].

- **Power Quality:** voltage sags are by far the most harmful power quality issue, leading to malfunctioning of electronic equipment and causing high economical losses in factories. Energy storage systems such as flywheels can help to reduce these short dips in the voltage by injecting big amounts of power into the grid in the form of reactive power [30].

- **Traction applications:** flywheels system can be also applied to traction applications such as railway. They can be either placed on-board to supply energy when the catenary is not available, or stationary in the train station recovering energy during the braking of the trains. In fact, flywheel systems are the main part in Kinetic Energy Recovery Systems (KERS) used in motoring.

- **Aerospace and military:** due to its high power density flywheels are considered a suitable energy storage solution for military [21] and aerospace applications [31], where weight as well as safety issues are crucial.

This section will describe the characterization process carried out to properly control the levitation of the flywheel prototype. As an electro-mechanical system, the flywheel-based energy storage prototype is composed by several subsystems: electromagnetic, formed by the coils of the magnetic bearings; and mechanical, formed by the body of the flywheel or rotor and the permanent magnet ring. s This section will focus on the description of the axial magnetic bearings only, since the control of the radial bearings is out of the scope of this thesis. The geometrical properties of the system are given in a pre-designed 3D model.

2.2   Active Magnetic Bearings

Active Magnetic Bearings are able to withstand a load making use of the force generated by a magnetic field. Due to the fact that the load is supported without any friction, they offer significant advantages over the mechanical and fluid-based bearings, such as reduction of heat loss, lubrication systems or periodical maintenance, among others.

They not only represent a competitive advantage in terms of reliability but also in dynamic stiffness and position control accuracy, and response compared to traditional bearings, since they can be controlled actively to achieve improved dynamic performance [19][16].

In addition, they are the only feasible solution for high-speed flywheel energy storage systems, since the high speeds involved require active control as well as safety and reliable operation [6].

As a drawback they have a high cost and complex construction associated, as well as sophisticated control systems need to be developed for the application in such systems [19][26][16].

2.2.1 Magnetic Bearings physics

Magnetic bearings will generate the force to control the levitation of the flywheel. In order to generate a specific amount of force, a magnetic field needs to be created by feeding current into the coil of the bearing. However, the resulting force will not only depend on the current flowing but also in the gap between the coil and the flywheel, according to equation (2.3) [27][6]:

$$B = \frac{\psi}{A} = \frac{\mu_0 N i}{g} \tag{2.3}$$

where B is the magnetic field crossing the air gap area A, i is the inductor current and g is the gap between the inductor plane and the flywheel. The magnetic force can be calculated from the magnetic field as states equation (2.4) [27][6]:

$$\mathbf{F} = \frac{\mathbf{B^2}}{2\mu_0} A \tag{2.4}$$

Therefore, the expression for the magnetic force in terms of current and gap is (equation (2.5)):

$$\mathbf{F} = \frac{\mu_0^2 N^2 \mathbf{i^2}}{\mathbf{g^2}} \frac{A}{2\mu_0} = \frac{1}{2} \frac{\mu_0 N^2 \mathbf{i^2} A}{\mathbf{g^2}} \tag{2.5}$$

Notice from (2.5) that the direction of the current does not affect the direction of the force, meaning that the bearing will always produce an attractive force as long as there is current flowing.

Looking at the equation (2.5) from a different point of view, the current can be calculated to generate an specific force for a given gap, thus:

$$\mathbf{i} = \frac{\mathbf{g}}{N} \sqrt{\frac{2\mathbf{F}}{\mu_0 A}} \tag{2.6}$$

Equation (2.6) will provide the current reference to the current control loop in order to generate the demanded force taking into account the actual position of the flywheel.

2.2.2 Magnetic suspension system

To achieve this energy conversion process efficiently and due to the high rotational speeds involved, mechanical bearings cannot be used for this purpose, hence a magnetic levitation system must be used instead. The magnetic suspension system will make use of electromagnets to ensure frictionless rotation of the flywheel at high speeds.

Figure 2-2 shows a magnetic suspension system scheme, including its main parts.
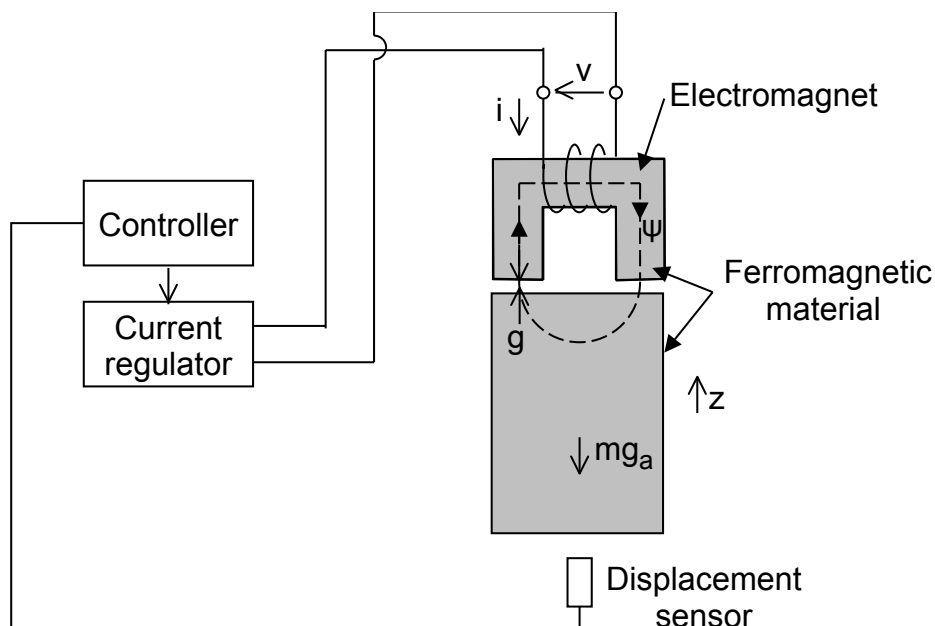
Figure 2-2: Magnetic suspension system [6].

It this case the rectangular mass of *Ferromagnetic material m* needs to be held in levitation along the vertical axis z. The *displacement sensor* measures the gap g between the mass and the *Electromagnet*, as a feedback signal to the *Controller*.

The *Current regulator* will calculate the instantaneous voltage v across the coil terminals necessary to make the desired current i to flow through.

The current reference is set by an external *Controller*, based on the position measurement so that the generated magnetic field produces the needed force to withstand the mass.

This basic example can be translated into the real system very similarly. In our case of study, the axial magnetic bearings are formed by a single coil that is actually

the electromagnet. By means of a controlled current flowing through the terminals, the electromagnet is able to withstand the weight of the flywheel in the levitation position while allowing frictionless rotation of the rotor with respect the housing.

The axial magnetic bearings must keep the flywheel in the levitation position, that is in the middle of the vertical gap between the bearings and the rotor, while the radial bearings keep the shaft precisely in the center of rotation. Mechanical bearings cannot be used for this purpose due to the very high rotation speeds that the system is intended for, that would cause very frequent bearings maintenance or even catastrophic failures.

2.2.3 Control Alternatives for active magnetic bearing systems

Magnetic suspension systems are naturally unstable systems, therefore a number of control strategies can be applied to tackle the problem. Magnetic bearings present a high non-linear behavior between the current injected and the force generated. Also, the variation of some system parameters such as the inductance associated to the position control is a challenging aspect that the control system must deal with.

Modern computational tools and Digital Signal Processors (DSPs) has enable the development of a number of control strategies, either linear or non-linear, to be implemented in real levitation systems. The different control alternatives are briefly described below [18]:

PID Control

It is a linear technique making use of the well-known classic control theory. The controller provides three different control actions: proportional, integral and derivative. The proportional action has to do with the mechanical stiffness, the integral eliminates the steady state error and the derivative deals with the mechanical damping, playing a major role in system stability .

PID Control is the most widely used for this kind of applications [2][13][22][35],

since it is relatively easy to tune and implement[7]. However the dynamic response can be sensitive to uncertainties and non-linearities of the system, since the classic control theory assumes that the mathematical model matches the physical model. The parameter sensitivity and the linear assumptions can deteriorate the dynamic response of the system, limiting the operation range of the magnetic suspension.

Robust Control

Unlike classic control methods, robust control methods are aimed to ensure a good dynamic performance dealing with the inaccuracy of the model. Robust control methods such as H_1, H_∞ or μ-synthesis can be applied to either linear or non-linear systems, as well as to $SISO$ or $MIMO$ systems [14]. They are based on input-output functions that deal with the disturbances as well as with the parameter variations[2][7][1][28][20].

Adaptive Control

In this case the the controller parameters are updated online according to the variation in the parameters of the physical system. They are usually carried out either calculating the controller coefficients based on physical parameters or using interpolation methods [14][34][33].

Fuzzy Control

The idea behind this control strategy is to define the behavior of the physical system using linear combinations and weightings of control variables. The parameters of the control are adjusted with statments in the form *if then* [14][7][5].

Neural Networks

Similarly to the biological neural networks, these kind of control system has a number of intermediate layers between input and output layers. Each layer is connected with the surrounding network, which performs a weighted sum of the inputs. The weightings are optimized in order to model the behavior of the physical system [14][17][3].

Optimal Control

This technique is commonly used for optimization problems in process control. After the problem is solved, the control actions are calculated to maximize certain objective function [4].

Comparison of control alternatives

Table 2.2.3 compares the different control alternatives in terms of lower oscillation, robustness, reference tracking and simplicity [14][7]:

Type	Lower Oscillation	Robustness	Ref. Tracking	Simplicity
PD Control	$+$	$++$	$++$	$+++$
Fuzzy Control	$+++$	$+$	$+++$	$++$
H_∞ Control	$+$	$+++$	$+$	$+$
Fuzzy PD Control	$++$	$++$	$+++$	$++$

Table 2.1: Comparison chart of control alternatives for active magnetic bearings [14][7].

According to [7], PD control and H_∞ presents the higher overshoot. In terms of reference tracking, fuzzy PD control presents the best performance whereas H_∞ is the poorest. However, H_∞ is the most robust when dealing with position control under rotation.

In this project a new control approach will be proposed, combining linear and adaptive methods.

Chapter 3

System Description and Identification

3.1 Description of the energy storage system

The Flywheel-based Energy Storage System (FESS) is based on a cylindrical steel-made flywheel supported by magnetic bearings and a permanent magnet, all enclosed in a steel housing. The flywheel is actually the external rotor of a surface-mounted permanent magnet machine, which stator is embedded in the system. Magnetic bearings and magnet ring are attached to the housing as well as the stator, only flywheel and its shaft are the moving parts.

The flywheel prototype is shown in picture 3-1:

Figure 3-1: Flywheel-based energy storage system prototype.

The axial magnetic bearings along with the magnet ring will provide the vertical force to keep the flywheel in levitation, while the radial magnetic bearings will provide the force to keep the shaft centred. Thus, the flywheel will be in complete levitation hence allowing for frictionless rotation.

Figure 3-2 shows a cross section of the FESS, with the main parts tagged.
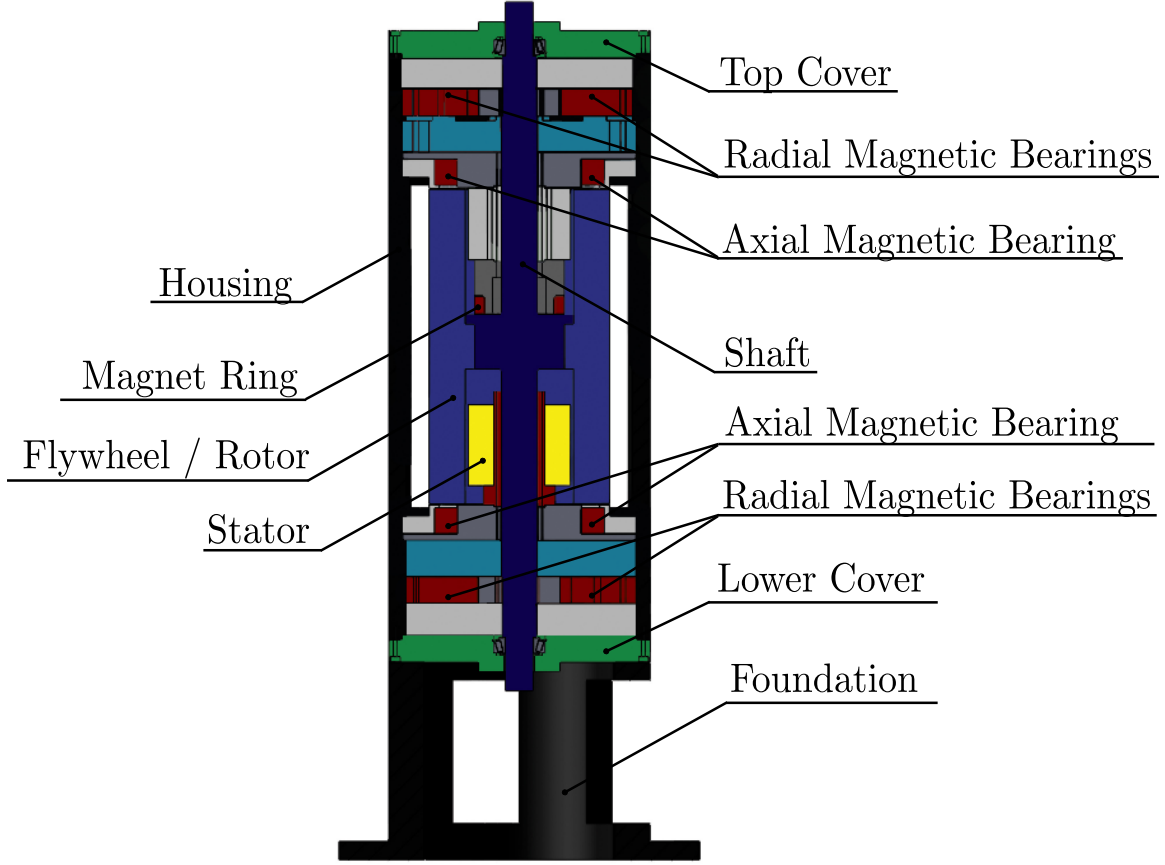
Figure 3-2: Cross section of the Flywheel-based Energy Storage System (FESS).

- **Flywheel:** is the main component of the system, where the energy is stored in form of kinetic energy. The flywheel body is a steel-made hollow cylinder attached to a shaft. It stores energy in form of kinetic energy by rotating around the shaft as fast as possible.

  - Mass: $m = 68.864\ kg$

  - Moments of inertia: $I_z = 0.3868\ kg \cdot m^2$; $I_y = I_x = 1.0472\ kg \cdot m^2$

  - Rotor outer diameter: $\phi_{r_{ext}} = 160\ mm$

  - Rotor inner diameter: $\phi_{r_{int}} = 120\ mm$

  - Shaft height: $l = 767\ mm$

  - Flywheel height: $h = 350\ mm$

- **Axial magnetic bearings:** are formed by two wounded toroidal coils, located in top and bottom positions, and they are responsible for generating the force to withstand the rotor in the vertical levitation position. The constructive data are gathered below:

    – Copper wire conductor: $\phi_{Cu} = 1.8\ mm$

    – Outer diameter: $\phi_{b_{ext}} = 187\ mm$

    – Inner diameter: $\phi_{b_{in}} = 139\ mm$

    – Flux area: $A = 122.9\ mm^2$

    – Width: $l_b = 28\ mm$

    – Turns: $N = 130$

Figure 3-3: Axial magnetic bearing coil.

- **Radial magnetic bearings:** consist of three coils or poles equally located around the shaft. They are in charged of apply the magnetic force to keep the shaft in the center of rotation. There are two sets of radial bearings in top and low position of the shaft.
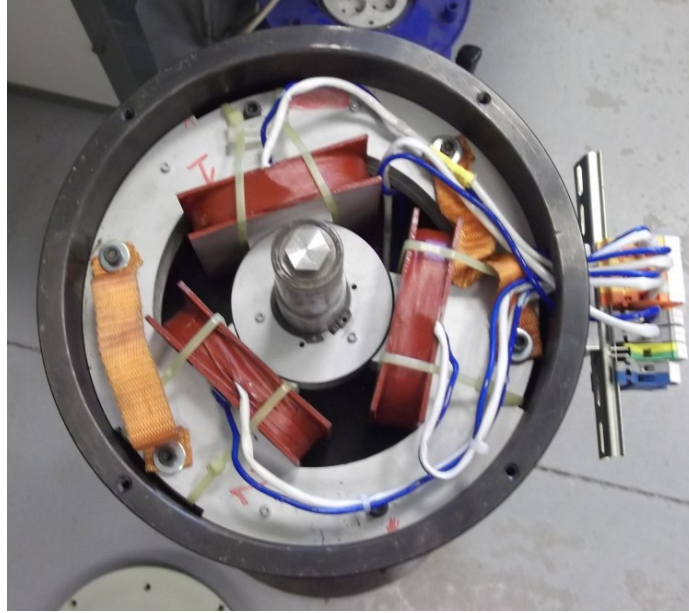
Figure 3-4: Radial magnetic bearings.

- **Magnet ring:** the housing contains embedded a Neodymium permanent magnet ring embedded and fixed to the housing. This high-field rare earth magnet is aimed to withstand most of the weight of the rotor when it is in the levitation position, in order to decrease the current demand of the magnetic bearings, therefore increasing system efficiency.

- **Electric Machine:** the flywheel is actually the external rotor of a surface-mounted permanent magnet synchronous machine which stator is inside the lower part of the flywheel hollow. It is a 2-pole machine with nominal speed of 3000 rpm.

- **Covers:** The top and lower aluminum cover will have attached the Hall-effect position sensors: two for horizontal plane and one for vertical, in both top and lower cover, counting six in total. The axial position sensor measures the vertical position of the screw attached to the shaft, whereas the radial sensors measure directly onto the shaft surface.
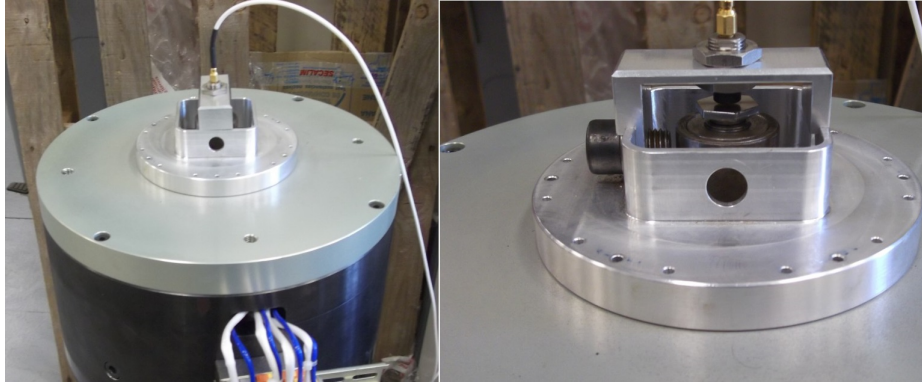
Figure 3-5: Top cover with position sensor attached.

- **Housing:** a steel-made container for the whole system. The top and lower covers have a hole from which the shaft comes out, and where the position sensors are attached in order to measure the position of the shaft. Finally the housing has a three-leg steel-made foundation, which includes a conic pedestal able to manually elevate the flywheel when embed to the shaft screw hole. This pedestal can be used to set the initial vertical position of the flywheel before levitation.
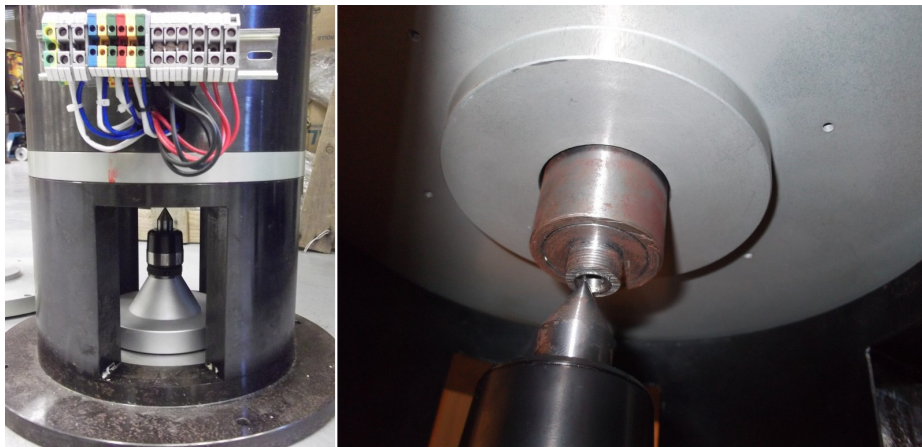
Figure 3-6: Conic pedestal.

3.2 System identification

3.2.1 Electromagnetic System

Focusing on the axial bearings, the electromagnetic system will be composed of two coils forming the bearings, as well as the permanent magnet ring. Identical constructive features will be assumed for the coils, which have been detailed in section 3.1. For the following section, the magnetic bearings will be looked as inductors rather than force generators.

Coil identification

In order for the current to be properly controlled, coil parameters need to be identified, namely resistance and inductance. These parameters have been estimated experimentally by applying a voltage step to the coil and analyzing the resulting response.

Ideally, the coil can be characterized by applying a voltage step as a input and looking at the current response. This system will provide a first-order response according to the transfer function of the R-L circuit:

$$G_0 = \frac{1}{L \cdot s + R} \tag{3.1}$$

In this case, the voltage across the coil terminals has been applied using the power converter. In order to have a flat voltage as an input, the converter is controlled with the duty varying each 0.5 seconds from 0.5 to 1. In order for the current not to be very high, the DC-bus is set to 3.4 Vdc which corresponds to 2A peak current circulating through the coil. The results are shown in figure 3-7:
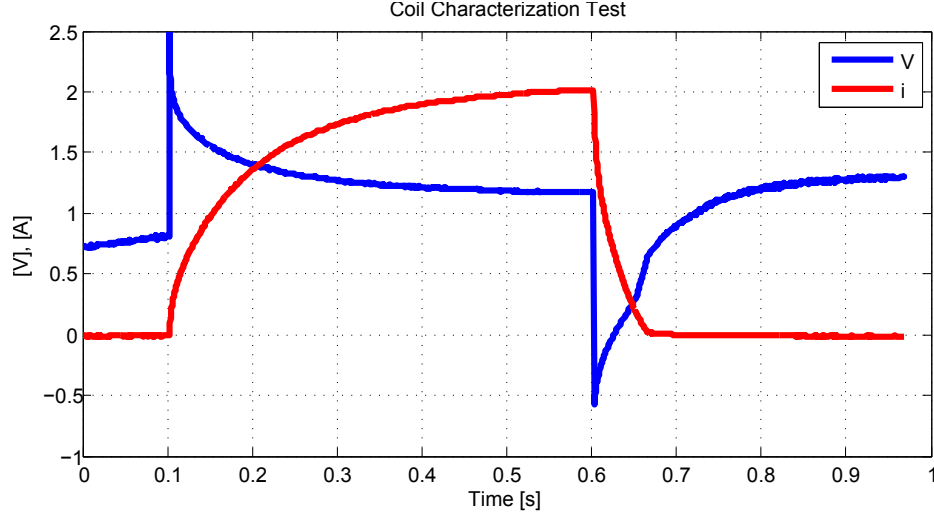
Figure 3-7: Coil characterization experimental test data: input voltage and current response.

As it can be appreciated from figure 3-7, the voltage waveform is not squared but has a voltage spike. It needs to be remarked that during this test the flywheel was static, so no voltage could have been induced by the flywheel movement. This is instead due to the fact that the voltage is affected by the impedance of the voltage source used for the test. Nevertheless, this effect does not have an impact in the identification process, since the input does not necessary have to be a voltage step.

This experimental data have been fit to the afore-mentioned first order transfer function (3.1), obtaining the coil parameters, obtaining in this case:

$$L = 97.2 \ mH$$

$$R = 0.5 \ m\Omega$$

This values are considering no gap between the coil and the flywheel.

Figure 3-8 shows an overlaid plot of the experimental response and the model response.
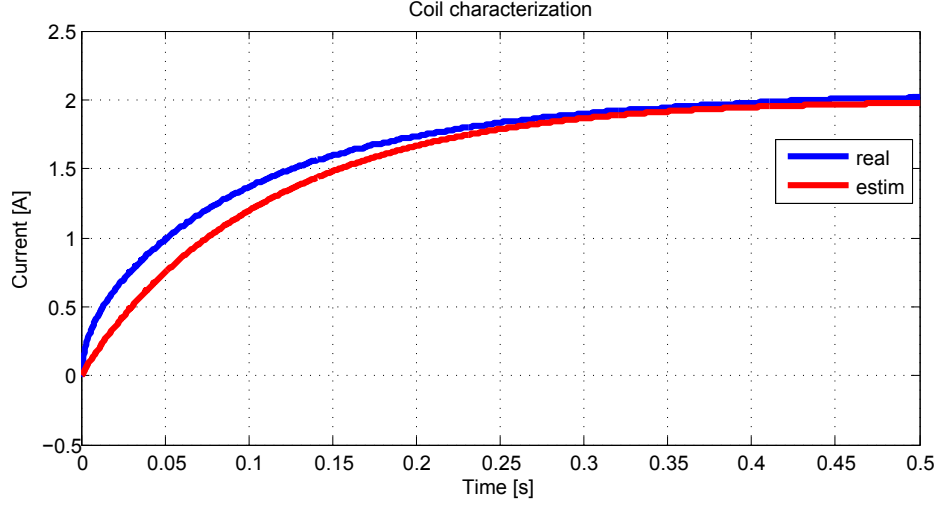
Figure 3-8: Coil characterization: overlaid current response comparison.

The real response in figure 3-8 (red) has a slightly higher rise time compared to the estimated response (blue). This is caused by the initial spike in the voltage across the coil terminals.

Inductance variation with gap

However, the inductance of the coils strongly depends on the gap between the flywheel and the coil, since the path for the magnetic flux is affected. In order to check for the impact of the gap in the inductance of the coils, the above process has been repeated for a number of gaps making use of the manual pedestal to place the rotor at several positions.

Table 3.2.1 gathers the obtained values for the conducted experiments.

Inductance	Gap
$L[mH]$	$g[\mu m]$
97.2	0
71.1	300
61.1	600
58.3	900
55.3	1200
43.7	2250

Table 3.1: Inductance variation with gap.

Afterwards, the results have been plotted and interpolated by a squared polynomial giving the following relation between gap and inductance:

$$L = 1.326 \cdot 10^{-8} \cdot g^2 - 5.049 \cdot 10^{-5} \cdot g + 0.09148 \tag{3.2}$$

Gap g is expressed in μm.

The result of such interpolation is shown in Figure 3-9:
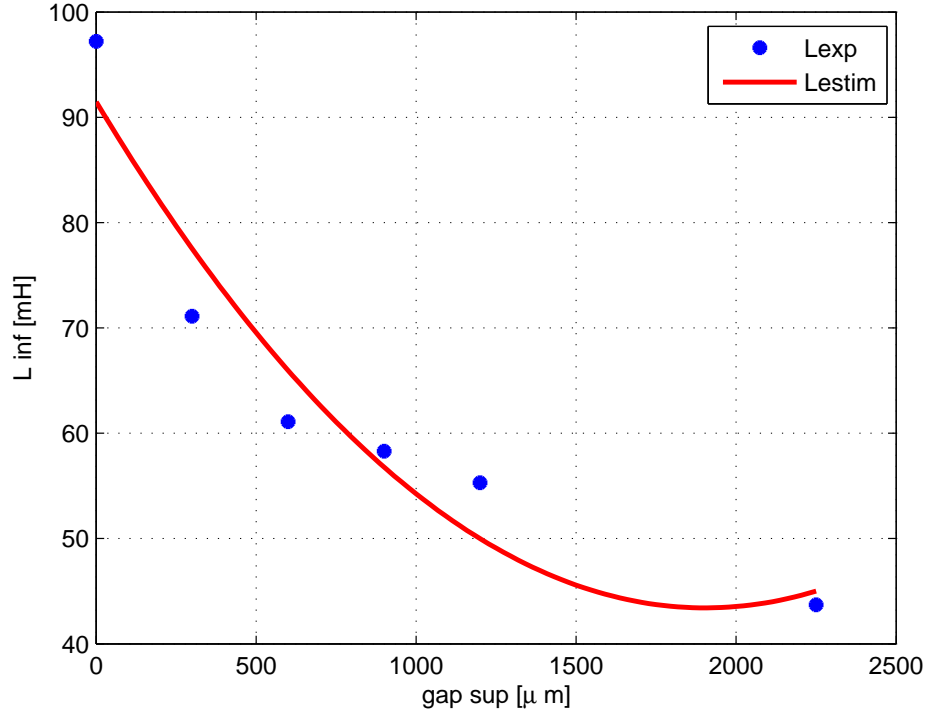
Figure 3-9: Inductance variation with gap.

This relation will be used for the control system to adjust the controller parameters online as an adaptive controller.

Induced Voltage

Due to the variation of the inductance associated with the flywheel movement, an induced voltage appears across the coil terminals, according to:

$$u(t) = R \cdot i(t) + \frac{d}{dt}[L(t) \cdot i(t)] = \underbrace{R \cdot i(t)}_{V_R} + \underbrace{L \cdot \frac{d}{dt}i(t)}_{V_L} + \underbrace{i \cdot \frac{d}{dt}L(t)}_{b.e.m.f.} \tag{3.3}$$

The back electromotive force (b.e.m.f.) tries to oppose any change in the inductor current, so an induced voltage appears trying to bring down the applied voltage V_L which causes the current variation.

In our system, the derivative of the inductance with respect to time occurs when the flywheel is moving, since the inductance varies with gap. Since the magnetic circuit parameters are not well defined and the mechanical geometry is very complex, an experimental approximation of the back electromotive force will be done, trying to find out a relation with the flywheel speed.

Experimental test

To do so, the flywheel will be lifted by injecting current in the upper magnetic bearing. Due to the displacement, an induced voltage will appear in the terminals of the lowest magnetic bearing, and thus the back electromotive force will be recorded.

In this case the current is injected with a controlled voltage source with current limit, applying 20 V to the upper coil terminal. The current will start flowing into the upper coil and producing an increasing force until the flywheel is lifted to the top position.

Figure 3-10 shows the results of the experimental test:
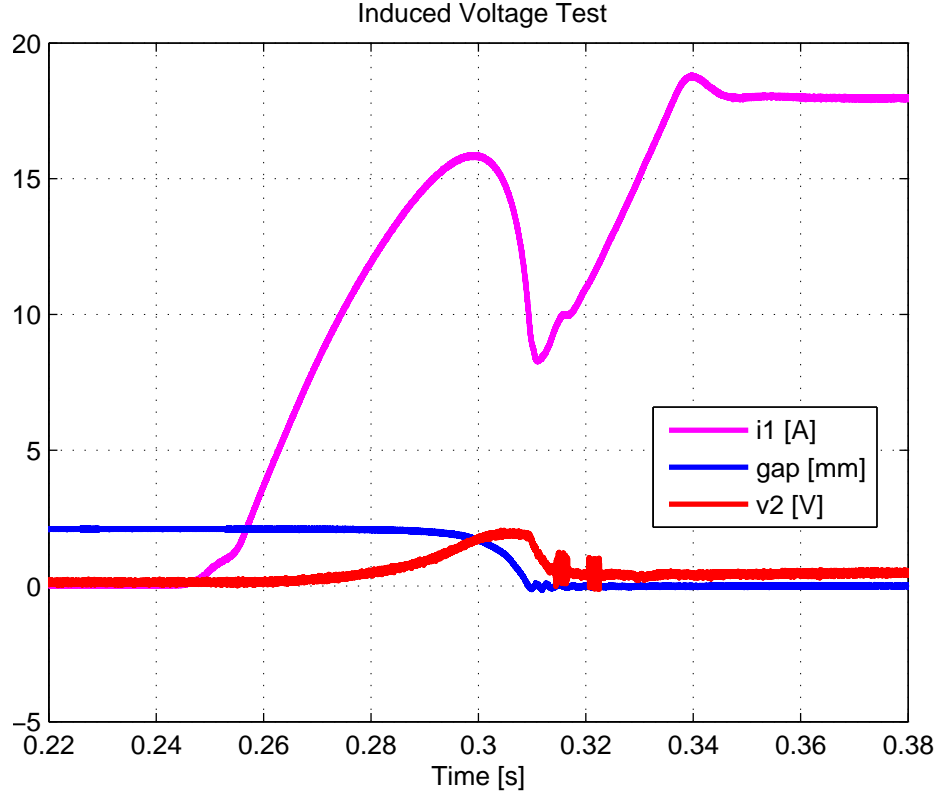
Figure 3-10: Induced voltage test: experimental data. Current in the top bearing $i1$ (magenta), upper gap in milimeters (blue), induced voltage in the lowest bearing (red).

The current is increased as soon as the voltage is applied to the upper coil terminals (not shown). Therefore, the force generated by the upper magnetic bearing increases, until the the flywheel takes off and starts lifting. As the flywheel is moving, the induced voltage starts increasing, making the current to decrease due to the aforementioned effect. Finally when the flywheel reaches the top position, the current in the upper coil starts increasing again until the current limit of the voltage source.

With the record of the induced voltage along with the vertical displacement measurement, a data post-processing will be carried out in order to figure out the relation between the vertical speed and the induced voltage.

Data post-processing

Focusing on the part where the movement takes place, the experimental data is passed through an moving-average statistical filter to remove noise without affecting the measurements.

Figure 3-11 shows the result of the gap signal filtered out.
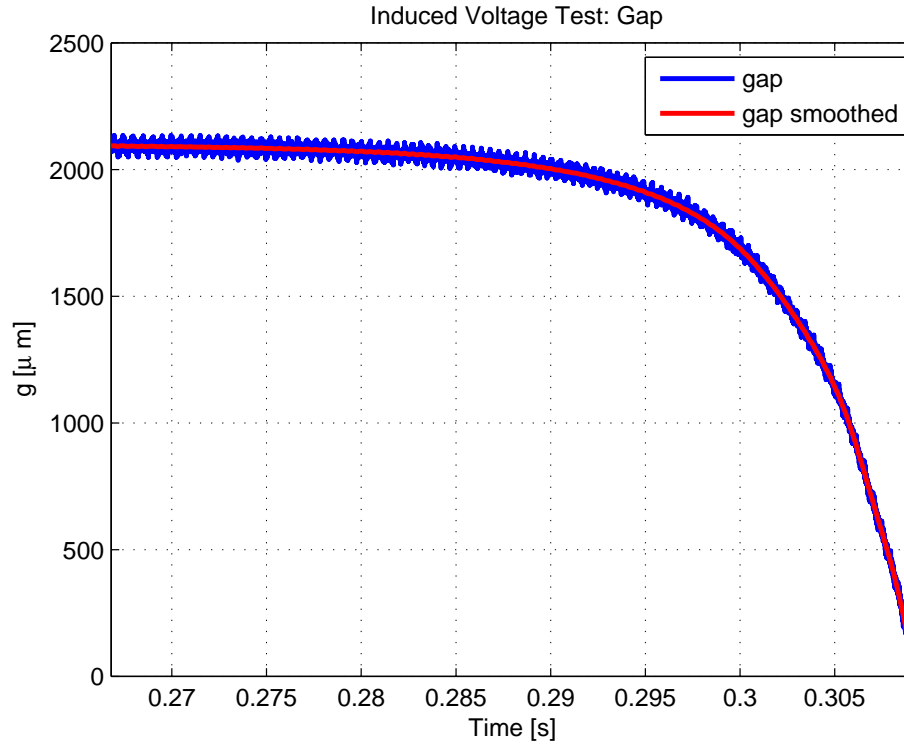
Figure 3-11: Induced voltage test: gap. Current in the top bearing $i1$ (magenta), upper gap in milimeters (blue), induced voltage in the lowest bearing (red).

In order to get the vertical velocity, a derivative process has been applied to the displacement measurement. The result is again filtered out to remove the inherent noise caused by the derivative of a sampled signal.

The velocity obtained is shown in figure 3-12:
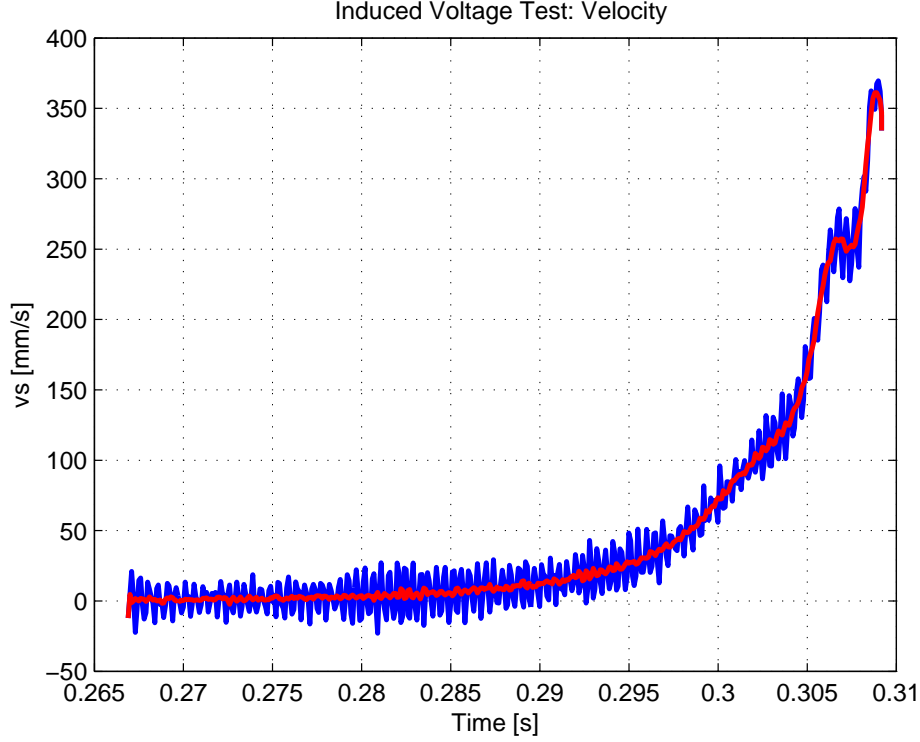
Figure 3-12: Induced voltage test: Vertical velocity. Velocity obtained from experimental data (blue), filtered velocity (red).

Once the velocity and the induced voltage are obtained, both signals are plotted together and the relationship is estimated by a third-order polynomial. Figure 3-13 shows the results.

As it can be appreciated from Figure 3-13, the estimation works reasonably accurately for vertical velocities lower than 200 mm/s. Notice that the values of the induced voltage are really low compared to the applied voltage (50 V maximum), so in any case it will not affect significantly the current control. Moreover, it has to be kept in mind that the test has been made in open-loop conditions, applying a high force into the top bearing, which leads to a sudden lift of the flywheel. The vertical velocity in controlled operation will be significantly lower.

It should be also pointed out that the fact that the induced voltage remains constant for high values of velocity might lead to confusion. This is caused due to the effect of focusing the post-processing in the movement part of the test, removing the part of the experiment where the derivative of the position goes back to zero (flyhweel
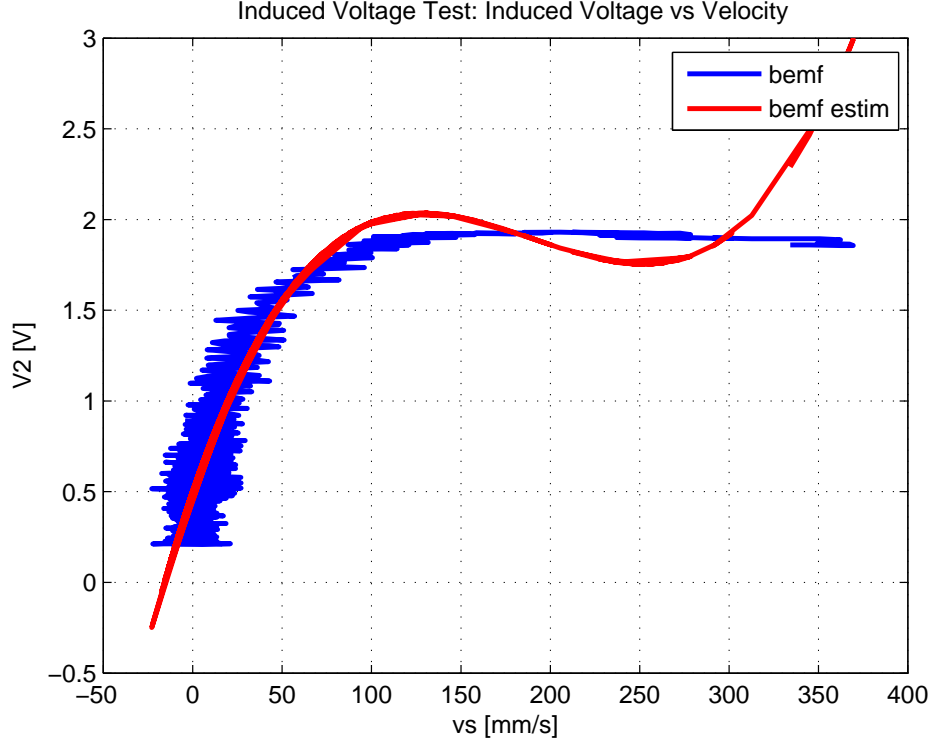
Figure 3-13: Induced voltage test: Induced voltage versus velocity. Experimental back electromotive force (blue), estimated back electromotive force (red) with third-order polynomial.

stopped in top position). The velocity estimation has to be performed only in the part of the test where the flywheel is moving to find out the relationship between velocity and induced voltage.

Therefore, the third-order polynomial approximation can be assumed to be provide a reasonably accurate assessment of the induced voltage, which will be introduced in the simulation model as a disturbance for the applied voltage to the coil terminals.

3.2.2 Mechanical System

The mechanical system is basically composed of the flywheel body as well as the permanent magnet ring embedded. The transfer function of the body of the flywheel is according to First Newton's Law:

$$G_{mech} = \frac{z}{F s} = \frac{1}{m \cdot s^2} \tag{3.4}$$

47

The transfer function for purposes of levitation has the applied force F_s as input and the vertical position z as output.

This transfer function is inherently oscillatory without any friction term. However, the presence of the magnet makes the system unstable, since the magnet produces a positive feedback from position to force, that is a force is increasing with the movement.

Figure 3-14 shows the block diagram of the mechanical system:
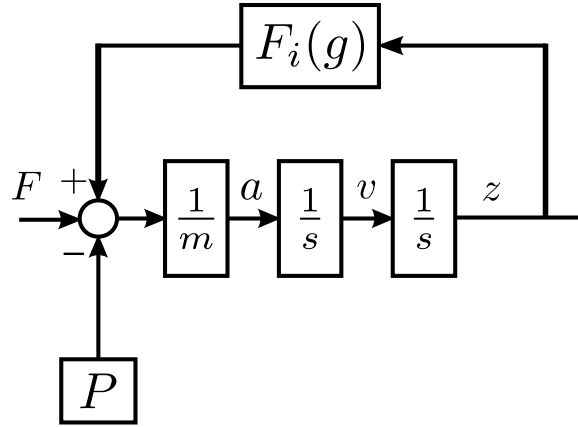
Figure 3-14: Block diagram of the mechanical system.

F represents the input force applied to the system, positive in the direction of increasing z, P is the weight of the flywheel and $F_i(g)$ is the force of the magnet.

Therefore, it is crucial to properly identify the magnet ring, which has strong influence in the dynamic response of the mechanical system due to its high strength.

Permanent magnet ring

The complexity of the mechanical system, including various materials, components shapes and numerous gaps, as well as the lack of information about the magnet properties makes very difficult to tackle the problem from the theoretical approach. Therefore, an experimental procedure has been followed to determine the force of the permanent magnet ring based on the evolution of the flywheel position during an attraction test.

The variable of interest in this case is the force as a function of the gap between

the flywheel and the magnet. The magnetic force comes as a result of the magnetic field generated by the permanent magnet, which is variable with the position.

Attraction force test

In order to extract the relation between the force and the gap, a laboratory test will be conducted taking advantage of the conic pedestal to manually vary the flywheel height. The test will make the magnet to attract the flywheel, while recording the position measurement for further study. To do so, the pedestal will be manually moved taking the flywheel from the lowest position to the top during a gradually and slowly lifting.

At some point, the magnet force will be higher than the weight of the flywheel, attracting it to the top position rapidly. Capturing the evolution of the position measurement, the magnet force will be calculated after the data post-processing. This experiment will provide the isolated force of the magnet as a function of the gap, with no possible magnetic coupling effects cause by the magnetic bearings since no current is flowing through them.

The manual lifting of the flywheel up to the attraction point has been done as slowly as possible in order not to disturb the derivative of the position, in order not to affect the derivative of the position. Thus the movement will be only caused by the attraction force of the magnet.

Figure 3-15 shows the output of the position sensor translated into distance using the conversion rate of the sensor (0:10 V / 0.3-3.3 mm). The so-called gap in the vertical axis represents the air gap between the flywheel and the magnet ring, when going from the lower to the top position.
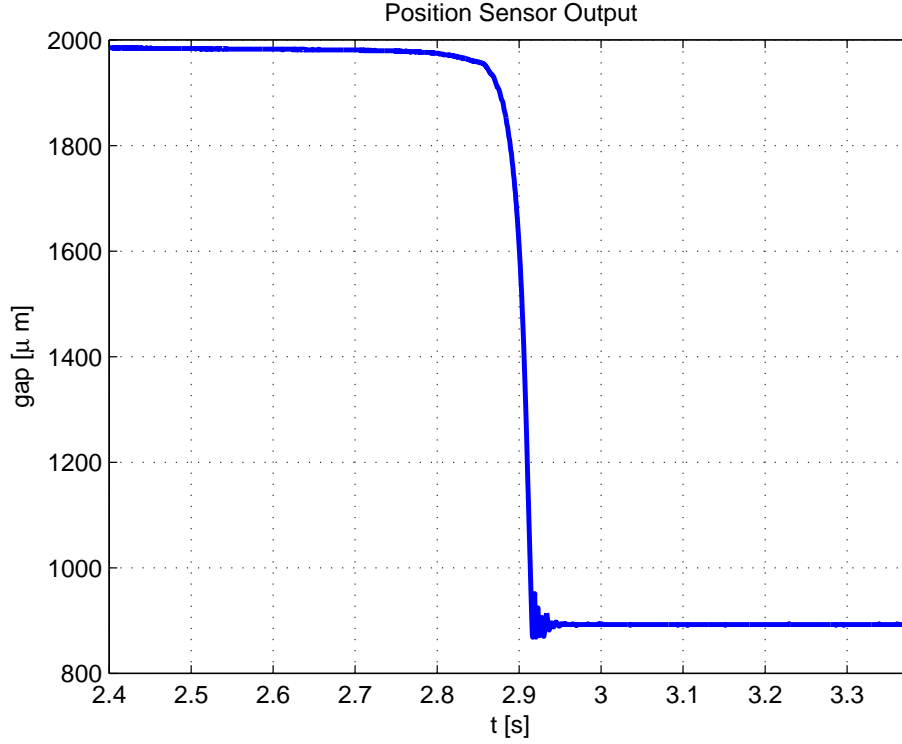
Figure 3-15: Experimental data recording of the position evolution during magnet attraction force test.

Experimental data post-processing

Based on the position evolution recorded in the test, a data processing applied consisting on several derivatives, in order to get first velocity and then acceleration, which is in turn proportional to the magnet force by the mass of the flywheel. Since the position measurement is sampled, the derivative process requires filtering to minimize the inherent noise associated. The several filtering processes have been selected so that the nature of the data is not significantly distorted.

Figure 3-16 shows the gap measurement zoomed into the movement area and subtracting the position offset introduced by the distance from the sensor tip to the screw plate.
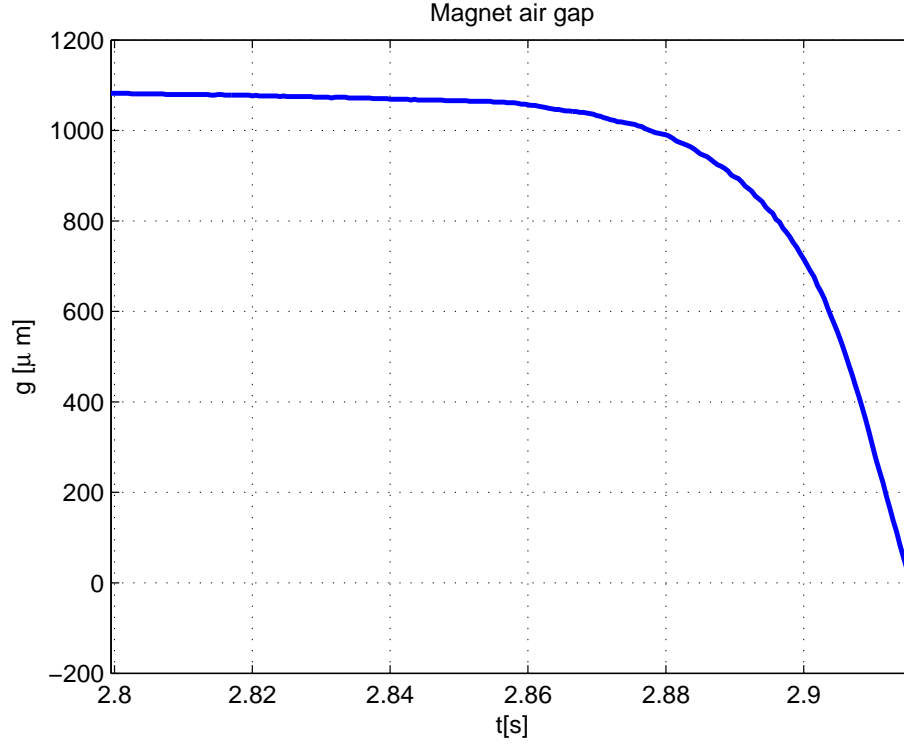
Figure 3-16: Gap evolution during the magnet force attraction test.

A derivative process is applied to the gap evolution in order to get the velocity, represented in Figure 3-17.

Due to the sampled nature of the position, the figure shows an overlaid plot of the filtered signal as well as a polynomial approximation.

The velocity presents a change in the derivative in the final part due to the ringing in the position signal caused by the impact of the flywheel against the magnet. This effect is amplified as the derivative processes are applied, giving a misleading signal for the force with a decrease in the force for low gaps that is not real. This issue makes very difficult to work out the magnet force for gaps very close to the magnet using this method.

The low-pass-filtered signal was chosen to carry on with the derivation process, leading to the acceleration signal shown in Figure 3-18:
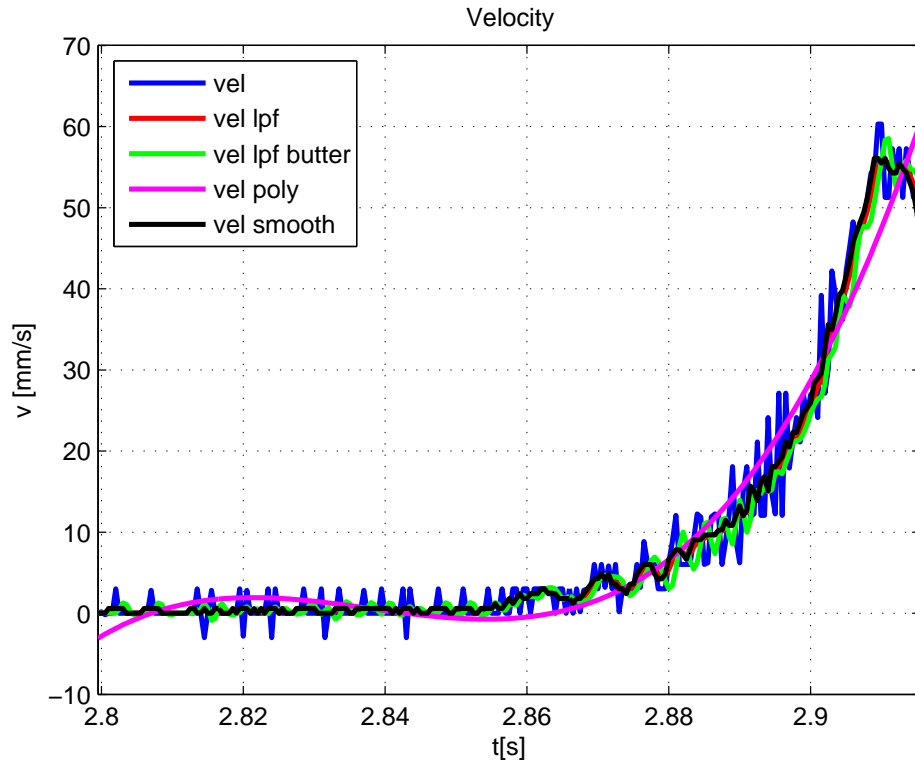
Figure 3-17: Velocity evolution and overlaid approximations during the magnet force attraction test: rough velocity (blue), 500 Hz low-pass-filtered velocity (red), 2nd order Butterworth 400 Hz low-pass-filtered velocity (green), cubic polynomial velocity approximation (magenta).
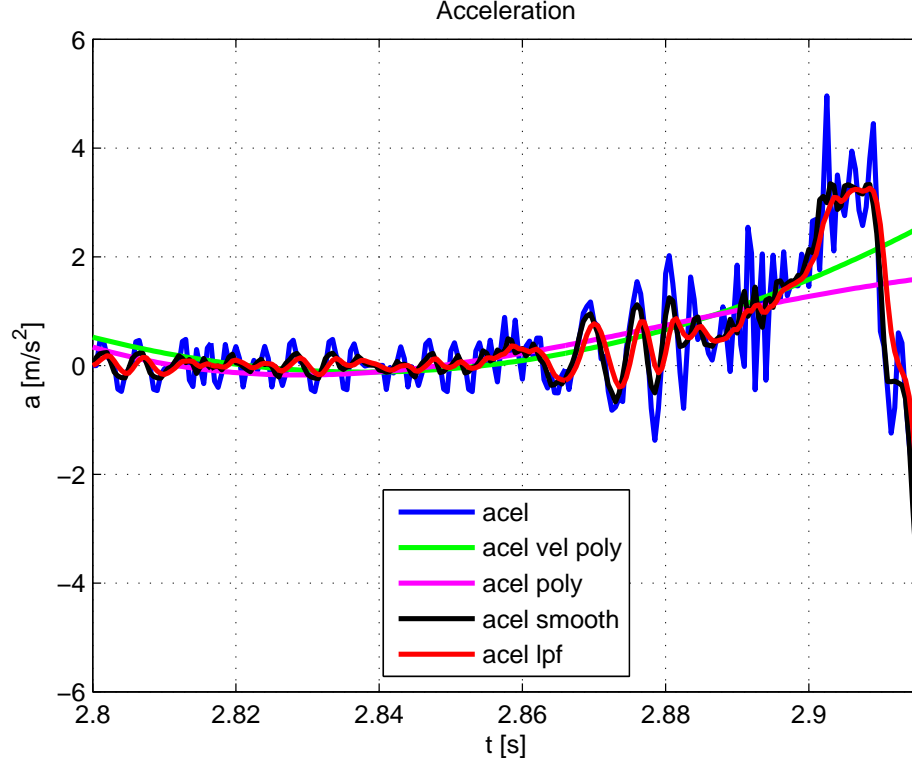
Figure 3-18: Acceleration evolution and overlaid approximations during the magnet force attraction test: rough acceleration based on low-pass-filtered velocity (blue), acceleration based on derivative of velocity polynomial approximation (green), acceleration polynomial approximation of 300 Hz low-pass-filtered acceleration (magenta), 300 Hz low-pass-filtered acceleration (red).

Once the acceleration signal is obtained, the magnet force is worked out, applying the First Newton's Law:

$$\sum F = F_i - P = m \cdot a \rightarrow Fi = m \cdot a + P \tag{3.5}$$

where F represents the resulting force causing the movement, m is the mass of the flywheel and P its associated weight and F_i the permanent magnet force. The obtained signal over time is shown in Figure 3-19.
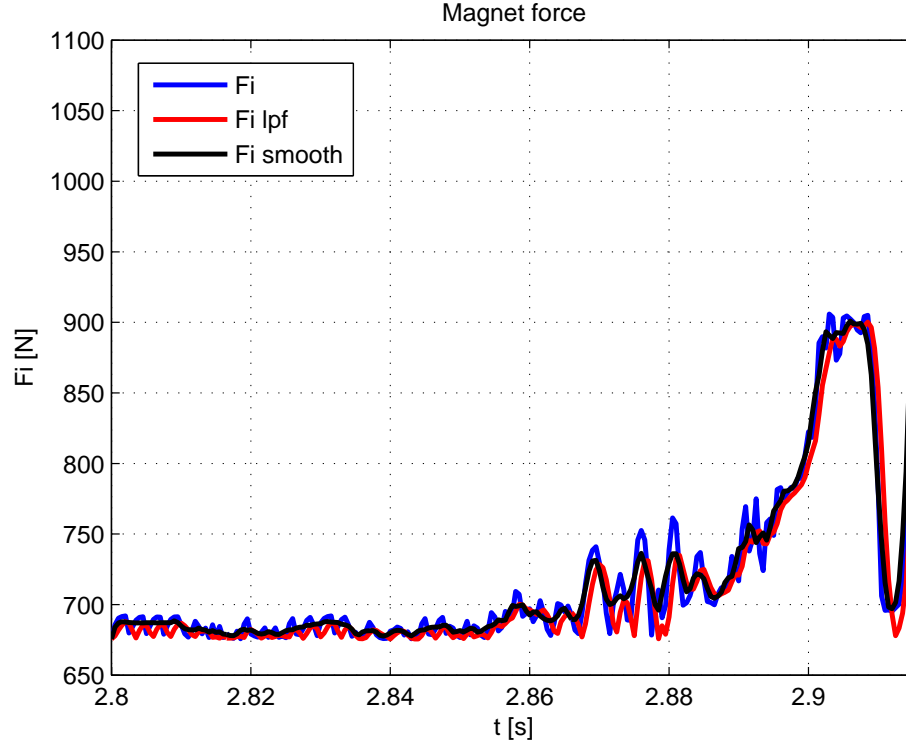
Figure 3-19: Magnet force overlaid plot over time during the magnet force attraction test: rough magnet force (blue), magnet force based on low-pass-filtered acceleration (red), magnet force based on acceleration polynomial approximation (magenta).

As mentioned before, the decrease of the force in the final part of the signal is just a consequence of the several derivative processes applied to the position signal.

Finally, Figure 3-20 represents the magnet force versus gap signal, along with different approximations.
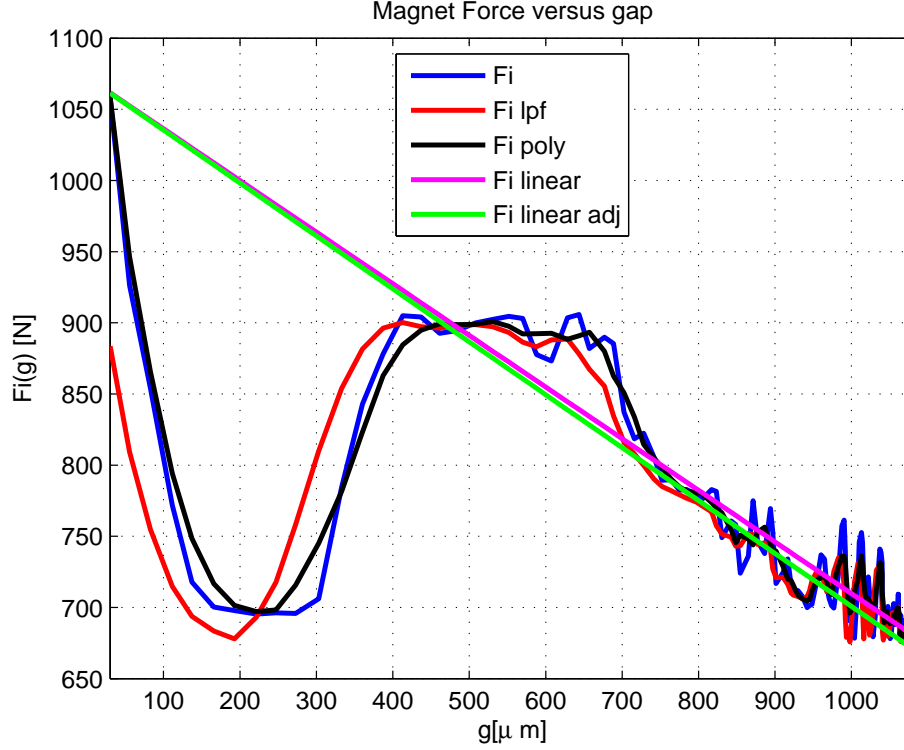
Figure 3-20: Magnet force overlaid plot versus gap during the magnet force attraction test: rough magnet force (blue), magnet force based on low-pass-filtered acceleration (red), magnet force based on acceleration polynomial approximation (magenta), linear approximation of the magnet force (black), linear approximation of the magnet force with experimental adjustment (green).

Once the natural response of the model has been tested, the magnet linear approximation has been slightly adjusted to match the experimental results. The adjusted linear approximation corresponds to the green line in figure 3-20.

Finally, the magnetic flux intensity produced by the magnet has been also estimated by applying the corresponding equation (2.4). Each of the plots in figure 3-21 is associated to its corresponding force estimation from figure 3-20.
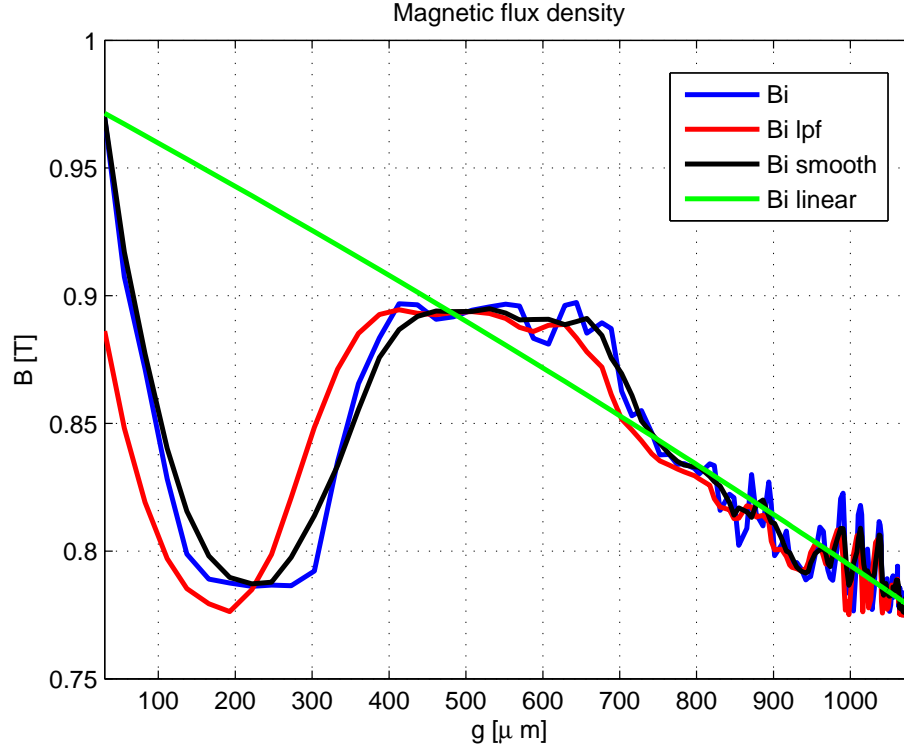
Figure 3-21: Magnetic flux density overlaid plot versus gap during the magnet force attraction test: rough magnetic flux density (blue), magnetic flux density based on low-pass-filtered magnet force (red), magnetic flux density based on magnet force polynomial approximation (magenta), magnetic flux density based on linear approximation of the magnet force (green).

The magnetic flux intensity estimation will help to check for the saturation of the material if needed.

Mechanical Model Validation

Once the permanent magnet force is assumed to be estimated correctly, the mechanical model including the magnet will be validated by checking the natural reponse. The model response is simulated setting the initial position to the initial value of the magnet atraction test, in order to test the correspondence with the experimental results. Initially, the model response was significantly faster than the experimental response, meaning that either the force or the mechanical properties of the model were not estimated correctly.

This is due to the fact that the system is not considered to have any friction, i.e.

floating in vacuum. The friction in the real system takes place between the shaft and the inner part of the housing and covers, since the radial magnetic bearings were not operating by the time the test was done. To be more realistic, a friction term was added in order to match the model response with the experimental data.
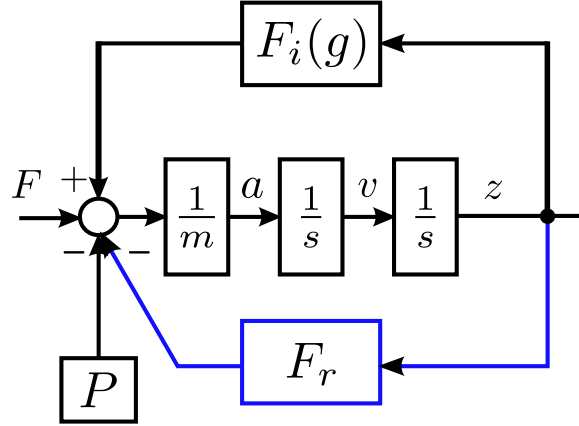
Figure 3-22: Block diagram of the mechanical system including friction term.

Another parameter to play with is the mass, since not accurate data for rotor material has been provided. A initial guess has been assumed for the mass using the density of steel F114 as an input to the 3D model, giving a mass of 68.8 kg. It has been slightly varied together with friction to match model and experimental data in several manual iterations.

Figure 3-23 shows plots for position and magnet force. The model response both with and without friction term are overlaid with the experimental data in order to test accuracy of the magnet force approximation.
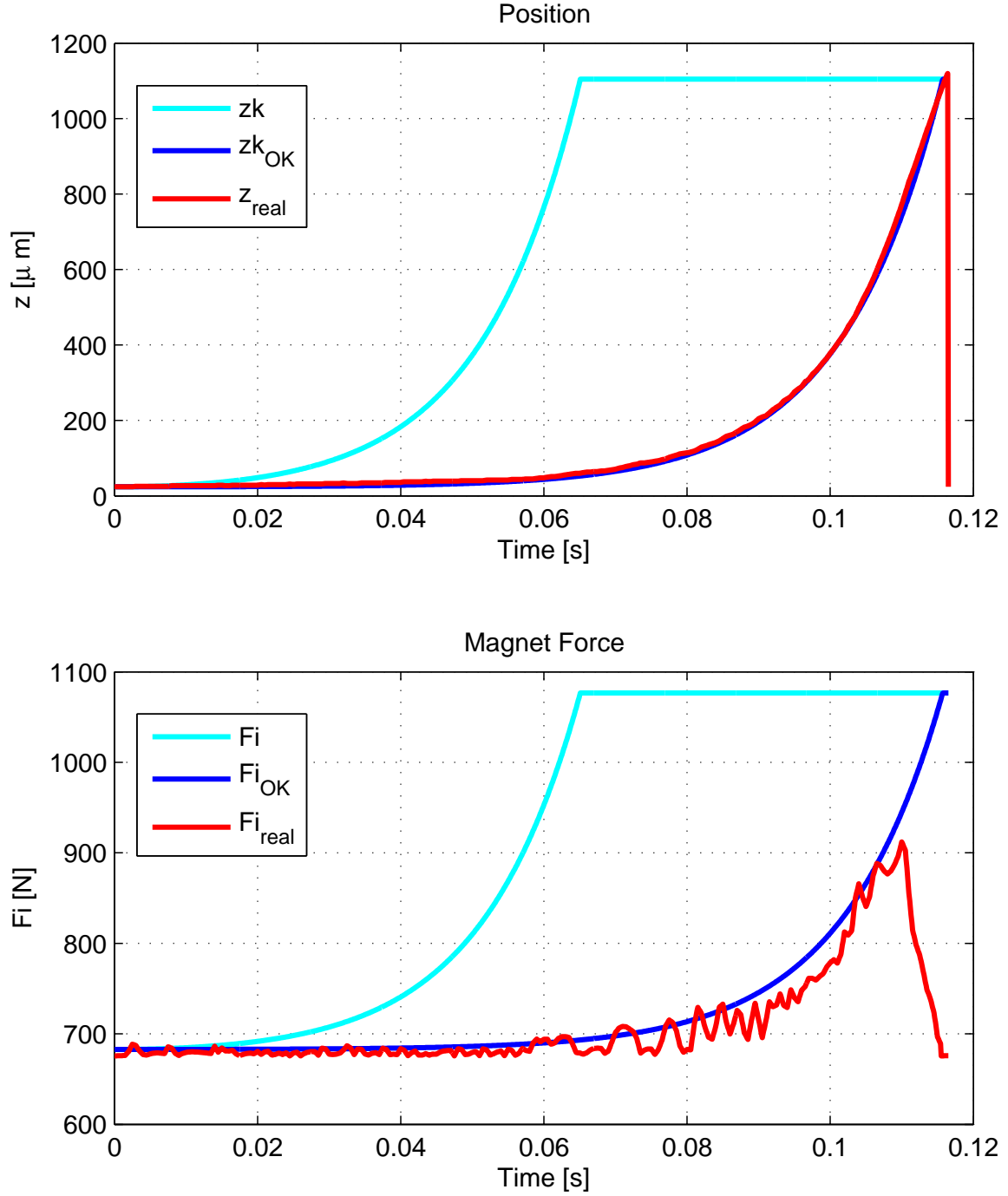
Figure 3-23: Natural response of the mechanical system in terms of position and magnet force. Experimental data (red), model response without correction (cyan), model response with friction and mass correction (blue).

As it can be appreciated from Figure 3-23, the model response matches the experimental results once the friction term is added adn the mass is slightly adjusted.

As mentioned before, the decrease in the final part of the experimental magnet force does not represent a realistic behaviour since it is caused by issues associated with the derivative process carried out to calculate this force.

3.2.3   Magnetic bearings as force generators

The force generation principle has been explained in section 2.2.1 before.

In order to test the magnetic bearings, two experiments have been carried out: lifting and pull-off from the magnet.

Lifting test

In this test an increasing dc current was injected into the top bearing with the flywheel in lowest position, until the generated magnetic force suddenly lifts the rotor to the top position. The current was set by means of a controlled source with current limit applying voltage directly across the top bearing coil terminals, while measuring flywheel position.

Figure 3-24 shows the experimental data obtained from the experiment:
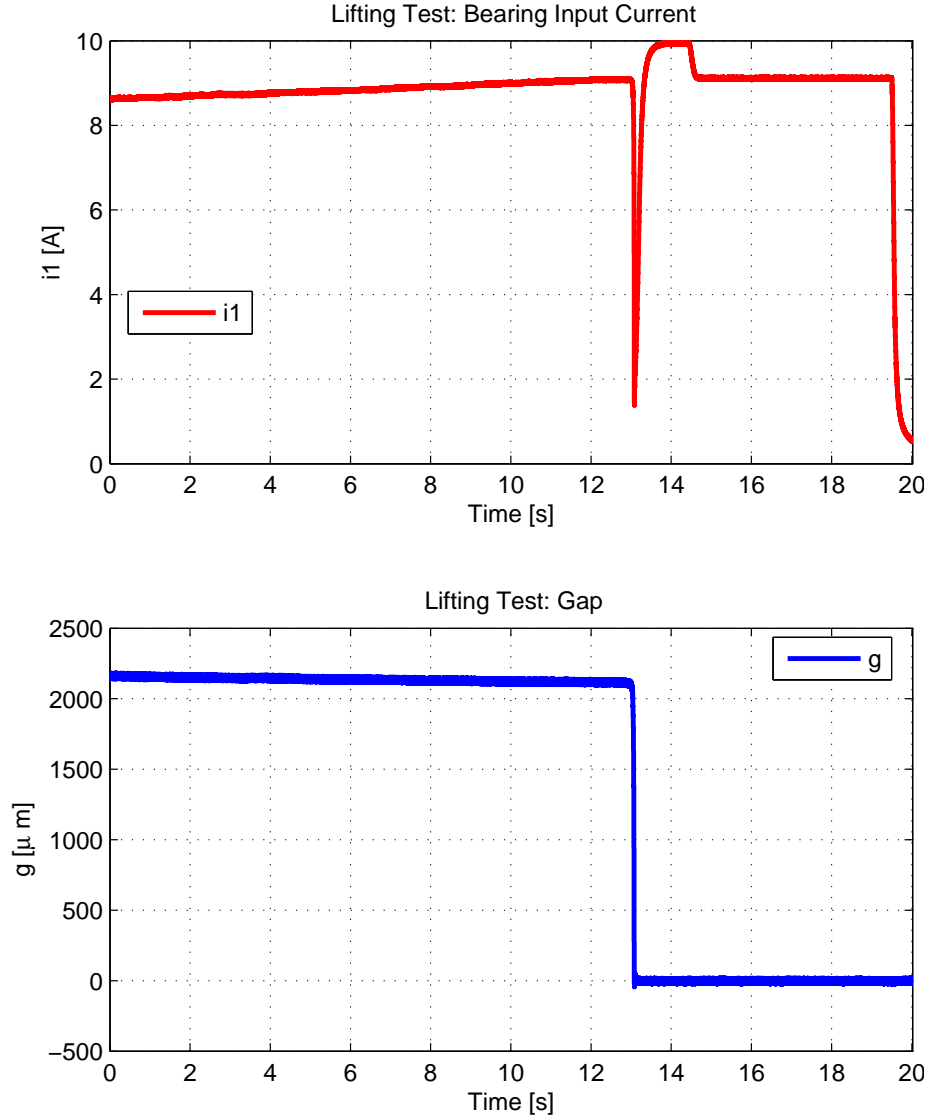
Figure 3-24: Lifting test: current through the bearing (blue) and position sensor voltage output (red) .

From the experiment carried out, the flywheel was lifted up when the current through the bearing was around 9 A. However, the theoretical force using equation 2.5 gives a magnetic force much higher than expected.

When the lifting occurs, the current is seen to decrease due to the back electromotive force produced by the movement of the flywheel.

Experimental data post-processing

Similarly to the characterization of the permanent magnet ring, an experimental validation of the model for the magnetic bearings has been carried out. The purpose of this data processing is to work out the total force that caused the lift of the flywheel. Once the total force is obtained, the force of the top magnetic bearing will be estimated experimentally.

Figure 3-25 shows the vertical displacement of the flywheel during the test in terms of gap between the top bearing and the flywheel.
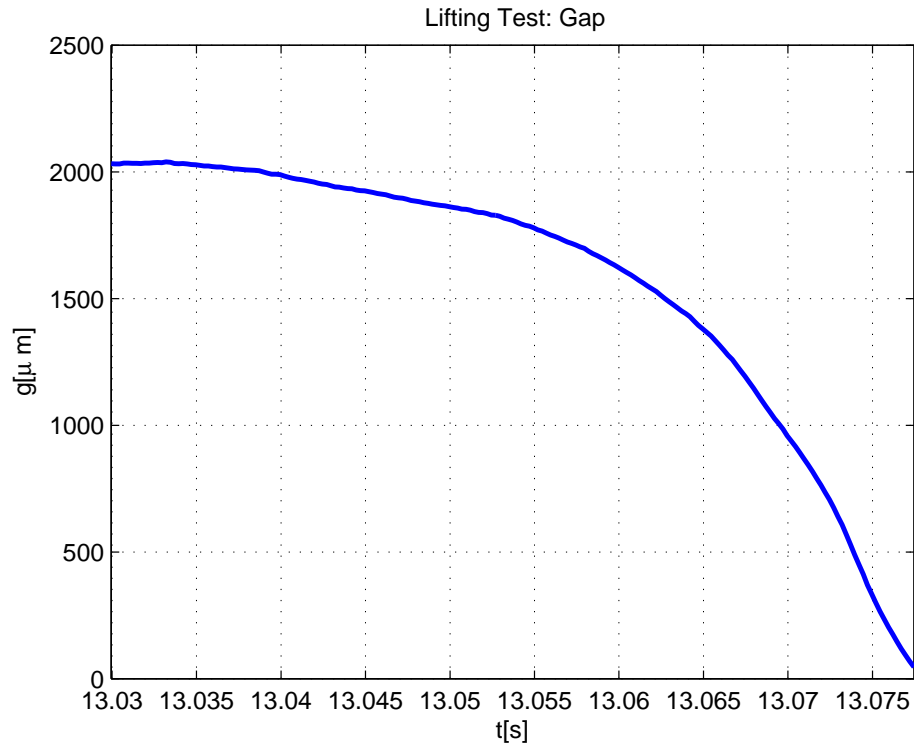
Figure 3-25: Lifting test: air gap.

From this signal the vertical velocity has been obtained after a derivative process in figure 3-26.
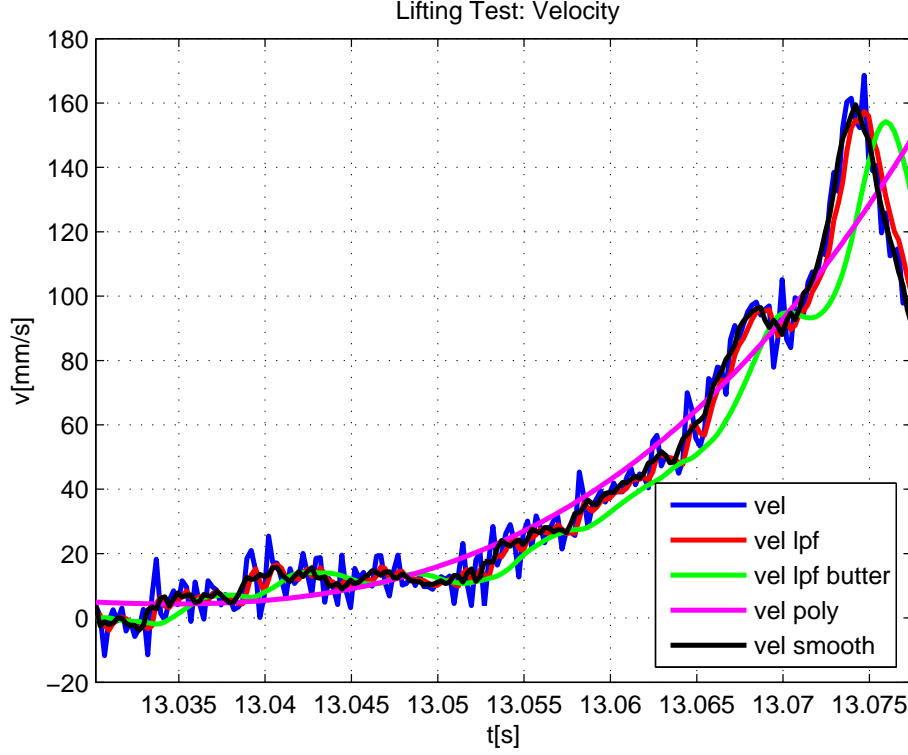
Figure 3-26: Lifting test: Velocity. Pure derivative from gap (blue), low-pass-filtered velocity (red), Butterworth low-pass-filtered velocity, velcocity polynomial approximation (magenta), velocity smoothed (black).

A second derivative has been performed over the velocity to get the total acceleration of the flywheel, shown in figure 3-27.

Scaling the acceleration by the flywheel mass, the total force that caused the movement can be obtained.

Let us call magnetic force as the sum of the magnet force and the bearing force. It can be calculated by subtracting the weight of the flywheel from the formerly calculated total force as:

$$F_{mag} = F_{total} - m \cdot g_a \tag{3.6}$$

Figure 3-29 shows the magnetic force against gap:
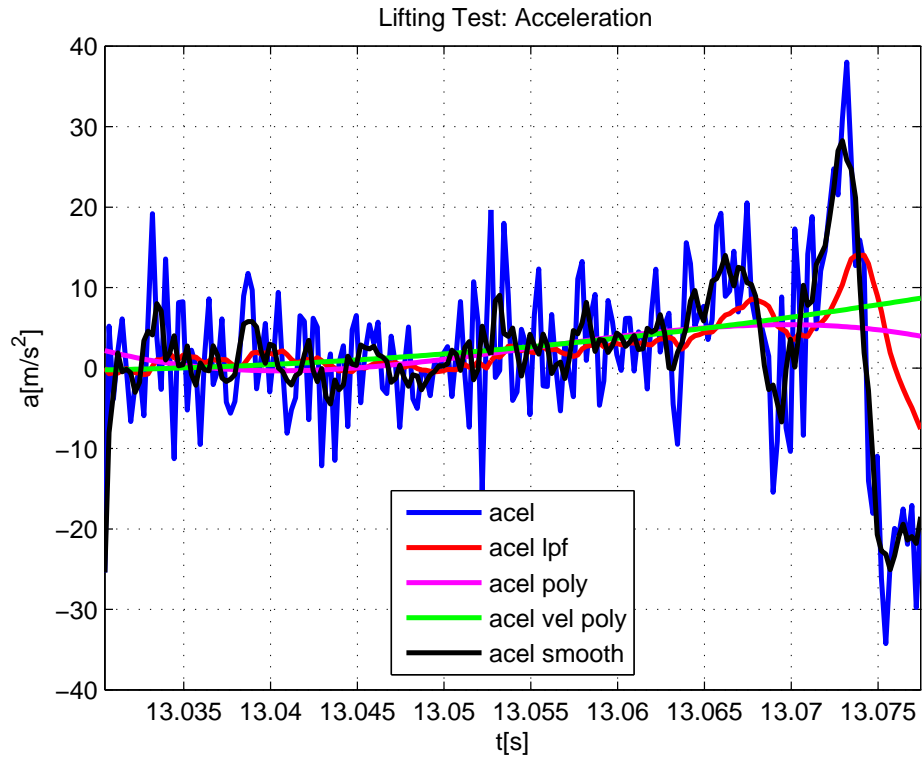
Figure 3-27: Lifting test: Acceleration. Pure derivative from velocity (blue), low-pass-filtered acceleration (red), acceleration polynomial approximation (magenta), acceleration from velocity polynomial approximation (green), smoothed acceleration (black).
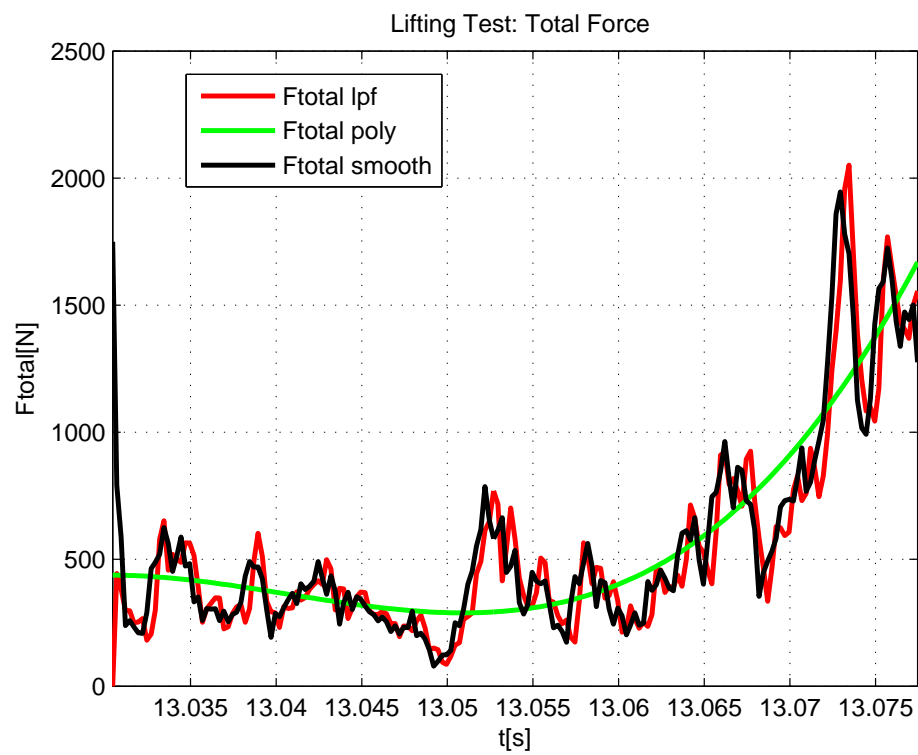
Figure 3-28: Lifting test: Total force. Low-pass-filtered total force (red), total force polynomial approximation (green), smoothed total force (black).
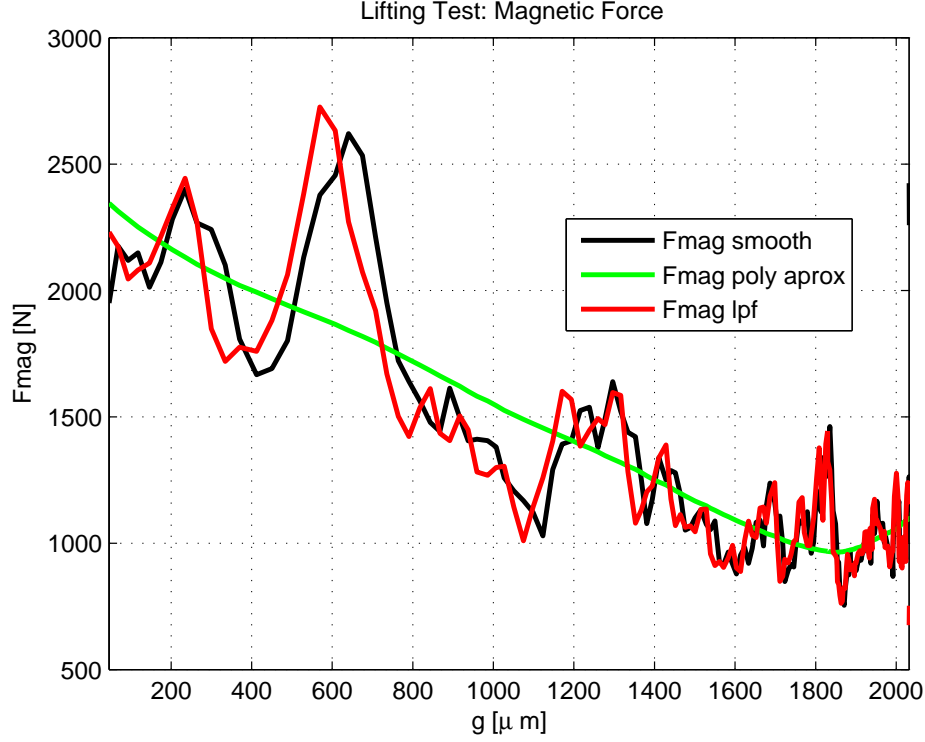
Figure 3-29: Lifting test: Magnetic force versus gap. Smoothed magnetic force (black), low-pass-filtered magnetic force (red), magnetic force polynomial approximation (green).

It has been seen that the formula of the force for the magnetic bearings (2.5) returns extraordinary high forces for the injected current and the gap in the test. As a result, the force produced by the top magnetic bearing during this test has been tried to be obtained through the energy approach.

$$E = \frac{1}{2} \cdot L \cdot i^2 \tag{3.7}$$

The above formula corresponds to the energy stored in the coil of the magnetic bearing for an specific inductance and current. The inductance variation along the lifting test has been obtained from the model mentioned previously ((3.2), see figure 3-9). The inductance variation for the lifting test is shown in figure 3-30.
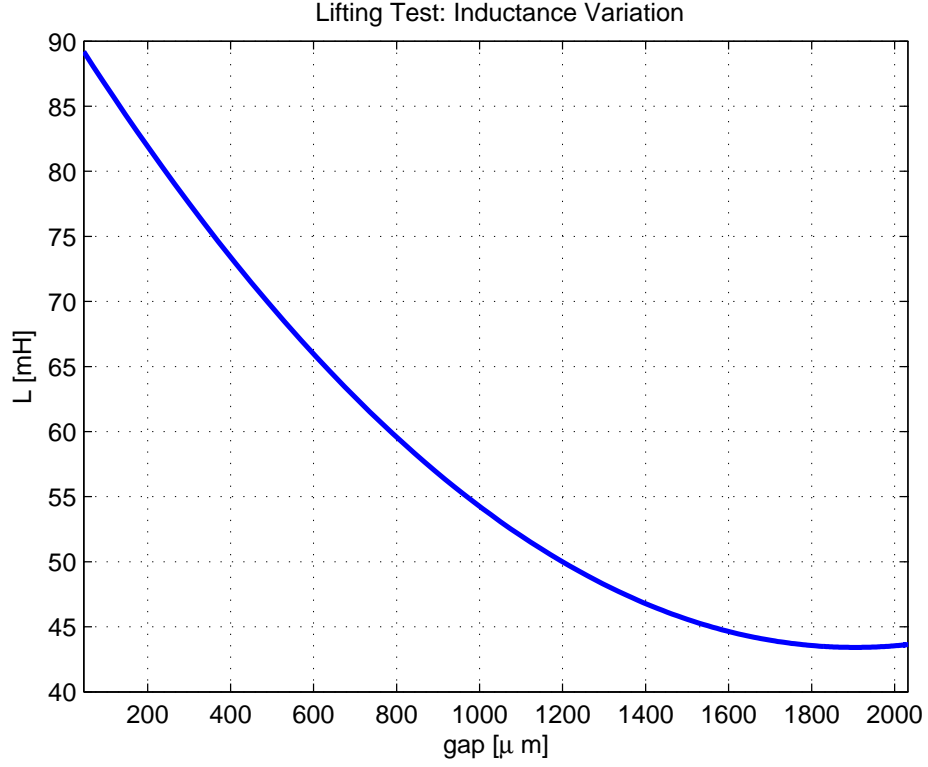
Figure 3-30: Lifting test: evolution of the inductance with the gap.

Thus, introducing the test data of current and inductance variation the energy during the lift has been obtained.

Therefore, the magnetic bearing force can be calculated as the variation of the energy with respect the gap, according to [6]:

$$F = \frac{\partial E}{\partial g} \tag{3.8}$$

Figure 3-31 shows a comparison of the bearing force using the energy approach and the theoretical formula (2.5).
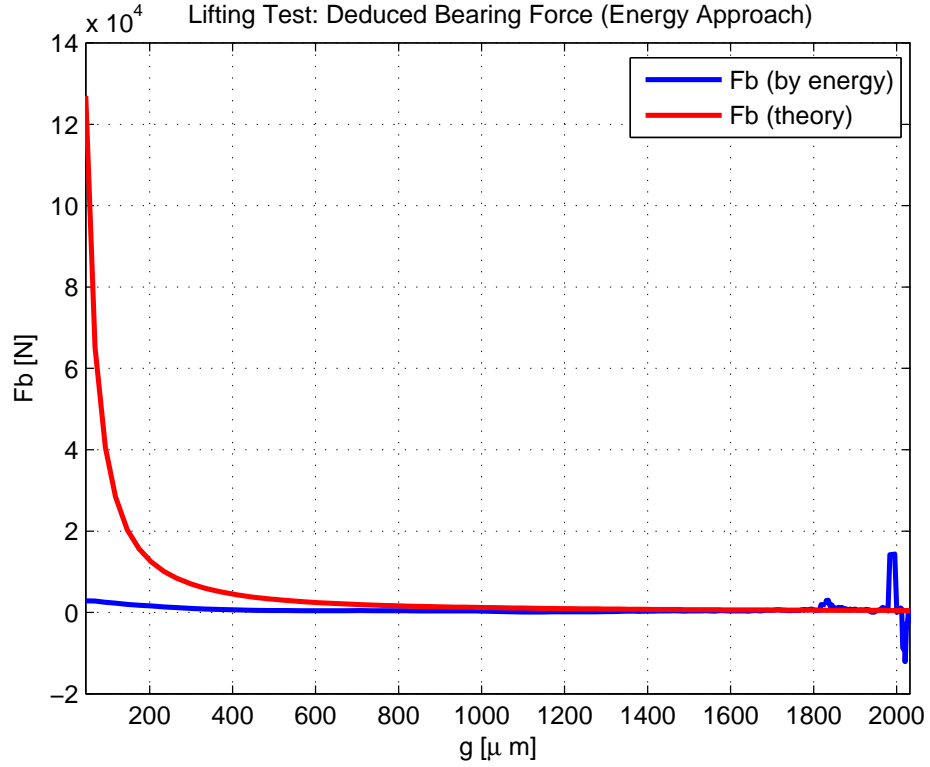
Figure 3-31: Lifting test: Bearing force using energy approach (blue), bearing force using the theoretical formula (red).

It can be appreciated from the figure the significant divergence of the results obtained using different approaches such as theoretical and through air gap energy.

Furthermore, the magnet ring force has been obtained assuming as true the bearing force obtained through energy approach. It has been compared to the magnet force obtained from the attraction test described previously. Both results are overlaid in figure 3-32.
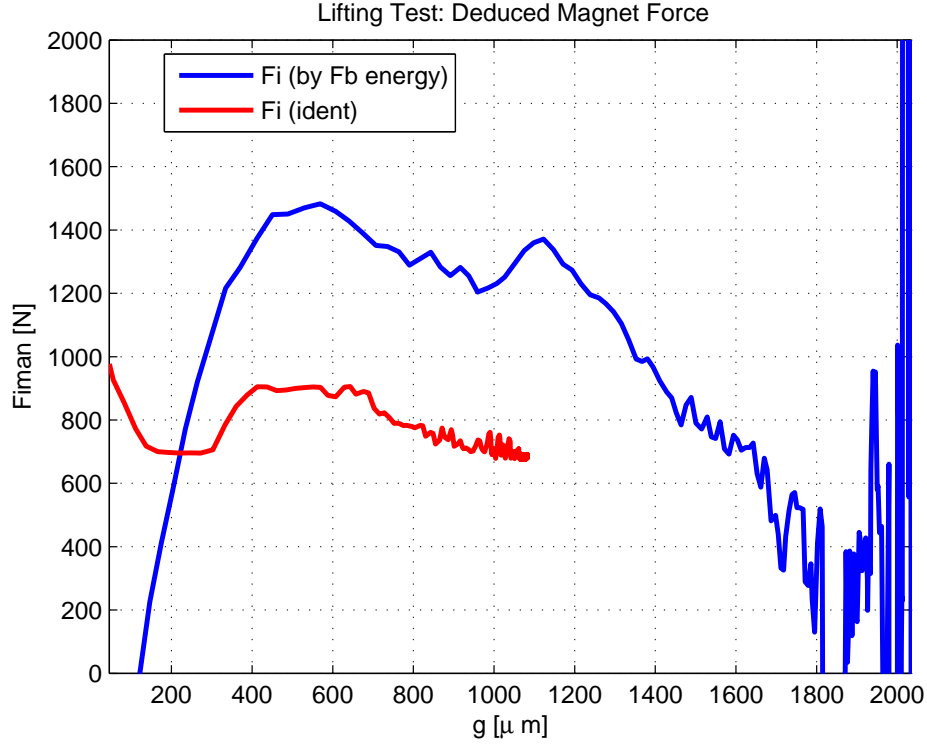
Figure 3-32: Lifting test: Overlaid plot of Magnet Force. Magnet force assuming bearing force by energy approach (blue) and magnet force by magnet attraction test (red).

The magnet force resulting from the attraction test (red) has been only obtained from g=1000 until the top position (g=0). This is due to the fact that the force of the magnet was not enough to cause a movement in the flywheel until a gap around 1000 μm.

As a conclusion, the force in the magnetic bearing is difficult to estimate, and the theoretical formula provided does not seem to give consistent results. The divergence from experimental results could be assigned not only to the leakage flux but also to the coupling between the magnetic fields generated by magnet ring and bearing. Also, the complexity of the geometry involved makes difficult to define a certain value for the area that the flux is passing through, leading to inaccurate results.

The problem should be tackled in the future by performing a Finite Element Analysis making use of the 3D model of the flywheel prototype provided.

Electromagnetic Model validation

Therefore, the magnetic force applied by the bearing strongly differs from the theoretical results. This is due to fact that the formula does not take into account leakage flux effects, and contains strong assumptions like perpendicular flux lines to the flux area, among other issues. Also, the complexity of the mechanical system with several gaps makes the theoretical approach for the system very tedious. Finite elements analysis based on the 3D model would be recommended, however it is out of the scope of this thesis.

As a result of the experimental observation, the theoretical formula for the magnetic force has been corrected by a factor of approximately 20% in order to match the simulation results with laboratory tests. This factor cannot be explained only by leakage flux so a more detailed analysis must be made to work out the magnetic bearing force.

Considering the correction factor, the model response is compared to the experimental results in Figure 3-24. The model was simulated using the experimental data of the current as an input for the upper bearing. The initial position of the model is the same as in the lifting test.

Figure 4-5 shows the position response of the flywheel for an increasing level of top bearing current until the lifting occurs.

As it can be appreciated from figure 4-5 the evolution of the position coming from the simulation model matches the experimental results.
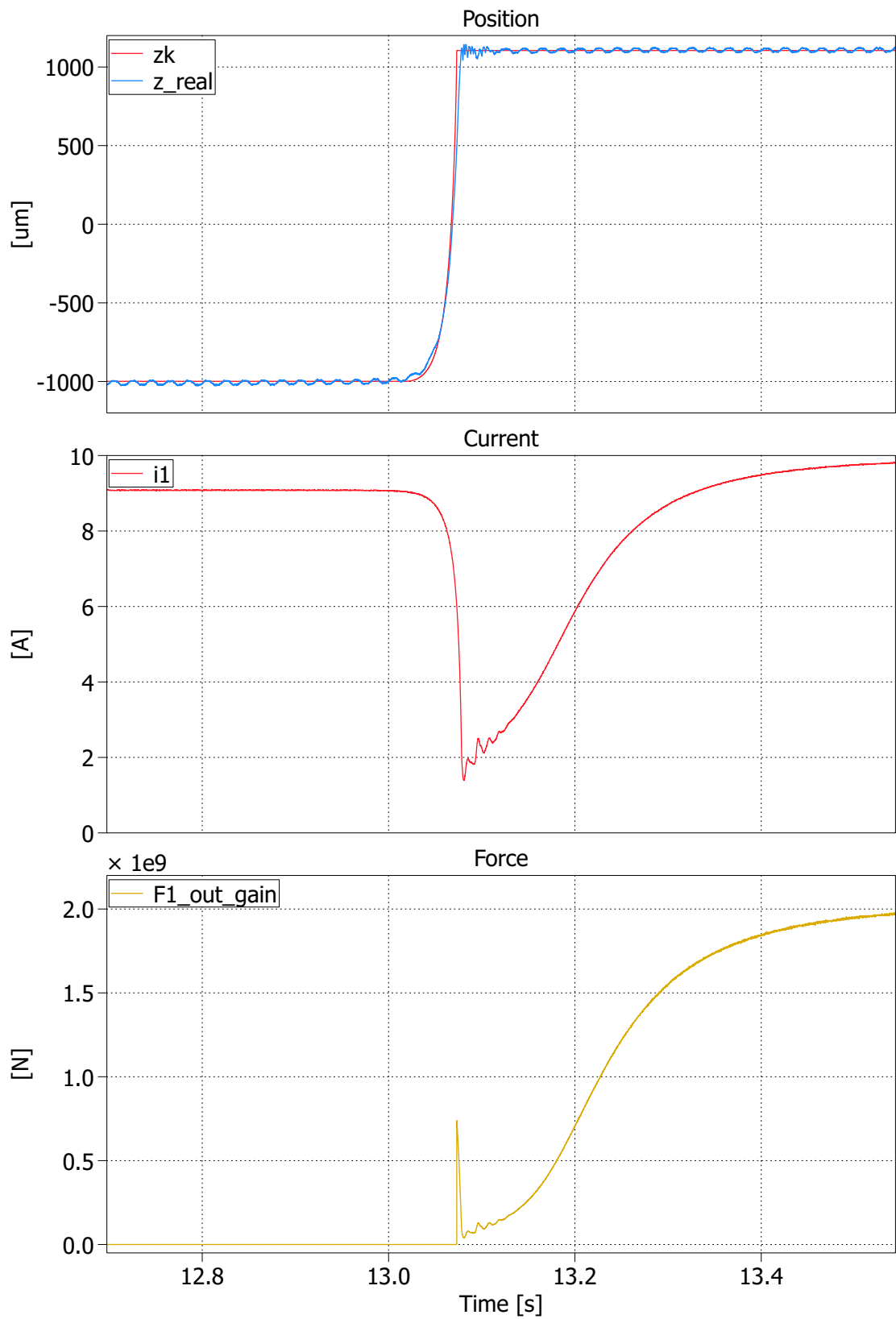
Figure 3-33: Overlaid plot of the lifting test in terms of position and top bearing current.

3.3 Chapter conclusions

In this chapter the identification process has been carried out for the flywheel prototype. The experimental identification of both electro-magnetic and mechanical model had to be done due to the uncertainties associated to the magnet ring as well as the inconsistencies seen from the theoretical formula of the magnetic force in the bearings.

As a result several tests have been performed followed by a data post-processing, in order to obtain a estimation of each of the parts experimentally. The estimations obtained have been compared to the experimental data through simulations, that helped to perform a fine adjustment of the model parameters.

Chapter 4

Power Converter and Hardware

In this chapter power converter topology and auxiliary hardware will be described, as well as the design criteria and features they provide.

Even though this thesis is focused on the axial magnetic bearings control, the hardware development for the radial bearings will be also provided for future work.

For the axial magnetic bearings a dedicated power converter was designed in early stage of the project, whereas for the radial magnetic bearings a commercial power stage will be used in the future.

4.1   Axial Magnetic Bearings

As described previously, the flywheel prototype contains two axial magnetic bearings at the top and lowest position. Each of this bearings is formed by a coil that will be driven by one of the outputs of the power converter.

4.1.1   Power Converter

As mentioned before, in order for the current to be controlled, a power converter is needed for each of the coils forming the axial magnetic bearings.

The power converter must ensure a flexible and precise control of the current through the bearings.

Design Requirements

The voltage rating of the converter depends upon the characteristics of the electrical system, namely inductance of the bearings, and the desired dynamics. The higher the bandwidth required the higher the voltage that needs to be applied to the coil terminals to cause the expected current variation.

For a bandwidth around several Hz for the inductance measured in the coils, the 50 V available in the voltage source are suitable for this application. However, the voltage rating of the IGBTs was chosen 600 V, in order to have enough margin in the case the DC bus voltage is increased.

The current rating also depends on the dynamics desired. The power converter must be able to provide the necessary peak current for the start up of the vertical levitation system. Being the flywheel at the lowest position, the initial force requires a peak current to make the flywheel reach the levitation point. The estimated starting current peak is around 10 A, and the current value in the levitation position is around 2A.

However the converter has been designed to be able to pull off the flywheel from the magnet once it is in the top position. From the experiments carried out, the maximum value of the current needed would be 25 A. Taking into account all these considerations, the current rating of the IGBTs used was chosen to be 30 A.

Power Converter board

Thereby, the designed converter topology is the single-phase H-bridge inverter, which allows to fully control the dynamics of the current by applying voltage in the positive and negative polarity.

The power stage includes two identical inverters to drive the two axial magnetic bearings. Each of the inverters is dedicated to control the current in each of the axial magnetic bearings independently, while sharing the DC bus.

In this case the DC bus will be shared and provided by a controlled voltage source with current limit, available in the laboratory.
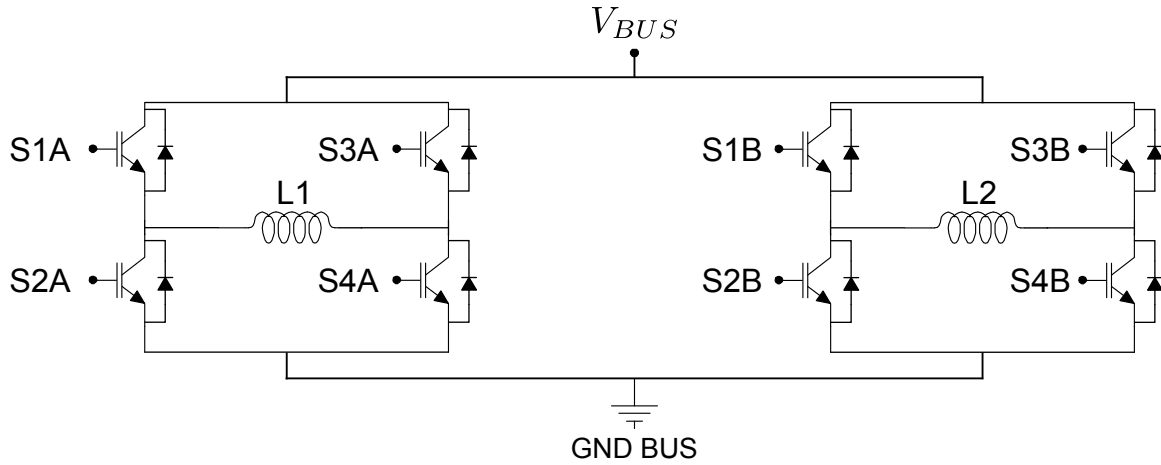
Figure 4-1: Power Converter Topology: two single-phase full-bridge inverters. Inverter A (top bearing), Inverter B (lowest bearing).
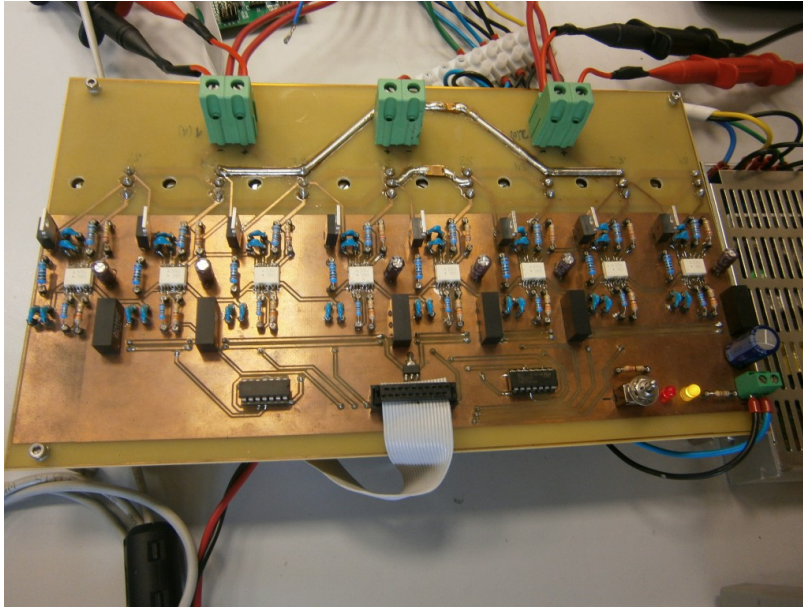
Figure 4-2: Power Converter prototype. Two single-phase full-bridge inverters.

The design of the power converter board was made trying to keep the symmetry as much as possible. The board receives the modulation signals through an 20 ways IDC connector, which are passed through a buffer to enable manual control over the modulation using a switch. The board includes driver circuitry, and IGBTs placed underneath, sharing a common heat sink. The two outputs are connected to the axial magnetic bearings with the measurement board in between.

Modulation Techniques

The power converter will be operated at a switching frequency of 10 kHz. The modulation strategy used is the well-known Pulse Width Modulation (PWM), which allows for a precise control of the voltage applied. Two different modulation strategies have been considered:

- **Bipolar:** the transistors are fired in X, that is in pairs: upper first leg with lower second leg and lower first leg with upper second leg. Thus, the power converter output is either $+V_{DC}$ or $-V_{DC}$. This modulation technique is very simple to implement but has high current ripple.

- **Unipolar:** the left leg is assigned the duty, and the right leg the complementary. Thus the converter output can achieve three levels: $+V_{DC}$, 0 or $-V_{DC}$. This modulation technique offers reduced current ripple allowing for a more precise current control.

4.1.2   DSP Board

The Digital Signal Processor (DSP) used is the TMS320 F28335 from Texas Instruments®. The DSP is used along with the docking station board, which provides the inputs and outputs physically available.
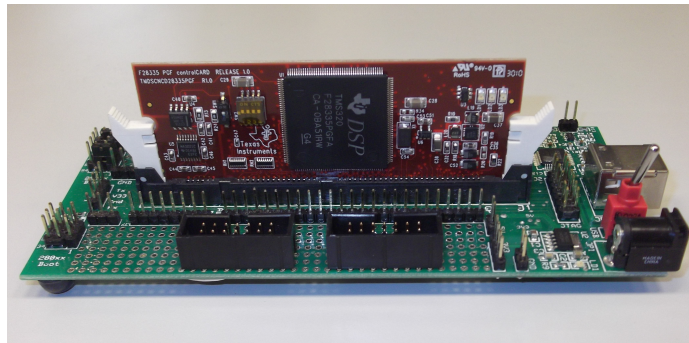
Figure 4-3: Overlaid plot of the lifting test in terms of position and top bearing current.

The DSP board will provide the modulation signals to the power converter as well as managing the measurement signals from the sensor boards.

Current and Voltage Measurement Board

The measurement PCB contains two current sensors and two voltage sensors for each of the outputs of the converter. The PCB also includes a signal conditioning stage for each of the measurements in order to provide the feedback signals in a suitable voltage range for the Analog/Digital Converter (ADC).
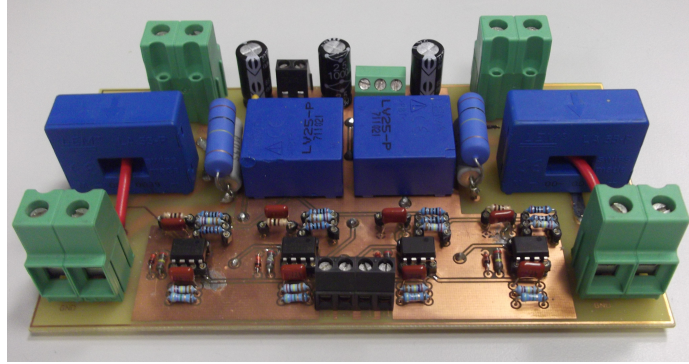
Figure 4-4: Overlaid plot of the lifting test in terms of position and top bearing current.

The signal conditioning stage converts the current signal from the sensors into voltage, to provide as a input for a 3.5 kHz anti-aliasing filter with scaling stage.

The measurement range for the current sensors depend on the measurement resistance at the input of the filtering stage, in this case is set to ±20 A.

Position Measurement Board

The position measurement provided by the sensor interface is within the range of 0-10 V. This PCB provides a signal conditioning to the ADC by scaling down the output voltage of the sensor by means of a voltage divider, and an optional low-pass filter.

4.2   Radial Magnetic Bearings

Each of the radial magnetic bearings is formed by three coils in a triangular disposition 120 degrees apart one from each other, allowing for a fully controllable force generation. Therefore, a three-phase inverter is needed for each of the two radial magnetic bearings.
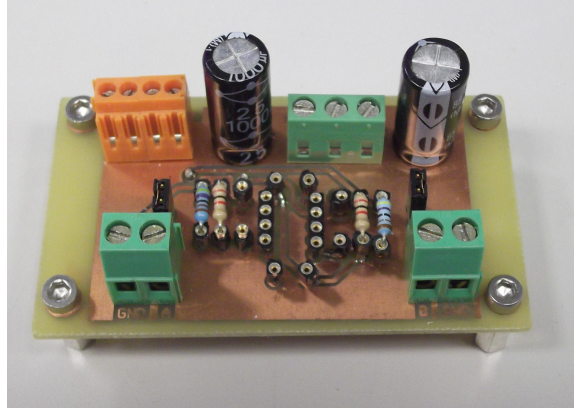
Figure 4-5: Overlaid plot of the lifting test in terms of position and top bearing current.

In this case the topology is the conventional three-phase inverter, and commercial power stages will be used for that purpose.

One of the goals of this project is to develop a set of PCB interfaces to be used with the commercial power stages available in the laboratory. Thus providing a ready-to-use hardware package to be used for the future control of the radial magnetic bearings, as well as for other applications.

4.2.1 Power Stage

The commercial power stages to be used are 10 kW three-phase inverters. The inverters contain a relay to connect to the grid inlet, driver circuitry and current and voltage sensors inside.

The power stage includes a pair of 25 ways D-sub connectors at the back side of the package.

The CONTROL connector manage the modulation signals for the IGBTs, the fault signals from the drivers, the reset signal and the grid relay control signal.

The SENSORS connector provides the measurement signals for phase currents, DC bus voltage and temperature.

The power stage has available the DC bus terminals, and offers the possibility to connect an external braking resistor with a braking leg transistor.
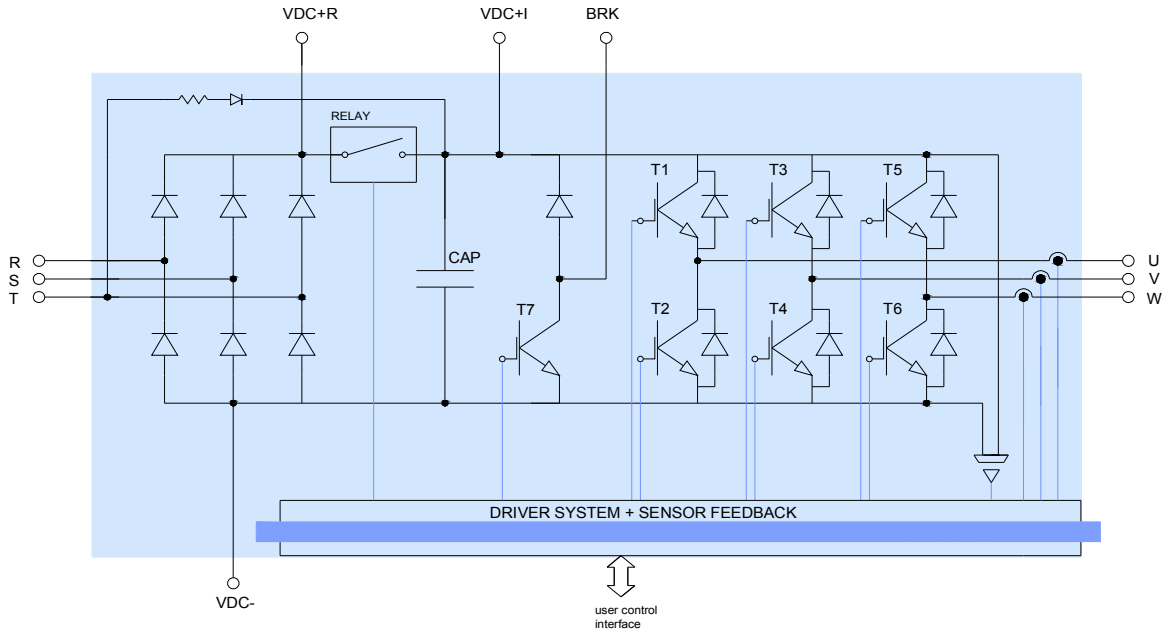
Figure 4-6: Schematic of the commercial power stage: 10 kW three-phase inverter.

4.2.2 DSP interface

The previously designed DSP interface includes connectors for the PWM module, ADC channels and other GPIOs. The DSP board is connected into the DSP interface rather than using the docking station board provided by the manufacturer. It has a portable programming board to load the code from the computer to the DSP via USB.

The DSP board is located in the right hand side of the interface, along with the GPIOs connectors. The supply connector and the portable programming board are located on top, and the PWM and ADC pins are available in the 8 ways connectors at the lowest part of the picture. The interface has a lever switch for the supply.

The DSP interface contains a signal conditioning stage for each of the ADC channels shown in figure 4-8. It consist of a 3.5 kHz anti-aliasing filter followed by a scaling stage. The input voltage range is [-1,1] V and the output is [3,0]V.
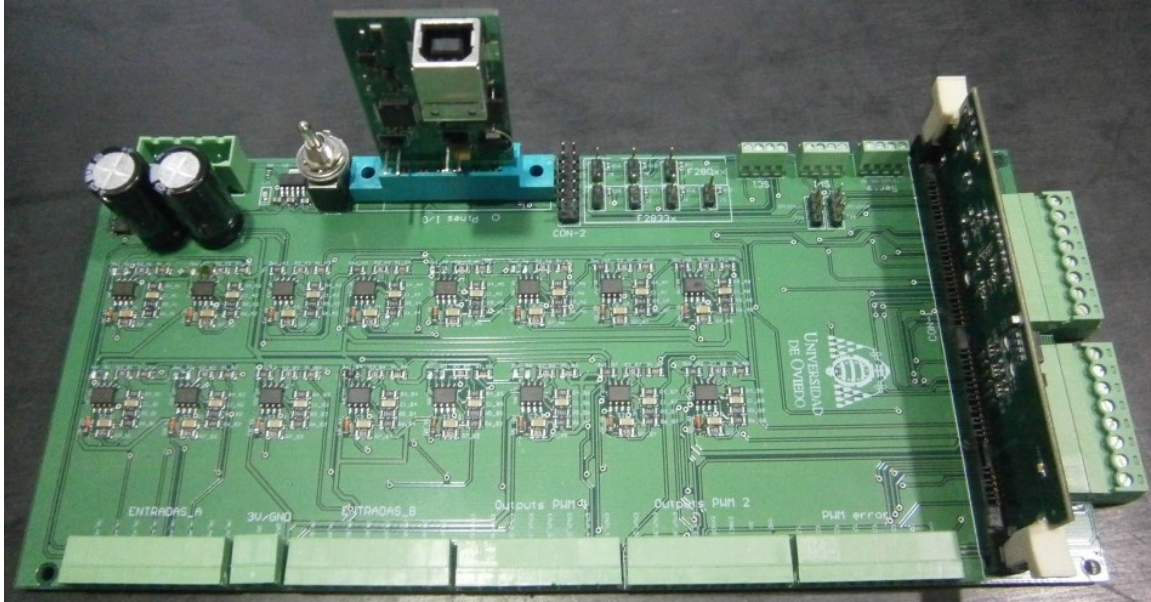
Figure 4-7: DSP interface.
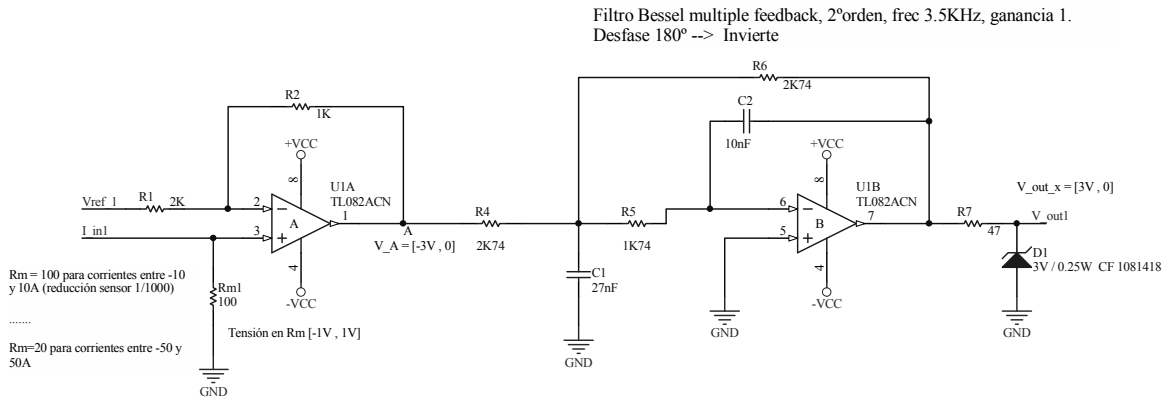
Figure 4-8: Signal conditioning stage included in the DSP interface for each of the ADC channels. 3.5 kHz anti-aliasing filter with scaling stage.

4.2.3 Control interface

In order to link the control signals with the power stage as well as provide feedback for the measurements to the DSP board, a PCB interface is needed.

The PCB interface must provide full control over the power stage, including manual enable of the modulation signals, monitoring LEDs and logic output signals.

The control PCB will be integrated along with the pre-designed DSP interface. Both PCBs will be stacked together in a back plane board, sharing tracks for the output connectors. Therefore, the design of the control interface has been aimed

to have full compatibility with the DSP interface provided, keeping the connection pin-out as well as the board shape.
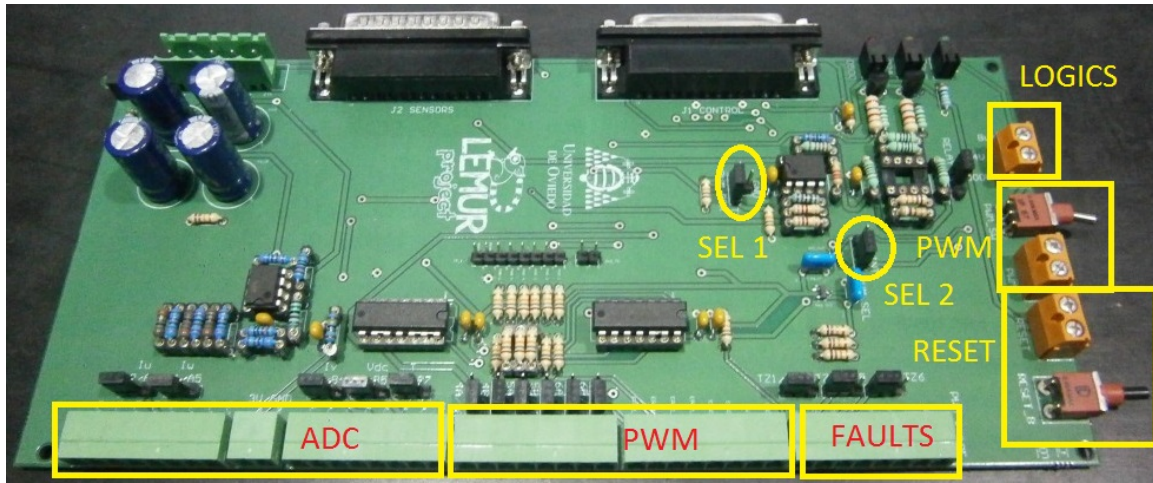
Figure 4-9: Control interface for the commercial power stage.

As in the DSP interface, the five control connectors at the bottom are identically located, as well as the supply connectors. All the pins in the control connectors are labeled onto the PCB for easy use. All the signals going to the output control connectors can be configured for two positions via jumper selectors. This is a flexible and fast way to configure the board depending on the channels used, and allowing to share the back plane for a back-to-back configuration.

PWM signals

The PWM connectors are located in the lowest right part of the PCB. The right most connector contains the driver fault output signals coming from the power stage, to be provided as an input to the DSP interface.

The two PWM connectors are located beside the faults connector on the left side. They receive the PWM modulation signals from the DSP interface and pass them through a pair of AND gates to provide control over the modulation. The PWM signals can be enabled internally with the lever switch or externally from the corresponding orange connector on the right side of the board. Both enable signals are passed through a single AND gate. Therefore, the enable signal provided to the

PWM enable connector must be in the range of 0-5V for logic 0 or 1 respectively.

A jumper selector (SEL 2 in the figure) allows to select the internal or external enable of the modulation. This selector avoids the need to bypass the PWM enable connector when the interface is driven externally.

In external mode both the lever switch and the enable input in the connector must be ON, whereas in internal mode only the switch position is taken into account. The green LED on the upper right is turned on when the switch is in the ON position.

Measurements

The ADC connectors in the lower left part of the PCB will provide the measurement signals from the power stage to the DSP interface. The voltage range for the phase current measurements is ± 7.5 V whereas for the Vdc is 0-7.5V. Therefore, a signal conditioning is placed in between to accomodate the voltage levels to the ADC. In the case of the Vdc measurement an analog circuit is needed to remove the offset, in order not to lose resolution in the digital conversion.

IMPORTANT NOTE: It is important to notice that the ADC connectors of the DSP interface were designed to provide the measurement directly from the sensors. For the use together with the Control interface the measurement resistor must be removed (see figure 4-8), only for those channels used.

Relay

As mentioned before, the power stage contains a relay to be managed to connect to the supply. This signal can be managed autonomously from the interface to manage the charge of the DC-bus or manually.

The autonomous charge makes use of a logic circuit to trigger the relay based on the Vdc measurement. When the supply voltage reaches 500 V, the relay is closed, and a red LED is turned on. This feature allows the interface to manage autonomously the charge of the DC bus.

However, the relay can be also managed manually by moving the jumper selector, either to close it manually or to leave it open, removing the jumper.

The yellow LED turns on as soon as the Vdc surpasses 24 V. When the yellow LED is turned off the DC bus is discharged indicating safety conditions.

Brake leg

The transistor in the brake leg can be used to burn energy in an external braking resistor when energy needs to be extracted from the application. This transistor can be triggered from a hysteresis analog circuit included in the board, which triggers the transistor when the DC-bus voltage exceeds an specific threshold. The upper and lower thresholds can be configurable by selecting the appropiate values of the resistors in the hysteresis comparator.

However, the braking transistor can be also used in modulation for other purposes such as boost converter, connecting in this case an external inductor across the brake terminals. This mode can be selected with SEL 1 in the figure just by placing the jumper selector in the corresponding position (PWM). The PWM input associated to the braking transistor is the PWM 4A.

4.2.4   Back plane board

In order to make a convenient and versatile hardware package, a back plane board has been designed. The back plane aims to stack both PCB interfaces ensuring compatibility. The PCBs are connected to the back place through the five 8-way control connectors on the bottom side of the interfaces, allowing the back plane to share the modulation and measurement signals.

The whole assembly can be seen in figure 4-10:

There are 3 and 4 rack designs available, depending on the application. The hardware developed is presented as a modular, ready-to-use package, which is very convenient for future use in a wide range of applications.
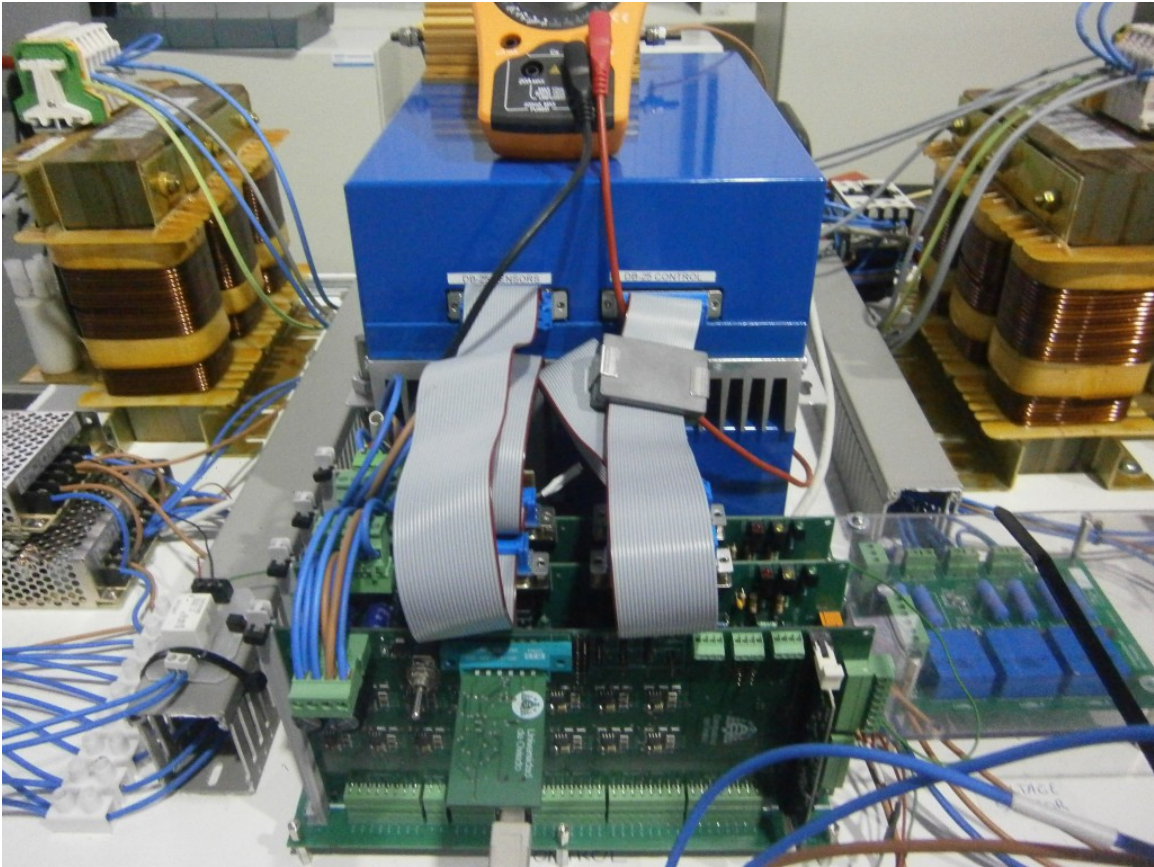
Figure 4-10: Stack assembly of the converter interface. DSP Interface and control interface mounted in the back plane.

Chapter 5

Control System

Once the system is properly identified, this chapter will describe how the problem of vertical magnetic levitation of the flywheel can be tackled from the point of view of the control system.

As mentioned before, the main goal of the control system is to maintain the flywheel in the levitation position, that is in the middle point of the gap between the flywheel and the magnetic bearings. In addition, the control system must provide a stiff response against disturbances in order to reject any kind of vibrations associated with the rotation of the flywheel, vibrations, or any other kind of external force trying to destabilize the flywheel.

5.1   Design Specifications

In order to withstand the flywheel in the levitation position, a variable force needs to be applied by the axial magnetic bearings. As mentioned previously, the force generated by the magnetic bearings depends on two variables: current through the coil and gap (see 2.2.1, eq. (2.5)). Therefore, to achieve an specific instantaneous force, the displacement signal must be taken into consideration to generate the current reference for the bearing, according to (2.6).

Therefore, the structure of the control system will be roughly an outer position controller that will produce a force reference according to the position error, and

an inner current loop for achieving the demanded force instantaneously taking into account the gap.

5.2   Current Control

The current is the main variable to control the force generation, and therefore the movement of the flywheel. To make the actual force of the bearing match the reference, an inner current loop will be used.

The current controller will be a conventional PI controller, in order to track the current reference without steady state error. The controller will be tuned accordingly to the parameters of the coils, namely inductance and resistance (see 3.2.1).

The selected tuning criteria is the pole-zero cancellation, which aims to cancel out the natural dynamic response of the coil to then shape it as desired. Considering this criterion, the current controller transfer function $C0$ will be of the form:

$$C0 = K_p \cdot \left(1 + \frac{1}{T_i \cdot s}\right) = K \frac{L \cdot s + R}{s} \tag{5.1}$$

where K_p is the proportional gain of the controller and T_i is the integral time constant. For a given bandwidth BW_i, these parameters can be calculated as:

$$K_p = 2 \cdot \pi \cdot BW_i L \tag{5.2}$$

$$T_i = L/R \tag{5.3}$$

In this case the bandwidth for the current controller has been set to 400 Hz.

5.2.1   Adaptive Controller

However, as it has been explained before (see 3.2.1), the inductance is not constant but varies with the flywheel displacement. The significant variation of the inductance represents a challenge for the conventional current controller shown before, since the

controller would not provide the dynamic reponse it has been designed for.

Therefore, an improved controller has been designed, able to re-calculate online its parameters according to the variation of the inductance with gap.

The controller is implemented in the digital domain using the Tustin discretization, for a sampling frequency of 10 kHz. The controller transfer function in discrete time will be the following:

$$C0z_{adap} = \frac{q_0 + q_1 \cdot z^{-1}}{1 + p_1 \cdot z^{-1}} \tag{5.4}$$

Since the current controller is PI, the coefficient p_1 equals -1. Once the inductance value is obtained for each sample period, the controller gains can be calculated according to (5.2) and (5.3). Then the controller coefficients will be calculated online as follows:

$$q_0 = K_p \cdot \frac{T_s}{2 \cdot T_i} + 1 \tag{5.5}$$

$$q_1 = K_p \cdot \frac{T_s}{2 \cdot T_i} - 1 \tag{5.6}$$

With the adaptive controller, the coefficients will be updated online each sample period T_s.

Figure 5-1 shows a comparative simulation response of the conventional current controller and the adaptive controller. A stepped reference has been introduced as a command for both controllers while varying the gap. As a result, the adaptive controller is seen to have better response than the traditional controller since the inductance variation is compensated online.
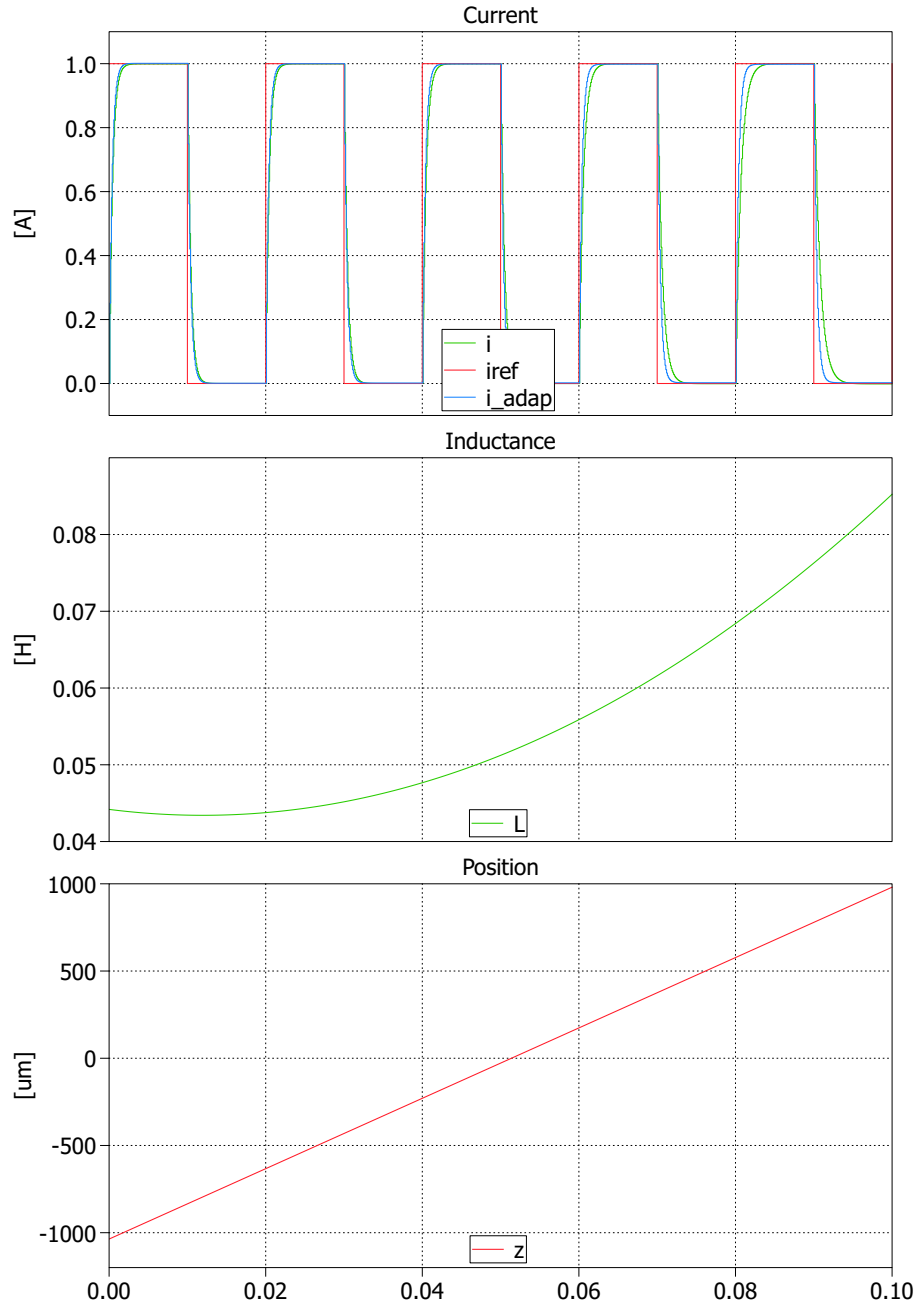
Figure 5-1: Overlaid simulated response of conventional and adaptive current controller. Current reference (red), fixed controller response (green), adaptive controller response (blue).

5.3 Position Control

The position control is the main objective of the whole control system. It is aimed to control the flywheel position to reach the levitation point. The position controller will calculate the force to be applied based on the error of the position measurement with respect to the levitation set point, in the middle point of the total gap.

Before going further, let us define the coordinate reference frame.

5.3.1 Coordinates description

In order to give a more insightful view the position control, a new reference frame has been defined relative to the levitation position. The relative reference frame facilitates the implementation as well as giving a more meaningful view of the position control. However the absolute reference frame is also used for the vertical displacement in experiments, since it has physical meaning for the formulas applied.

In order to clarify, figure 5-2 shows an schematic view of the coordinate variables involved.
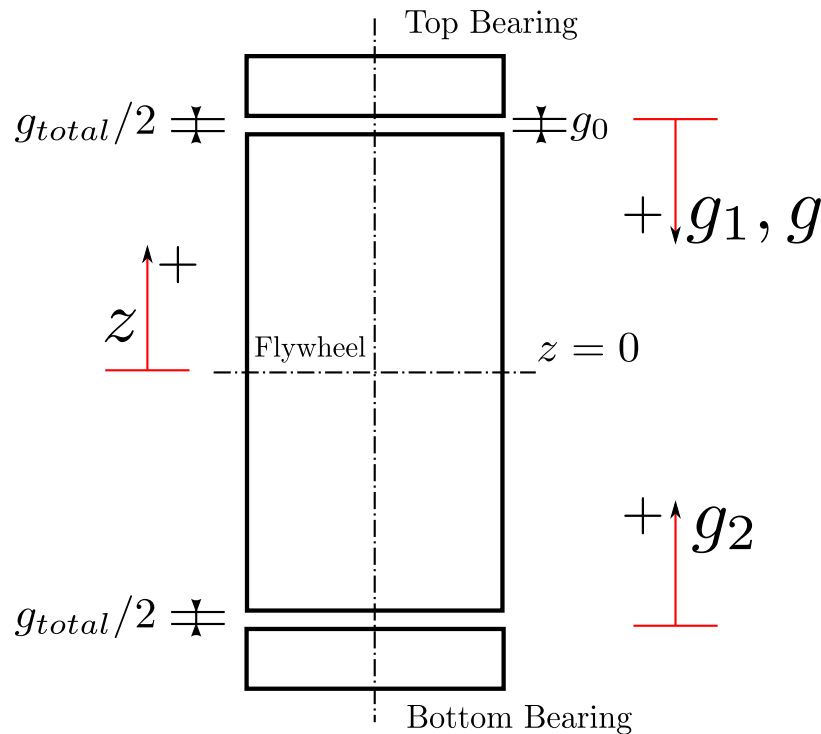
Figure 5-2: Coordinates description

The position variable z represents the vertical coordinate with respect the levitation set point, increasing towards the top bearing. Thus, $z = 0$ is the levitation position.

On the other hand, the variable g represents the gap between the bearing and the flywheel, by default associated to the top bearing. From now on, the subscript 1 will refer to the top bearing and 2 to the bottom bearing. Thus, g_1 is the gap between the top bearing and the flywheel, while g_2 is the gap for the bottom bearing. Obviously, both variables are complementary and they always add up to the total gap.

Position sensor

It is important to notice that the position sensor is measuring the vertical displacement of the flywheel with respect to the shaft. The position sensor is measuring the actual distance between a reference plate in the head of a screw attached to the tip of the flywheel shaft.

When the flywheel is in the top position, there is a small gap between the position sensor and the plate of around 900 μm.
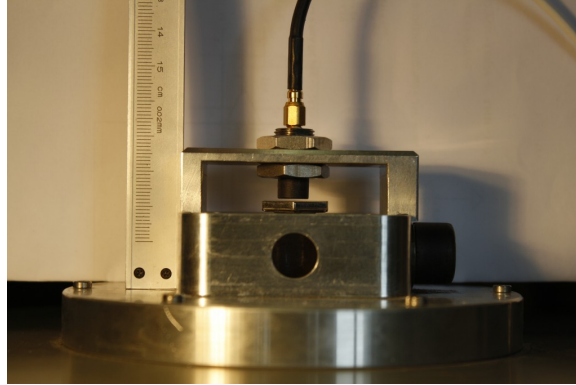
Figure 5-3: Position sensor measurement from screw plate attached to the flywheel shaft.

In order to get the actual gap between the flywheel and the bearings this small offset needs to be subtracted from the measurement.

Therefore, the total gap between the flywheel and the bearings is the difference between the maximum distance d_{max} (flywheel in lowest position) and the minimum

distance d_{min} (offset when the flywheel is in the top position):

$$g_{total} = d_{max} - d_{min} \qquad (5.7)$$

The total gap according to the mechanical 3D model provided is 3 mm long. However, using the position sensor the total gap is of around 2.2 mm. This inconsistency was first associated to the leakage flux of the hall effect position sensor, since the reference plate is small. However, using high-precision cameras the maximum distance from sensor tip to plate d_{max} was measured 2.9 mm and d_{min} 0.8 mm, giving a total gap of 2.1 mm.

In the levitation position, the nominal gap g_0 will then be:

$$g_0 = \frac{g_{total}}{2} \qquad (5.8)$$

The nominal gap will be used to easily move from relative coordinates to gap and vice versa:

$$g_1 = g_0 - z \qquad (5.9)$$

$$g_2 = g_0 + z \qquad (5.10)$$

Table 5.1 gathers the values of the gaps and vertical coordinates for the main position states of the flywheel:

	$\mathbf{z}$ $[\mu m]$	$\mathbf{g1}$ $[\mu m]$	$\mathbf{g2}$ $[\mu m]$
lower	$-g_0$ (-1106)	g_{total} (2212)	0
levitation	0	$g_{total}/2$ (1106)	$g_{total}/2$ (1106)
top	$+g_0$ (+1106)	0	g_{total} (2212)

Table 5.1: Relationship between levitation-referenced position variables ($\mathbf{z}$) and gap-referenced variables ($\mathbf{g1}$: top gap, $\mathbf{g2}$: lower gap).

5.3.2 Position Controller

Due to the unstable nature of the system, the main goal of the position controller is to stabilize the system. Thereby, the controller must provide a derivative term in order to make the system stable. Also, the position controller must provide a stiff disturbance rejection capability to ensure that the flywheel is kept in levitation in any case. Unlike the current control, which is aimed to have a good reference tracking, the position control loop must be optimized for disturbance rejection. This effect is achieved by increasing the integral gain of the controller.

PID controller

The intuitive approach is to design a PID controller (Proportional Integral Derivative) which fulfills both specifications. However, the fact that the controller provides derivative and integral effect in the control action increases the complexity of the tuning, as well as compromising the dynamic response, since the velocity is controlled indirectly. As a result, the design of the controller becomes a trade-off between both responses, leading to an overshoot in the reference tracking [12], resulting in an overshoot in the position.

Cascaded position-velocity controller

An improved dynamic response can be achieved by using a cascaded scheme for the position controller. The use of the vertical velocity as a feedback signal with a dedicated controller allows the dynamic response to be much more controllable while reducing the overshoot. By controlling the velocity directly, the derivative effect is moved to the feedback path, avoiding the influence of the reference command in the response.

The fact that the derivative effect is embedded in the velocity avoids the need of the perform the calculation inside the controller, therefore moving the derivative term to position feedback path. which allows the velocity to be independently controlled. This approach allows the controller to give an specific control action for the velocity,

instead of being coupled with the integral term. As a result, this control scheme offers a much better dynamic response compared to the PID controller, since now both control actions for position and velocity are independent.

Both control schemes are compared shown in figure 5-4 and 5-5:
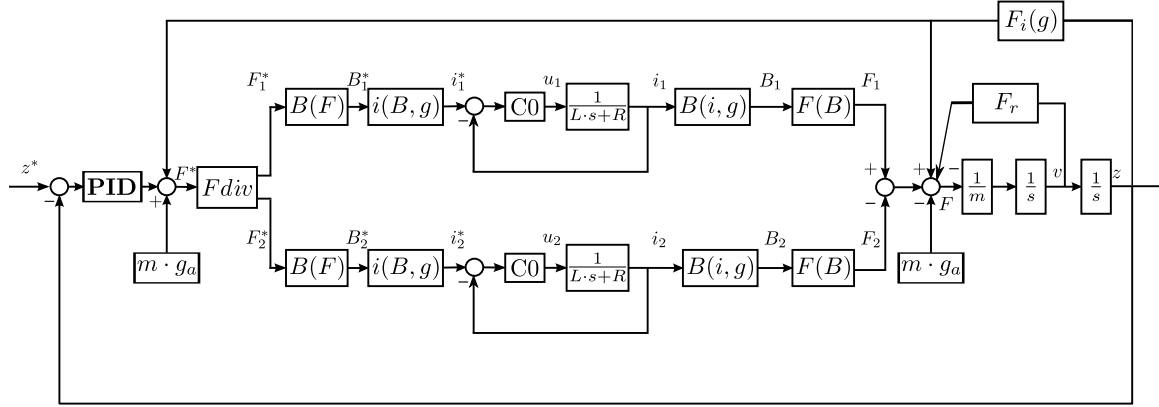
Figure 5-4: Control scheme using PID position controller.
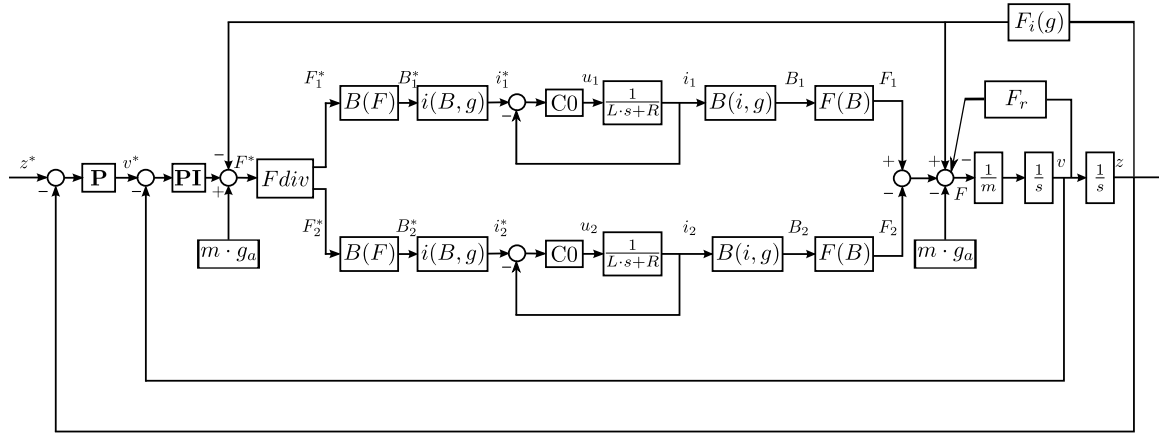
Figure 5-5: Control scheme using cascaded P-PI position-velocity controllers.

Figure 5-6 shows an overlaid plot of the simulated position control using both approaches [12]:
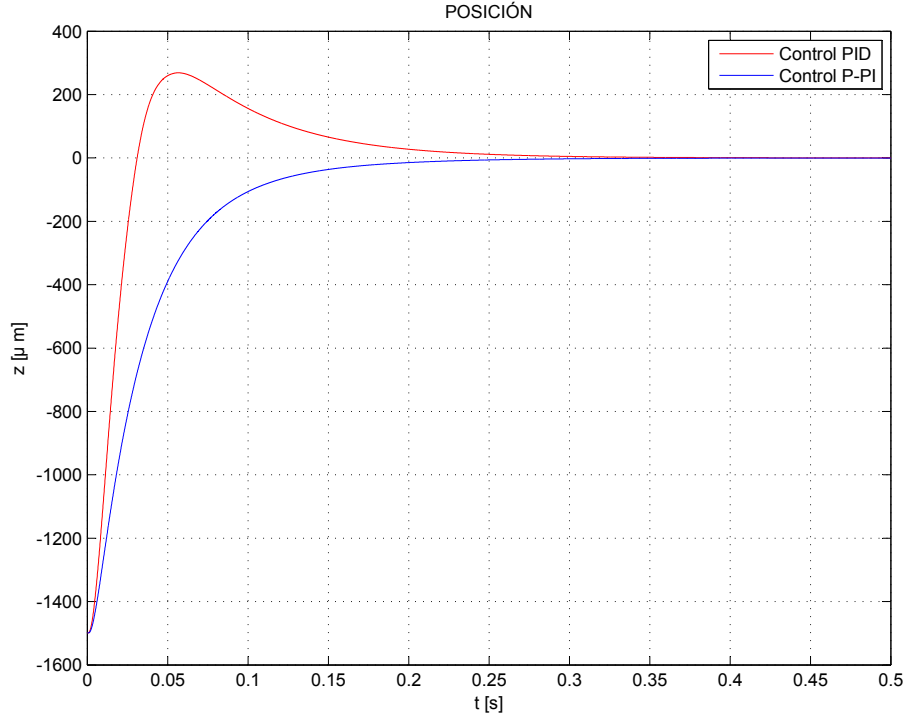
Figure 5-6: Overlaid simulation results for position control using different control schemes. PID position controller (red), cascaded position-velocity controllers (blue).

5.3.3 Velocity Estimation

Nevertheless, the velocity feedback signal is not present in the system, since there is no such vertical velocity sensor. Hence, the vertical velocity must be estimated from the position measurement of the flywheel. By doing so, the velocity feedback signal contains the derivative term necessary to make the system stable.

The fact that the position measurement includes noise when converted to digital domain, makes difficult to perform a derivative online, since the noise is amplified. Several digital filters are included in order to minimize the effect of noise, which will be described in next sections.

The tuning of the filtering stages has been carried out in simulation, first controlling the system with a virtual velocity feedback signal, coming from the mechanical model. The ideal velocity has been then faced with the estimated velocity signal in

order to tune the digital filters, trying to match the ideal velocity as much as possible.

The first estimation is carried out by the so-called velocity estimator, which is formed by a high-pass filter that behaves like a derivative for low frequencies, filtering out the higher frequencies. The cut-off frequency has been set to 40 Hz, which was seen to have the better estimation performance.

The estimation has been filtered out afterwards by using a low-pass filter set to 160 Hz. This filter will help to reduce the impact of feedback noise on the velocity estimation.

The frequency response of the velocity estimator and its components is shown in Figure 5-7:
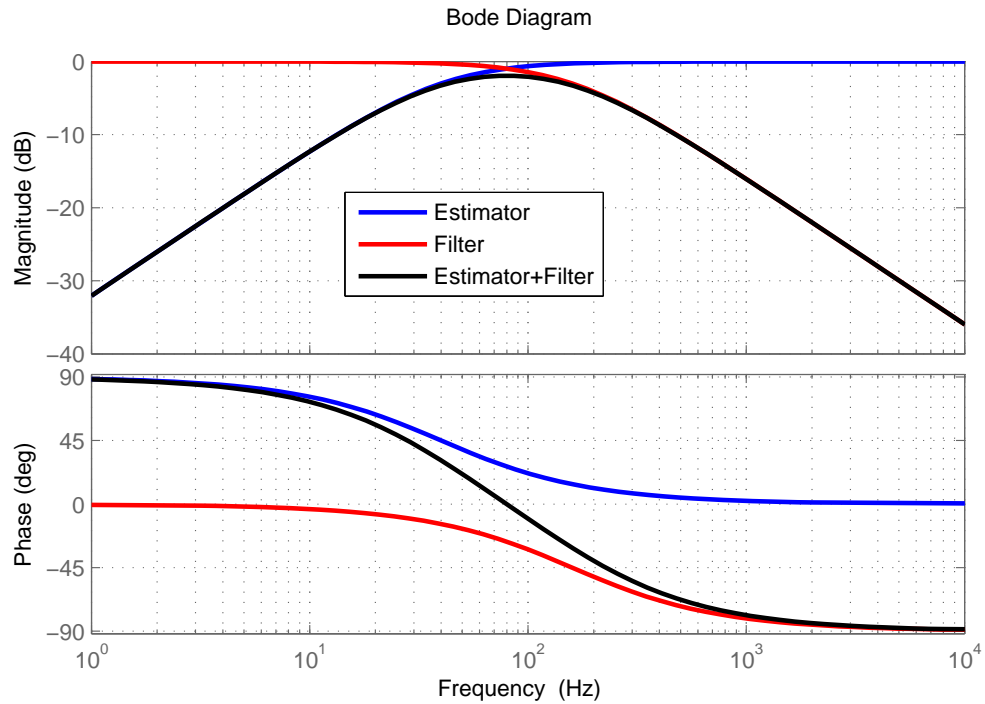
Figure 5-7: Simulation results for position control response including main control variables with noise in the position feedback.

Figure 5-8 shows the velocity estimation performance:
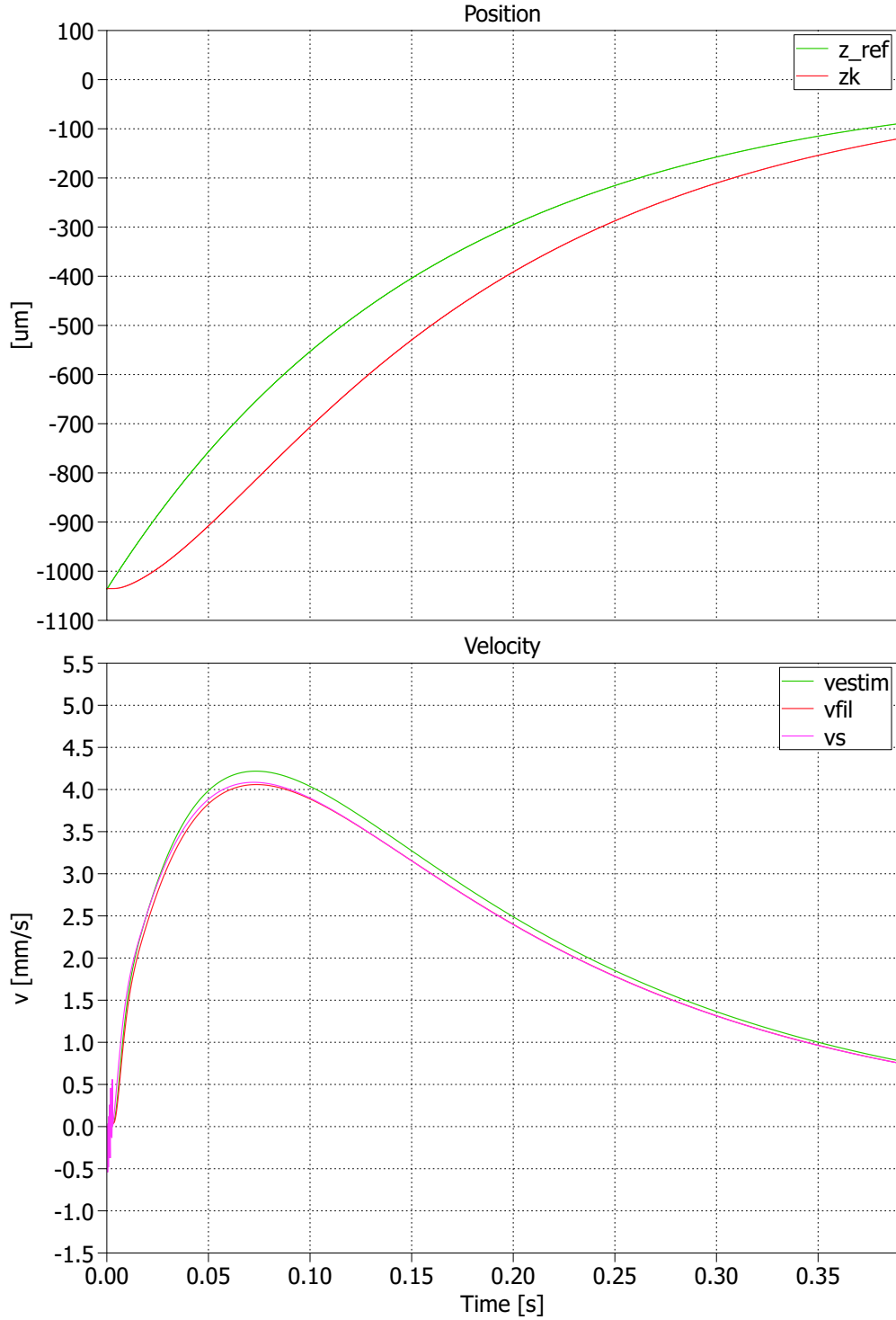
Figure 5-8: Simulation results for velocity estimation under position control. *vs* (magenta) is the velocity of the system coming from the integration of the acceleration, *vder* (green) is the velocity obtained directly form the velocity estimator (derivative + high-pass filter) and *vfil* (red) is the velocity using estimator and low-pass filter.

5.3.4 Force distribution

Since there are two thrust magnetic bearings, top and bottom, the required force must be distributed among those. Each bearing generates an attraction force, so the two bearings generate force in opposite directions.

Therefore, the addition of the two magnetic bearings' forces must add up to the required force to be applied to the mechanical system. Due to the inductive nature of the coils, the current cannot be stopped suddenly, so neither the force. Besides, the discontinuous conduction of the magnetic bearings can cause stability problems to the system.

To avoid these possible issues, a force offset has been applied in order to keep the magnetic bearings active at all time. This minimum force has been set to 10 N which represents a negligible value compared to the needed force for levitation.

The force distribution for a range of total force is shown in figure 5-9.
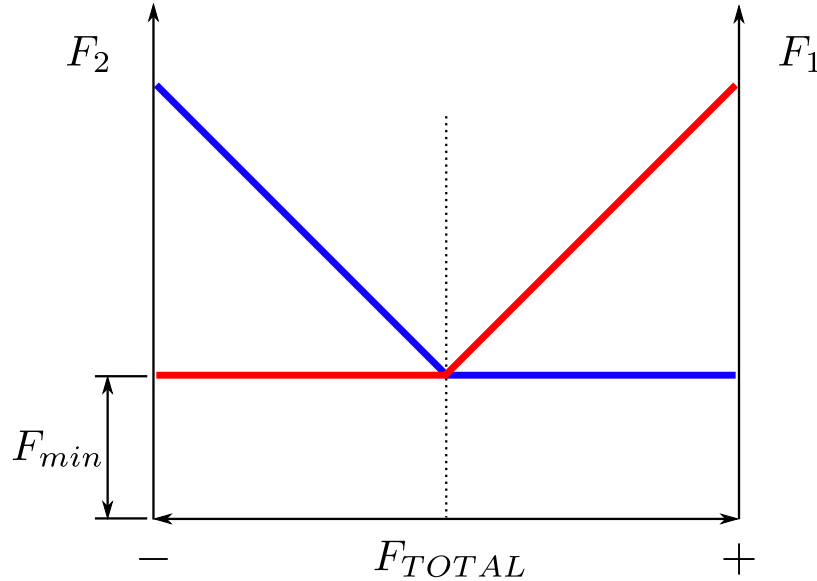
Figure 5-9: Force distribution among top and lowest bearings.

For positive reference forces the top bearing will operate while the lowest bearing remain with the minimum force. For negative reference forces the lowest bearing will act leaving the top bearing with the stand-by force.

The force reference generated by the position controller is split into two separated

references for each of the bearings, following the aforementioned relation. The force reference for each of the bearings can be calculated using the formula:

$$F_1 = F_{min} + \frac{|F_{TOTAL}| + F_{TOTAL}}{2} \tag{5.11}$$

$$F_2 = F_{min} + \frac{|F_{TOTAL}| - F_{TOTAL}}{2} \tag{5.12}$$

5.3.5 Controller tuning

Since the control scheme uses two cascaded controllers for position and velocity, it is necessary to consider the adequate transfer function for each one.

Velocity Controller

In the case of the velocity controller, the transfer function is:

$$G2 = \frac{vs}{Fs} = \frac{10^3}{m \cdot s} \tag{5.13}$$

This transfer function will give the vertical velocity in [mm/s] and the force in [N].

Now the task is to design a PI controller for to track the velocity reference without steady state error. The desired bandwidth must be significantly lower than the current controller. In this case around 40 Hz.

The dynamic response of the controller in closed loop is shown in figure 5.3.5.
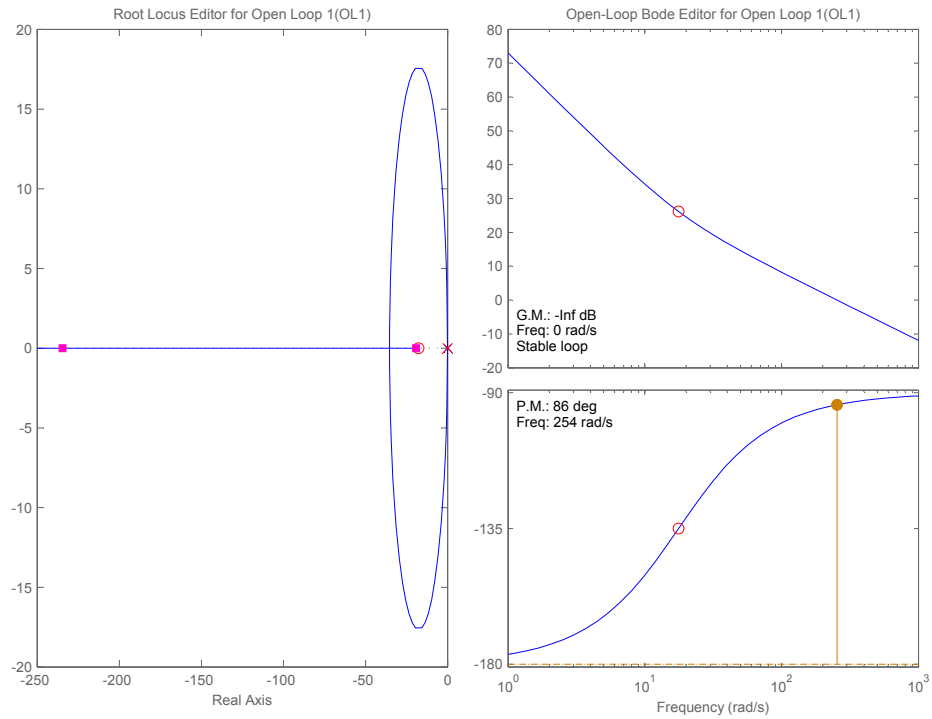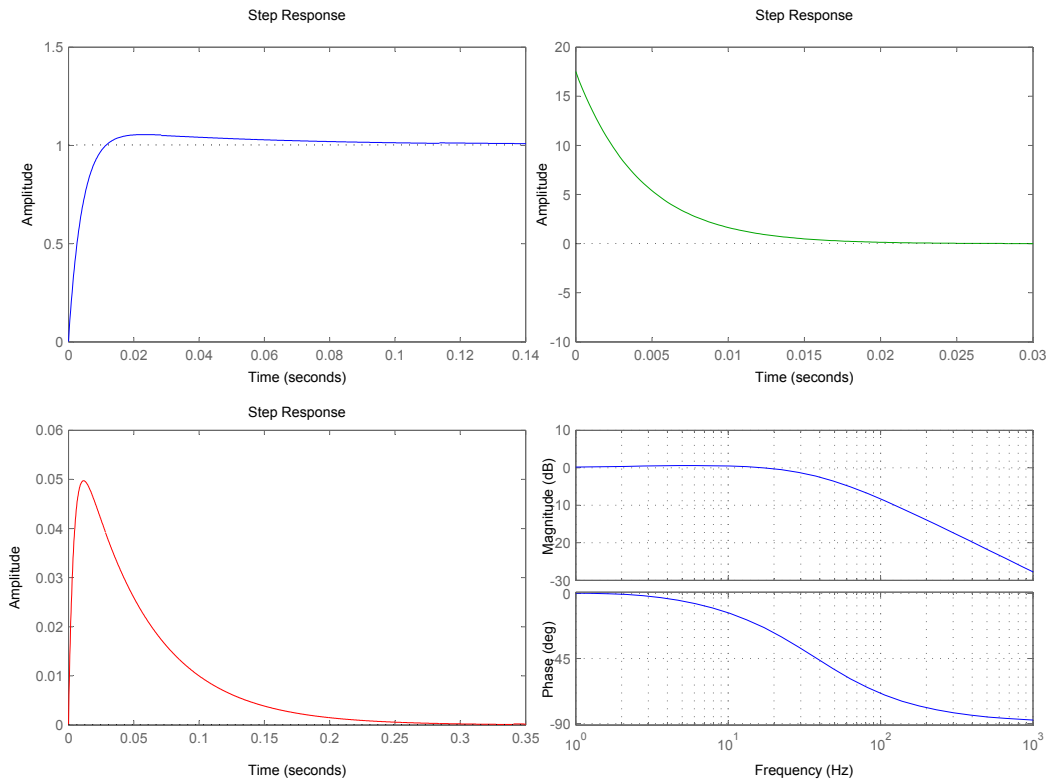
(a) Root locus (left) and open-loop Bode diagram (right)

(b) Reference tracking (top left), control action (top right), disturbance rejection (bottom left) and closed-loop Bode diagram (bottom right)

Figure 5-10: Velocity controller dynamic response.

A feedforward term is introduced to decouple the magnet force and the weight, since they do not represent a disturbance but a roughly known value. Thus, the velocity controller will only have to deal with the estimation error of these signals, rather than considering them a disturbance, with the subsequent improvement in the dynamic response. The decoupling takes place at the output of the velocity controller (see figure 5-5).

Position Controller

The transfer function for the position controller is:

$$G3 = \frac{z}{vs} = \frac{10^3}{s} \tag{5.14}$$

with the position in $[\mu\ \mathrm{m}]$ and the velocity in [mm/s].

The position controller will provide the velocity reference for the velocity controller, which is aimed to track it without steady state error. Therefore, the position controller will be a constant gain, in order to generate a velocity reference proportional to the position error. The bandwidth for this controller is around 4 Hz, since it is the outer most loop.

The dynamic response of the position controller is shown in figure 5.3.5.
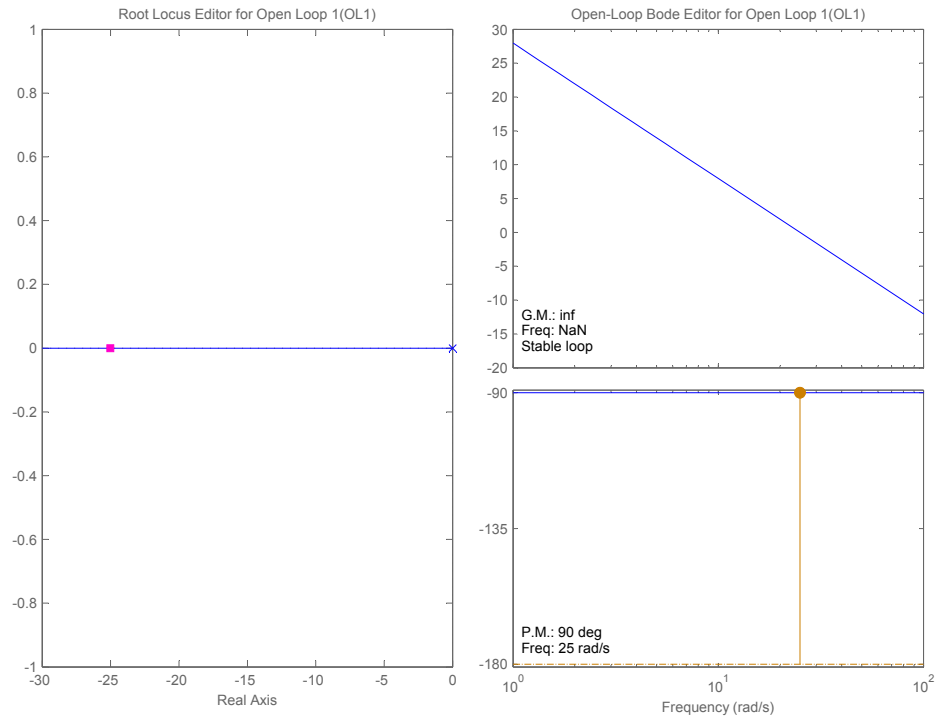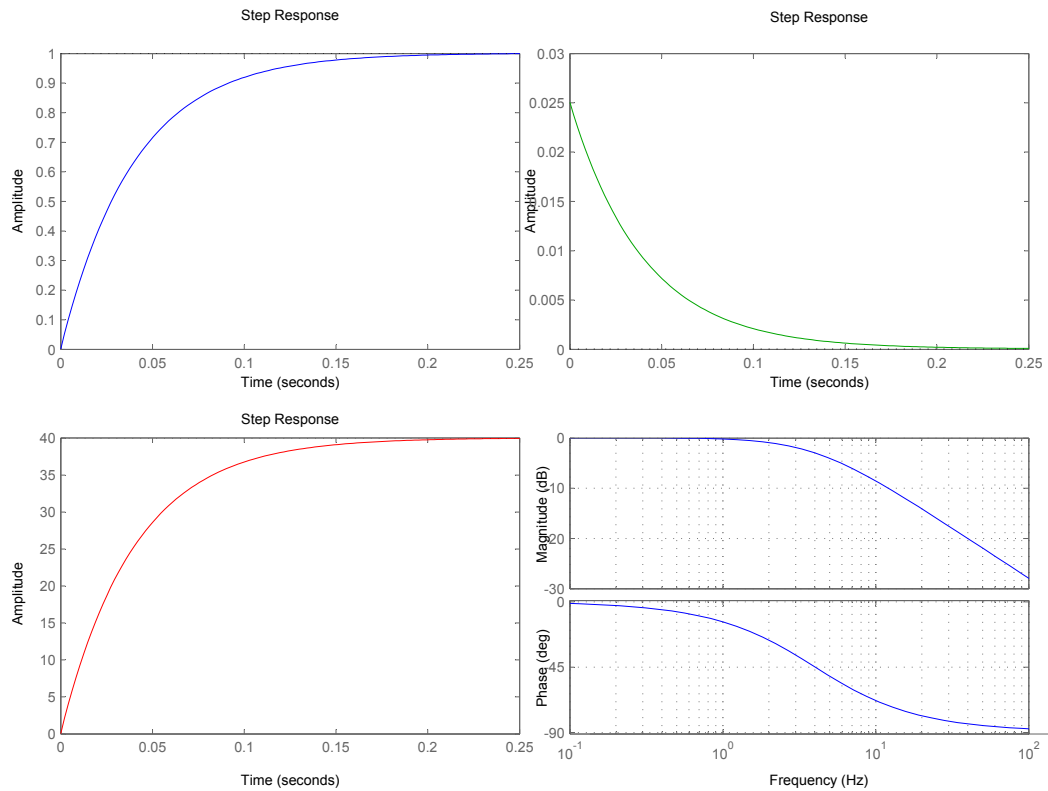
(a) Root locus (left) and open-loop Bode diagram (right).

(b) Reference tracking (top left), control action (top right), disturbance rejection (bottom left) and closed-loop Bode diagram (bottom right)

Figure 5-11: Position controller dynamic response.

5.4 Simulation Results

5.4.1 Simulation Model

The simulation model has been developed in MATLAB SIMULINK®, including the aforementioned regulators in discrete time. The model allows to load data from experiments to test the validate the model response, as well as a monitor where all the control variables can be displayed.

To model the mechanical boundaries of the system, the forces applied to the flywheel mass have been split into internal and external forces. By doing so, when the flywheel hits either the top or bottom boundary, the internal force, namely magnet ring force and weight, are disabled, simulating the force equilibrium condition. As for the external force, it is switch to zero depending on the direction and the flywheel position. Thus, the external force is set to zero either for positive forces with flywheel at the top, or negative forces with flywheel at the bottom. The reset signal for the internal force is also used to reset the velocity to zero.

5.4.2 Position control with velocity estimation

Using the velocity estimator proposed, the simulation results are shown in figure 5-12. As it can be seen from figure 5-12 the estimation is very accurate with respect to the actual velocity of the flywheel coming from the model.
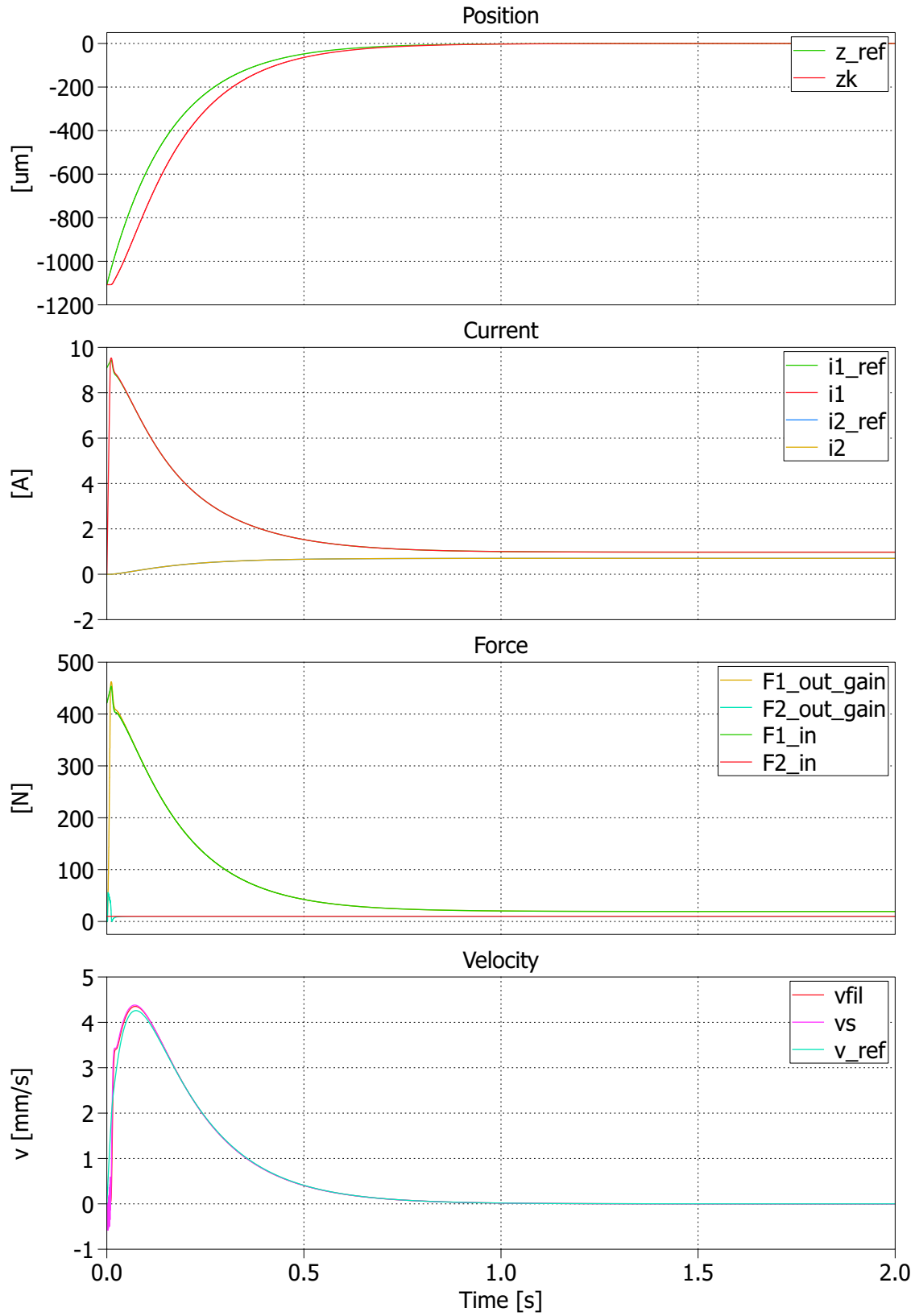
Figure 5-12: Position control simulation results using velocity estimator.

5.4.3 Analysis of Feedback Noise Impact

In order to test the robustness of the system, a random deviation in the position feedback path has been introduced. This effect aims to simulate the issue of the noise in the feedback path associated with the physical implementation of the control system.

In order to assess the level of noise, the position measurement has been stored in digital values from the ADC of the DSP.
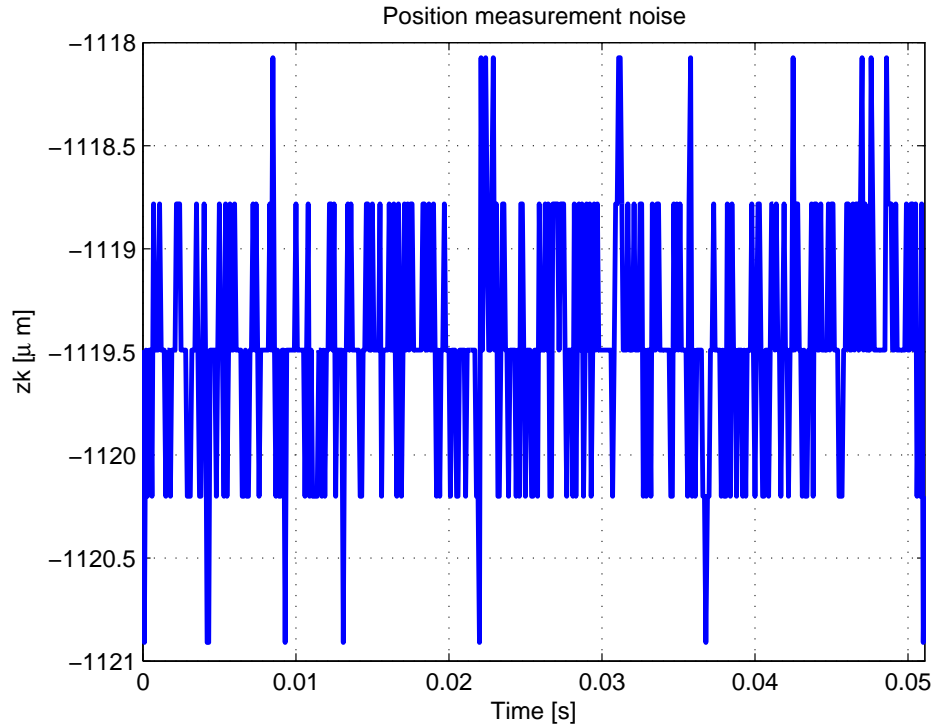
Figure 5-13: Experimental data record of the position feedback signal seen from the DSP. Impact of noise.

This record has been taken once the inverter is in operation, in order to consider the noise associated to the modulation. Thus, the noisy signal considered for simulation will be slightly higher than the worst case in normal operation, assuring reliable simulation results in terms of robustness.

Figure 5-14 shows the simulation results once the position noise is introduced in the feedback path.
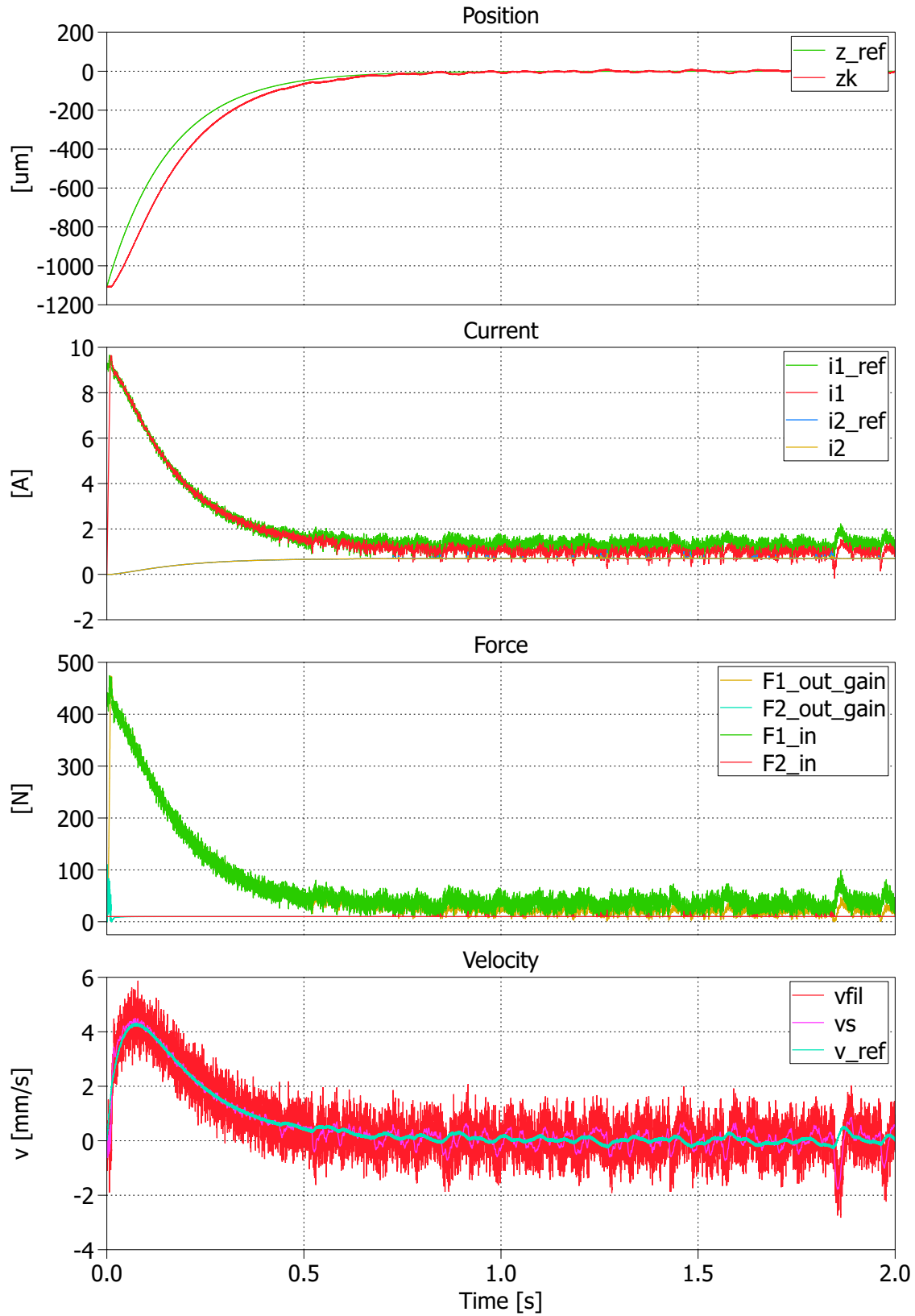
Figure 5-14: Position control simulation results using velocity estimator and noise in the position feedback path.

As a result of the noisy feedback signal, the filtering stage in the velocity estimator is not enough to minimize the impact of noise. As a result, an additional low-pass filter has been introduced in the feedback path to mitigate this impact.

Figure 5-15 shows the simulation results including position feedback filter.
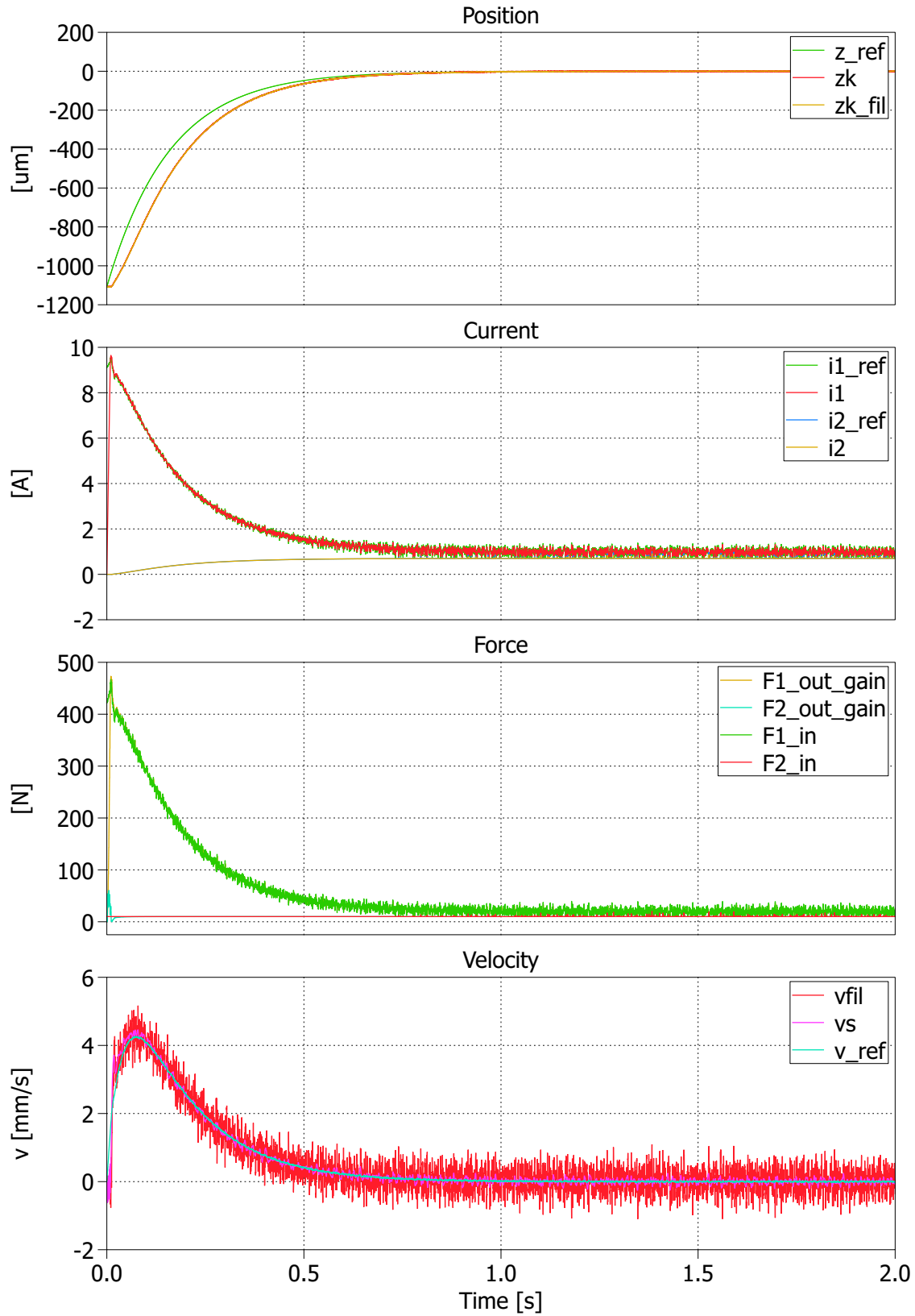
Figure 5-15: Position control simulation results using velocity estimator and position filter against noise in the feedback path.

Finally, the magnetic flux inside the flywheel has been checked for saturation in the material. Taking into account the signs of the currents through the coils and the magnet ring, the total magnetic flux intensity in the material can be calculated as:

$$B_{total} = B_1 + B_m - B_2 \tag{5.15}$$

During the initial current peak in the simulation 5-15 the total magnetic flux intensity has reached 1.3 T. This value seems to be lower than the saturation level for the magnetic material which is around 2 T. However, this is just an initial guess and a more accurate saturation test should be made once the materials are properly defined.

Chapter 6

Experimental Results

6.1 Experimental Setup

Figure 6-1 shows a photo of the experimental setup. The power converter and the measurement boards are connected to the axial magnetic bearings terminals of the flywheel prototype.
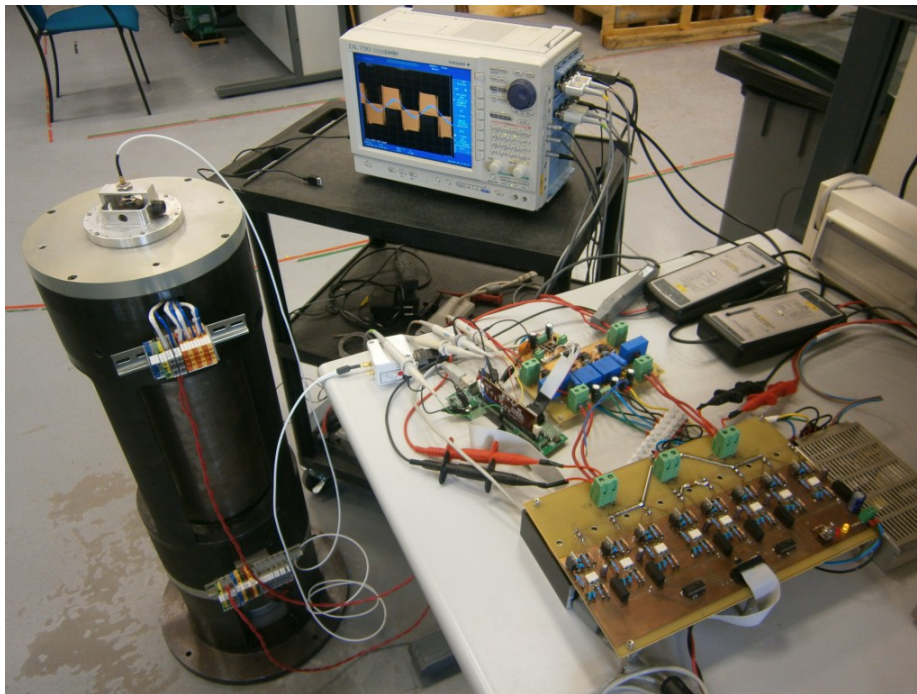
Figure 6-1: Experimental Setup.

6.2 Current Control

6.2.1 PWM Modulation comparison

In order to check the different PWM modulation techniques, a 50 Hz sinusoidal current reference has been set. The results are shown in Figure 6-2.
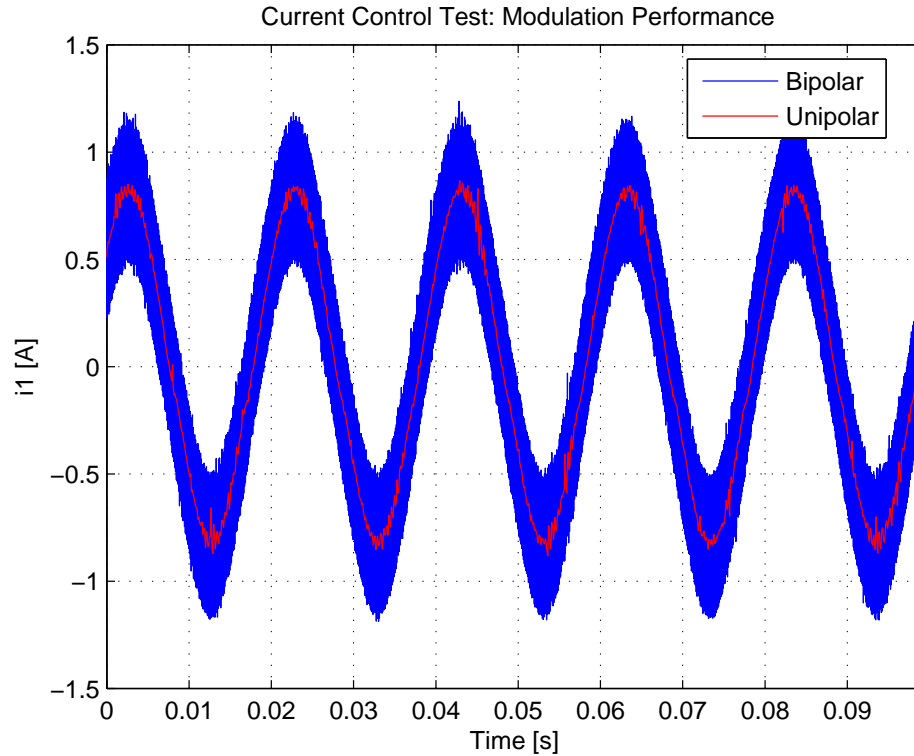
Figure 6-2: Current Control Performance: sinusoidal reference.

As it can be appreciated from above, the unipolar modulation allows for a much more reduced current ripple. This is crucial for the magnetic bearings since current ripple means force ripple, which could eventually become the system unstable due to the vibrations associated.

Figure 6-3 shows the performance of both modulation techniques under fix current control:
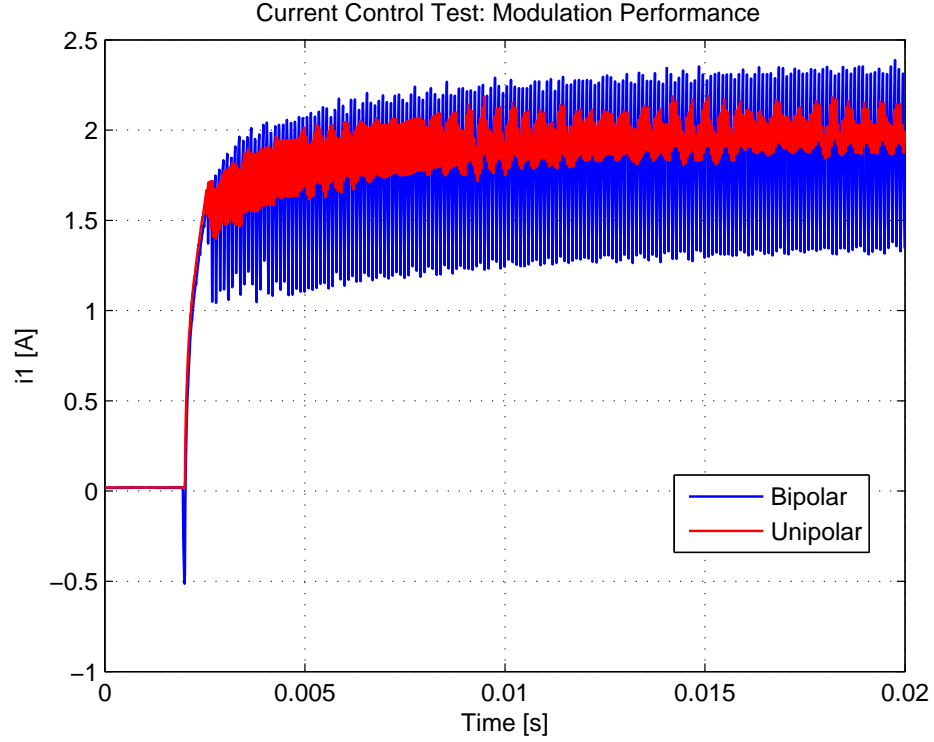
Figure 6-3: Current Control Test: overlaid plot of modulation performance. Bipolar modulation (blue), Unipolar modulation (red).

6.2.2 Current Control test: sinusoidal reference

Figure 6-4 shows the experimental results for 1A peak 50 Hz sinusoidal current reference using unipolar modulation:
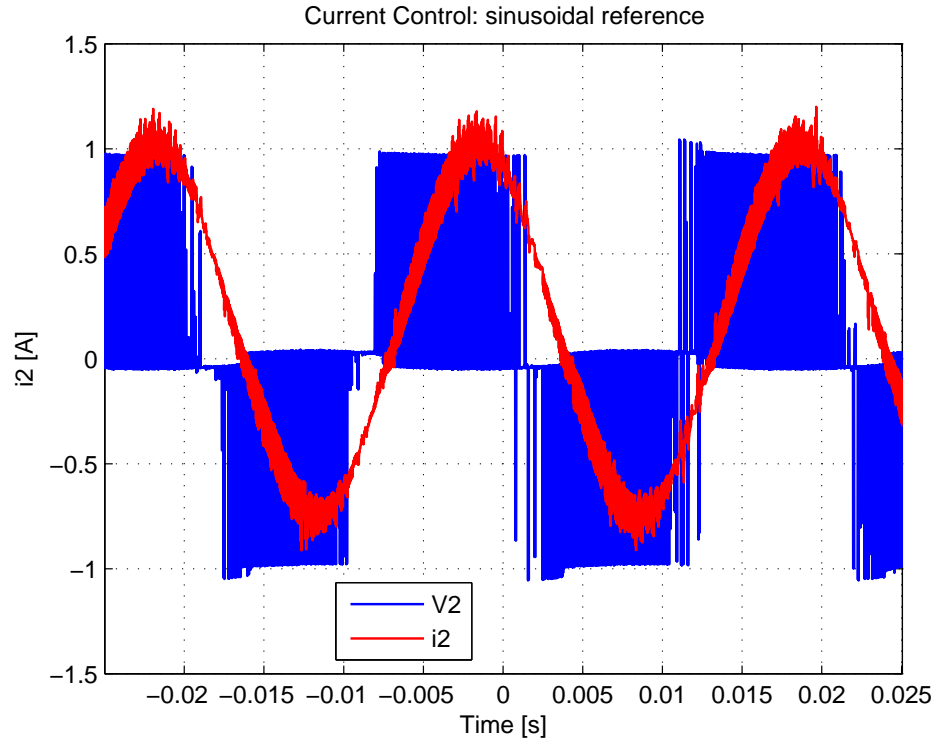
Figure 6-4: Current Control Performance: sinusoidal reference using unipolar modulation.

6.2.3 Current Control Test: variable stepped reference

Figure 6-5 shows the experimental results for a 2A stepped current reference:
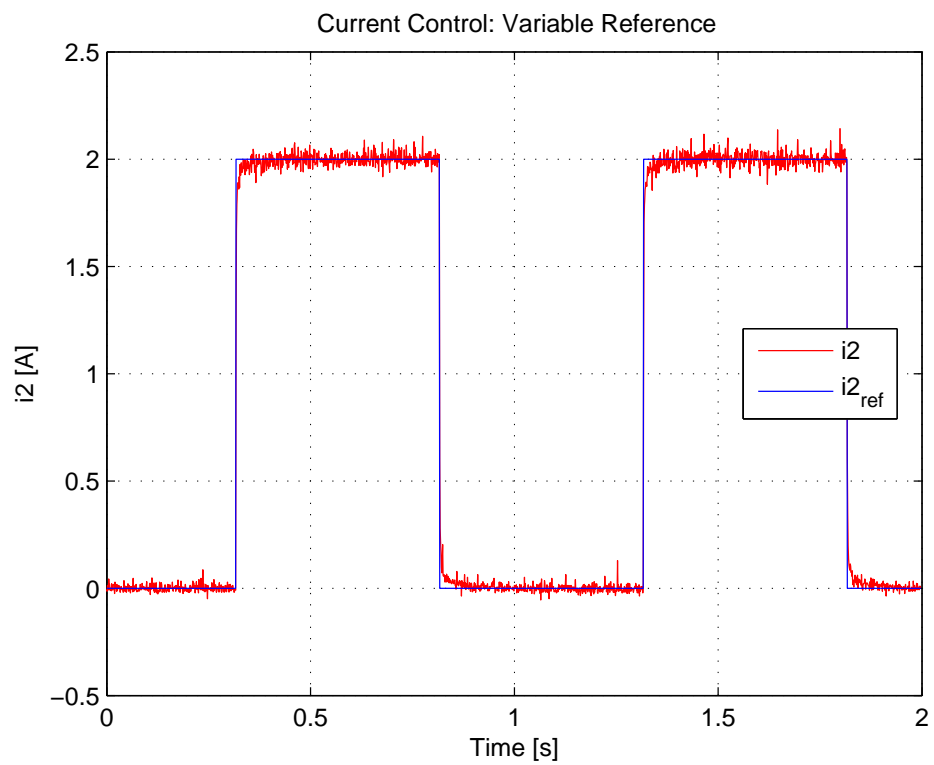
Figure 6-5: Current Control Performance: variable current reference.

Chapter 7

Conclusions and Future Work

7.1 Conclusions

The project has developed a simulation model of the flywheel prototype validated with experimental tests. This simulation model has been used to design and simulate a position control system to achieve the vertical levitation of the flywheel.

The control system presented includes a velocity estimator which provides an improved dynamic response of the position control. The control system has been tested in simulation introducing measurement noise in the feedback path. To improve robustness, discrete filters have been introduced for both position and velocity estimation.

The control system has been implemented digitally in DSP, for the use with the experimental setup. However, no experimental results for position control have been achieved up to this point due to digital implementation issues.

In addition, the hardware development for the radial magnetic bearings has been developed for future use.

7.2   Future Work

7.2.1   Velocity Observer

Due to the high impact of noise in the velocity estimation, a velocity observer would be recommended. The observer would provide an estimation filtering the noise and adjusting the parameters of the estimator online. It is an advanced control technique which is very recommended for position control, and it would be interesting to implement in future work.

7.2.2   Finite Elements Analysis

For a proper identification of the system a Finite Elements Analysis should be performed using the 3D model provided. With an accurate data of the magnet materials the software is able to simulate the magnetic response of the whole system, taking into account the real geometry of the prototype [25].

7.2.3   Control of radial magnetic bearings

Previously a PhD thesis has been dedicated to the different control strategies for the radial magnetic bearings [19][9][10]. The present project has helped to the future implementation of this work by developing hardware interfaces.

It remains for future work the development of the DSP code associated to the control of the radial bearings, and its relationship with the axial magnetic bearing control system.

7.2.4   Energy Storage Control

Once the complete levitation system is operating in static mode, the flywheel should be tested for energy storage. That means using a dedicated three-phase back-to-back power converter to control the bi-directional energy flow of the electric machine.

The levitation system must be checked for correct operation under high rotational speeds. The effect of the flywheel rotation in the levitation system has been considered

in previous studies [19], however it remains for future work the experimental validation of the whole levitation system as well as the evaluation of the disturbance rejection capability under such operating conditions [32][15].

7.2.5 Self-sensing control

In the future, a possible room for improvement of the whole system is clearly the use of self-sensing control techniques [10][11][9][8][23].

Self-sensing techniques aim basically to estimate the position by injecting high frequency signals to detect the position looking at the variation of the reluctance of the circuit. The flywheel prototype is a good candidate where these techniques could be eventually used, since the magnetic circuit has a direct and strong relation with the position, the variable aimed to control. The use of self-sensing control will allow to bring down by removing position sensors, which represent a significant part of the total cost of the prototype.

7.2.6 Integrated hardware package

In order to optimize the hardware used for the entire levitation system, it would be necessary to integrate the radial and axial power converters in a unique hardware package. The future power converter could operate at higher switching frequencies to achieve a higher performance of the levitation control due to the reduced current ripple in the bearings.

Therefore, the future designer should also consider MOSFETs as a possible device, that would allow to use a higher switching frequencies with high efficiency.

Appendix A

Digital implementation in DSP

The control system described in chapter 5 has been implemented digitally in C code in the DSP (Texas Instruments® TMS320 F28335). The real-time software must work according to simulation to provide the modulation signals for the inverter as well as integrate the feedback signals into the control algorithm.

A.1   IQmath library

The IQmath library from TEXAS INSTRUMENTS® is a collection of optimized functions to develop efficient fixed point code algorithms.

However, the fact that the DSP works in fixed-point makes the digital implementation not an easy task, since every intermediate calculations must remain within a given range and precision. The DSP makes use of the TEXAS INSTRUMENTS® *IQmath* library.

The IQ data type is set to IQ19, whose range [-4096, 4095] and precission $(1.907 \cdot 10^{-6})$ are suitable for most applications.

A.2   Structure of the real-time control software

The structure of the real-time software will be the following:

- **Main:** The main part will include configuration of PWM and ADC modules as well as initialization of control variables.

- **AD Interruption:** The ADC will be triggering an interruption every sample time, where the control algorithm is included within. The

- **Modes of operation:** In the top part of the code, several modes of operations are defined as pre-processor rutines, either for testing, open loop or closed loop. Also, several optional features can be enabled or disabled only by commenting out one line. This allows the user to easily select different modes of operation and set current references manually in real-time for instance.

A.3   Operation Modes

The software has been provided with pre-processor rutines that allow to select the mode of operation easily. The modes are structured in test modes, open loop and closed loop. To select a mode of operation just compile the corresponding rutine and the associated part of the code will be compiled. To disable a mode just comment out.

Each of the modes are described below:

A.3.1   Real or simulated operation

- **REAL:** the real operation includes the updating of the PWM signals in the corresponding GPIOs, as well as the conversion of the measurement signals conected to the ADC.

- **SIM:** the software also allows to simulate the whole system, for debuging purposes.

A.3.2   Test modes

These modes are useful to test the operation of the inverter.

- **DUTYTEST:** allows to set an specific duty to each of the inverters. The desired duty can be updated online manually from the debuging monitor by typing the duty value in the *duty1_man* and *duty2_man* variables.

- **DUTYVAR:** in this mode, the duty is alternated between two values previously set. The time for each of the states can be also set. This mode have been used to apply voltage steps to the coils in order to characterize their parameters (see 3.2.1).

A.3.3   Open loop

The open loop modes allow to check the current control on its own. The different modes allow to set different current references.

- **CURRENTLOOP_FIX:** fixes a constant reference for the current, also with manual online setting. The magnitude of the current reference is taken from variables IREF1 or IREF2. It is also possible to set sinusoidal references.

- **CURRENTLOOP_VAR:** this mode changes the current reference in steps of a defined time, similarly to DUTYVAR mode. The magnitude and offset of the current reference can be set through IREF1, OFFSET1, IREF2, OFFSET 2 variables also online.

A.3.4   PWM Modulation

The user can choose the PWM modulation technique to be used, either **BIPOLAR** or **UNIPOLAR**. Unipolar modulation is preferred for this applications since the current ripple is significantly reduced.

Bibliography

[1] H. M N K Balini, C.W. Scherer, and J. Witte. Performance enhancement for AMB systems using unstable controllers. *IEEE Transactions on Control Systems Technology*, 19(6):1479–1492, November 2011.

[2] H. Bleuler, C. Gahler, R. Herzog, R. Larsonneur, T. Mizuno, R. Siegwart, and Shao-Ju Woo. Application of digital signal processors for industrial magnetic bearings. *IEEE Transactions on Control Systems Technology*, 2(4):280–289, December 1994.

[3] Hung-Cheng Chen. Adaptive genetic algorithm based optimal PID controller design of an active magnetic bearing system. In *3rd International Conference on Innovative Computing Information and Control, 2008. ICICIC '08*, pages 603–603, June 2008.

[4] Hung-Cheng Chen. Optimal fuzzy pid controller design of an active magnetic bearing system based on adaptive genetic algorithms. In *2008 International Conference on Machine Learning and Cybernetics*, volume 4, pages 2054–2060, July 2008.

[5] Xiaofei Chen, Li Ji, and Kun Liu. A BP neural network controller for magnetic suspended flywheel system. In *2010 3rd IEEE International Conference on Computer Science and Information Technology (ICCSIT)*, volume 6, pages 448–452, July 2010.

[6] A. Chiba, T. Fukao, and O. Ichikawa. *Magnetic bearings and bearingless drives*. Newnes, 2005.

[7] Wang Ding, Zhu Changsheng, Tang Ming, and Zuo Bin. The effect of controllers on the dynamic behaviour of a rotor supported on active magnetic bearings. In *2010 International Conference on Electrical and Control Engineering (ICECE)*, pages 2336–2339, June 2010.

[8] P. Garcia, F. Briz, D. Reigosa, C. Blanco, and J.M. Guerrero. On the use of high frequency inductance vs. high frequency resistance for sensorless control of AC machines. In *2011 Symposium on Sensorless Control for Electrical Drives (SLED)*, pages 90–95, September 2011.

[9] P. Garcia, J.M. Guerrero, F. Briz, and D. Reigosa. Sensorless control of three-pole active magnetic bearings using saliency-tracking based methods. In *IEEE Energy Conversion Congress and Exposition, 2009. ECCE 2009*, pages 3984–3991, September 2009.

[10] P. Garcia, J.M. Guerrero, I El-Sayed, F. Briz, and D. Reigosa. Carrier signal injection alternatives for sensorless control of active magnetic bearings. In *2010 First Symposium on Sensorless Control for Electrical Drives (SLED)*, pages 78–85, July 2010.

[11] P. Garcia, J.M. Guerrero, I El-Sayed Mahmoud, F. Briz, and D.D. Reigosa. Impact of saturation, current command selection, and leakage flux on the performance of sensorless-controlled three-pole active magnetic bearings. *IEEE Transactions on Industry Applications*, 47(4):1732–1740, July 2011.

[12] Juan Morís Gómez. *Desarrollo del Convertidor de Potencia y Sistema de Control para un Cojinete Magnético Axial*. Universidad de Oviedo, 2012.

[13] AE. Hartavi, O. Ustun, and R.N. Tuncay. A comparative approach on PD and fuzzy control of AMB using RCP. In *Electric Machines and Drives Conference, 2003. IEMDC'03. IEEE International*, volume 3, pages 1507–1510 vol.3, June 2003.

[14] Islam El-Sayed Mahmoud, Pablo Garcia, Fernando Briz, Juan M. Guerrero, David Reigosa. *Analysis of Topologies Alternatives for Radial Magnetic Bearings*. 2012.

[15] Kyungdae Kang and A. Palazzolo. Homopolar magnetic bearing saturation effects on rotating machinery vibration. *IEEE Transactions on Magnetics*, 48(6):1984–1994, 2012.

[16] Rene Larsonneur. *Design and Control of Active Magnetic Bearings Systems for High Rotational Speeds*. Swiss Federal Institute of Technology Zurich, 1990.

[17] F.-J. Lin, S.-Y. Chen, and M.-S. Huang. Tracking control of thrust active magnetic bearing system via hermite polynomial-based recurrent neural network. *IET Electric Power Applications*, 4(9):701–714, November 2010.

[18] Florian Losch. *Identification and automated controller design for active magnetic bearings systems*. PhD tesis, Swiss Federal Institute of Technology, 2002.

[19] Islam EL-Sayed Mahmoud. *Técnicas no lineales para el control de un sistema de almacenamiento cinético*. Departamento de Ingeniería Eléctrica, Electrónica, de Computadores y Sistemas. Área de Ingeniería de Sistemas y Automática. Universidad de Oviedo, 2010.

[20] Sae Kyu Nam, Ho Shik Kang, and Oh Seop Song. Fuzzy h infin; output feedback control for rotor magnetic bearing system. In *Proceedings of the 2002 IEEE*

International Conference on Fuzzy Systems, 2002. FUZZ-IEEE'02, volume 1, pages 455–459, 2002.

[21] M. A Pichot, J.P. Kajs, B. R. Murphy, A Ouroua, B. Rech, R.J. Hayes, J.H. Beno, G.D. Buckner, and AB. Palazzolo. Active magnetic bearings for energy storage systems for combat vehicles. *IEEE Transactions on Magnetics*, 37(1):318–323, January 2001.

[22] B. Polajzer. Modeling and control of horizontal-shaft magnetic bearing system. In *Proceedings of the IEEE International Symposium on Industrial Electronics, 1999. ISIE '99*, volume 3, pages 1051–1055 vol.3, 1999.

[23] D. Raca, P. Garcia, D. Reigosa, F. Briz, and R. Lorenz. A comparative analysis of pulsating vs. rotating vector carrier signal injection-based sensorless control. In *Twenty-Third Annual IEEE Applied Power Electronics Conference and Exposition, 2008. APEC 2008*, pages 879–885, February 2008.

[24] Robert B. Schainker. Executive overview: energy storage options for a sustainable energy future. In *IEEE Power Engineering Society General Meeting, 2004*, pages 2309–2314 Vol.2, June 2004.

[25] E. Schmidt and M. Hofer. Parameter evaluation of a hybrid magnetic bearing by using 3d finite element analyses. In *Power Engineering Conference, 2008. AUPEC '08. Australasian Universities*, pages 1–6, 2008.

[26] G. Schweitzer. *Active Magnetic Bearings - Chances and Limitations*. International Centre for Magnetic Bearings, ETH Zurich.

[27] G. Schweitzer and E.H. Maslen. *Magnetic bearings: theory, design, and application to rotating machinery*. Springer Verlag, 2009.

[28] H. Seto and T. Namerikawa. An h infin; control system design of a magnetic bearing considering periodic disturbance. In *Proceedings of 2005 IEEE Conference on Control Applications, 2005. CCA 2005*, pages 227–232, August 2005.

[29] Z. A Styczynski, P. Lombardi, R. Seethapathy, M. Piekutowski, C. Ohler, B. Roberts, and S.C. Verma. Electric energy storage and its tasks in the integration of wide-scale renewable resources. In *Integration of Wide-Scale Renewable Resources Into the Power Delivery System, 2009 CIGRE/IEEE PES Joint Symposium*, pages 1–11, July 2009.

[30] G.O. Suvire, P.E. Mercado, and L. J. Ontiveros. Comparative analysis of energy storage technologies to compensate wind power short-term fluctuations. In *Transmission and Distribution Conference and Exposition: Latin America (T D-LA), 2010 IEEE/PES*, pages 522–528, November 2010.

[31] Wensen Wang, H. Hofmann, and C.E. Bakis. Ultrahigh speed permanent magnet motor/generator for aerospace flywheel energy storage applications. In *2005*

IEEE International Conference on Electric Machines and Drives, pages 1494–1500, May 2005.

[32] Xiaogang Wang and Bin Mei. Study on the centripetal effect of a magnetic bearing. In *2010 International Conference on Electrical and Control Engineering (ICECE)*, pages 2135–2138, June 2010.

[33] Zhang Weiwei. A flywheel energy storage system suspended by active magnetic bearings with fuzzy PID controller. In *2010 International Conference on Computer Application and System Modeling (ICCASM)*, volume 5, pages V5–116–V5–119, October 2010.

[34] Tao Zhang. Adaptive vibration compensation control research on rotor in active magnetic bearing system. In *2010 International Conference on Measuring Technology and Mechatronics Automation (ICMTMA)*, volume 1, pages 428–431, March 2010.

[35] Weiwei Zhang and Yefa Hu. A prototype of flywheel energy storage system suspended by active magnetic bearings with PID controller. In *Power and Energy Engineering Conference, 2009. APPEEC 2009. Asia-Pacific*, pages 1–4, March 2009.